THE UNIVERSITY of EDINBURGH

Measurements of the ^{25}Mg(d, p)^{26}Mg reaction to constrain nucleosynthesis in novae and the weak s-process

Conor Brian Hamill

Doctor of Philosophy
The University of Edinburgh
May 2021

Abstract

The $^{25}\text{Al}(p, \gamma)^{26}\text{Si}$ reaction rate is one of the few outstanding uncertainties in modelling the contribution from novae to the galactic budget of the long-lived radioactive isotope ^{26}Al. The rate is dominated by three key resonances in ^{26}Si ($J^\pi = 1^+$, 0^+ and 3^+), of which only the 3^+ resonance has been directly constrained. The first experiment described in this thesis used the $^{25}\text{Mg}(d, p)$ reaction to measure the spectroscopic factors of the three analog states in the mirror nucleus ^{26}Mg, including a spectroscopic factor for the 0^+ state. The proton partial widths estimated from these spectroscopic factors established the 0^+ state contributes $\lesssim 10\%$ of the $^{25}\text{Al}(p, \gamma)$ reaction rate, with the 3^+ state dominating at higher temperatures. The upper limit extracted for the 1^+ proton partial width, which disagreed with a previous ($^4\text{He}, ^3\text{He}$) study, found it only contributes to the reaction rate at low temperatures. Previous studies presented evidence for a negative parity state in ^{26}Mg around 5.7 MeV, consistent with the angular distribution measured in the current work, which has not had an analog state in ^{26}Si confirmed. Future work should focus on identifying such a state and further constraining the parameters of the dominant 3^+ resonance.

The amount of neutrons available for the weak s-process depends on the $^{22}\text{Ne}(\alpha, n)$ and $^{22}\text{Ne}(\alpha, \gamma)$ reaction rates, which proceed through natural-parity states of ^{26}Mg above the alpha and neutron thresholds. The second experiment in this thesis used the $^{25}\text{Mg}(d, p)$ reaction to populate states above the ^{26}Mg alpha threshold. The shapes of the angular distributions constrained the ℓ-transfers populating those states. This established the spin/parities of states at 10.82, 10.95, 11.08 and 11.11 MeV as 2^+, 1^-, 2^+ and 2^+ respectively. Combining these assignments with previous alpha-transfer studies allowed alpha partial widths to be extracted, which were used to calculate reaction rates for both reactions. Studies seeking to further reduce these rate uncertainties should focus on constraining the properties of the 10.95 and 11.11 MeV states, which dominate the reactions at temperatures whenever the $^{22}\text{Ne}(\alpha, n)$ rate overtakes that of the $^{22}\text{Ne}(\alpha, \gamma)$ reaction.

Declaration

I declare that this thesis was composed by myself, that the work contained herein is my own except where explicitly stated otherwise in the text, and that this work has not been submitted for any other degree or professional qualification except as specified.

Parts of this work have been published in [1].

(Conor Brian Hamill, May 2021)

Acknowledgements

The work presented in this thesis was done with the backing of many people, both inside and outside physics. I feel very fortunate to have participated in such a collaborative and open-minded field of research, with such a wealth of support from people outside physics in my life.

The guidance, patience and leadership of my principal supervisor, Prof. Phil Woods, have been essential throughout my PhD and have allowed me to complete this piece of work. A large amount of credit must also be given to my second supervisor, Dr. Daid Kahl, whose guidance throughout my PhD has made me a better programmer, writer, and scientist. To the Edinburgh nuclear physics group I have a lot of gratitude. From the welcome I received from day one of my PhD, to the submission of this work, the members of the group have always been a great help and always willing to answer the many questions I've had. Special thanks must be given to Oscar and Tom for guiding me through the nuances of C++ and ROOT, and Ashley and Sam, who helped me through the many intricacies of python.

Thanks must be given to my collaborators at the Triangle Universities Nuclear Laboratory (TUNL) research facility, for the kind welcome to North Carolina and the smooth running of the experiment discussed in this work. To Richard Longland, Kiana Setoodehnia, Caleb Marshall, Frederico Portillo, I am sincerely grateful. I also have a huge amount of gratitude for the technical staff at TUNL, especially John Dunham, for the smooth running of the experiment presented in this work, and for John Greene of Argonne National Laboratory, who is responsible for the high-quality targets that allowed this work to achieve the success it did.

Proficient and considerate guidance in understanding the details of reactions calculations through FRESCO was provided by Kiana Setoodehnia and Antonio Moro, who I am both grateful to. Clarification on input for TALYS calculations from Arjan Koning is also greatly appreciated.

To my amazing wife Hannah, who has supported me through every moment of my PhD, I have a massive amount of gratitude. Her patience in listening to many many hours of physics talk and belief in my ability to overcome any challenge that

Contents

List of Figures

List of Tables

Chapter 1

Introduction

1.1 Nuclear Astrophysics and the Quest for the Origin of the Elements

1.1.1 The Origins of Nuclear Astrophysics

Knowledge of the origin of the elements that we see on Earth and the source of the power of stars in our night sky has been sought by humans from ancient times. The ancient Greeks considered the Universe to consist of the four corruptible earthly elements, with the heavenly stars made of the immutable and eternal aether, while the ancient Chinese held the belief that everything that could be seen was made of five elements, the relationships of which alter the world. In more modern times, a complete explanation of the origin of the chemical elements and the mechanisms that power stars is still sought by scientists. Chemistry explains the reactions we see in everyday life, but provides no answers as to where the elements that make up the Earth and other bodies in our Universe came from.

As the nature of the atomic nucleus was uncovered by the work of Nobel laureates in the early 20th century [2–4], theories about how these nuclear reactions and properties of nuclei might have a larger scale effect in our Universe began to form. A large gap in our understanding of stellar bodies came from ignorance of what the energy source of the Sun (and by extension, other stars) was; the conversion of gravitational energy to heat (a theory that was endorsed by von Helmholtz and Lord Kelvin) was in contention with geological records of the Earth [5], while the

lifetime provided by a fossil fuel like coal would not have even reached the length of recorded human history.

The first statement that the transmutation of nuclei could be at the origin of the Sun's power came from Eddington in the 1920s [6]. Francis Aston had recently measured the mass of a helium atom to be *less* than that of 4 hydrogen atoms [7], which led Eddington to propose that the transformation of hydrogen into helium could liberate energy via the "lost" mass between the two species, although a lack of knowledge of nuclear structure at the time prevented a full understanding of the responsible mechanism. This idea was built upon by Hans Bethe and Charles L. Critchfield, who derived the proton-proton (p-p) chain in 1938, providing the detail of the mechanism that liberates energy from the conversion of hydrogen to helium [8].

Around the same time, the carbon-nitrogen-oxygen (CNO) cycle was developed independently by Carl von Weizscker [9] and Hans Bethe [8], describing another process converting hydrogen into helium and powering the Sun. At this time this process was favoured by Bethe to be the primary source of energy production in the Sun, as nitrogen was believed to comprise $\sim$10 % of the Sun's mass (modern estimates now place the abundance around 0.1 % by mass, with the p-p chain understood to be the dominant source of energy production [10]).

The prediction by Fred Hoyle of a resonance state in ^{12}C near the threshold of the ^{8}Be + ^{4}He reaction at solar temperatures indicated an increase in the yield from this reaction, bridging the gap of production between helium and carbon [11]. Thus, while light nuclei had explanations for their origins, elements heavier than carbon had no description of their production mechanism. This was a key point of understanding the origin of the elements in our Galaxy - while the Sun (and the rest of the observed Universe) is comprised nearly entirely of hydrogen and helium, it was known that it also included heavier elements (collectively referred to as metals by astronomers).

Modern estimates of the Sun's metallicity from spectroscopy are roughly Z=0.012-0.013 [10, 12], meaning approximately 1% of the Sun's mass is comprised of elements heavier than hydrogen and helium. Older stars tend to have smaller masses and metallicities (as they were formed when the Universe was made of a higher proportion of hydrogen and helium), while more massive stars have shorter lifetimes, and so tend to be younger. Thus, massive stars observed will have been formed more recently from material with a greater proportion of elements heavier than helium (in addition to their larger masses allowing them to synthesise elements beyond hydrogen and helium more easily), resulting in typically higher

2

metallicities than older or lower-mass stars.

In 1957, two seminal works for the field of nuclear astrophysics were published. The first was a paper by Margaret Burbidge, Geoffrey Burbidge, William A. Fowler, and Fred Hoyle (known as B^{2}FH from the authors' initials) [13]. As well as drawing together the ideas of previous scientists on the origin of the elements, the contributions of various nucleosynthesis processes in different stellar environments were evaluated using abundance patterns observed by astronomers. It made the argument that only the lightest elements in the Universe were created during the Big Bang and the ejection of heavier mass elements synthesised by stars into the interstellar medium, and the subsequent reformation of younger stars from this material is what leads to the anti-correlation in metallicity and age of stars. The various explosive stellar environments that could be responsible for the production and distribution of elements about our Galaxy were also considered, including supernovae, massive stars, and novae. Also included were tables describing which elements were considered to be produced by the slow neutron capture (s) and rapid neutron capture (r) processes.

The second work of significance published concurrently that year came from Alastair G. W. Cameron, in the form of "Stellar Evolution, Nuclear Astrophysics, and Nucleogenesis". This was humbly described as mere notes for a series of lectures, but stands as a comprehensive description of the life cycles of stars, the environments that nuclei can be produced in, and an explanation of elemental abundances observed in our Galaxy [14–16].

This interplay of theory, experiment and observation to explain the origin of the elements that is shown in both of these works is a philosophy that still drives development in the field of nuclear astrophysics today.

1.1.2   Recent Progress in Nuclear Astrophysics

In the past 60 years, the field of nuclear astrophysics has made improvements in experimental performance, computational power, and increasingly insightful astronomical observations. This has resulted in significant leaps in our understanding of the mechanisms that power stars and create the elements in our Universe, including which astrophysical processes are responsible for the creation of the nuclear isotopes (see Figure 1.1).

Many nuclear reactions are responsible for producing the known isotopes in our Universe, but it is a subset of these that nuclear astrophysicists consider most pertinent to reduce the nuclear reaction rate uncertainties of, so as to gain greater confidence in our interpretation of astronomical observations. However, for many of these key reactions, direct studies are not yet possible, and a lack of certainty on key nuclear reaction rates prevents us from fully understanding the processes that drive nucleosynthesis. A combination of theory and carefully chosen experimental measurements are needed for indirect studies that advance our understanding of the key reactions in the production of elements in our galaxy. This often takes the form of acquiring nuclear information through transfer reactions – populating key states in a nucleus of interest through the transfer of nucleon(s).

Transfer reactions to constrain nuclear reaction rates and their implications for stellar nucleosynthesis are what will be discussed in this thesis. By measuring the $^{25}\text{Mg}(d,p)^{26}\text{Mg}$ reaction, the work described in this thesis sought to constrain the reactions involved in two key nuclear processes. The first experiment constrained properties of states of ^{26}Mg that are mirror states to those involved in the $^{25}\text{Al}(p,\gamma)^{26}\text{Si}$ reaction at nova temperatures, reducing the uncertainty in the amount of the γ-ray emitting isotope ^{26}Al produced in nova explosions, and is discussed in Chapter 4. I was the first author of a paper published in a peer-reviewed journal (see Ref. [1]) describing the results of this first experiment. The second experiment constrained properties of states in ^{26}Mg that the $^{22}\text{Ne}(\alpha,n)$ and $^{22}\text{Ne}(\alpha,\gamma)$ reactions proceed through, and is discussed in Chapter 5. Constraining the rates of these reactions is necessary to determine the amount of neutrons available for nucleosynthesis in the weak s-process.
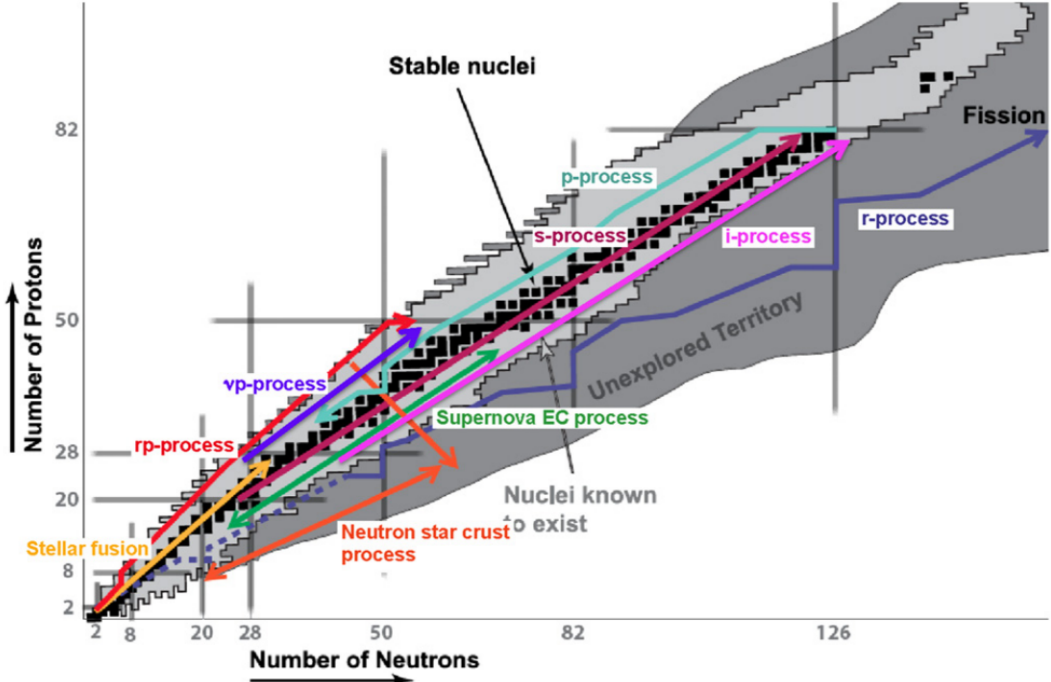
Figure 1.1 *A chart of nuclear isotopes, showing which astrophysical processes are understood to create them, from Ref. [17].*

1.2 The Synthesis of Nuclear Isotopes in Novae

1.2.1 Nucleosynthesis in Classical Novae

Stars with masses ranging from roughly 0.07-8.0 $M_\odot$ will end their lives as white dwarfs, compact stellar objects supported by electron degeneracy pressure, in which no fusion reactions take place [18]. Typical white dwarf (WD) masses are between 0.5-0.7 $M_\odot$ [19], with radii in the range of 0.8-2.0 $R_\oplus$ [20]. The surface of a typical white dwarf consists of a thin layer of hydrogen upon a layer of helium, around a core of carbon-oxygen (or possibly oxygen-neon) [21].

In close binary systems consisting of a main-sequence star and a white dwarf, material from the main-sequence star is accreted on to the surface of the white dwarf. This material forms a layer of fuel on the envelope of the white dwarf, the degeneracy of which prevents the material from expanding, despite the increasing temperature and pressure it experiences as accretion proceeds. When sufficient material from the companion star has accreted so that the material reaches the Fermi temperature ($\sim$7$\times$10^7 K), a thermonuclear runaway consisting of proton captures occurs [22]. Material is ejected from the surface of the white dwarf, with
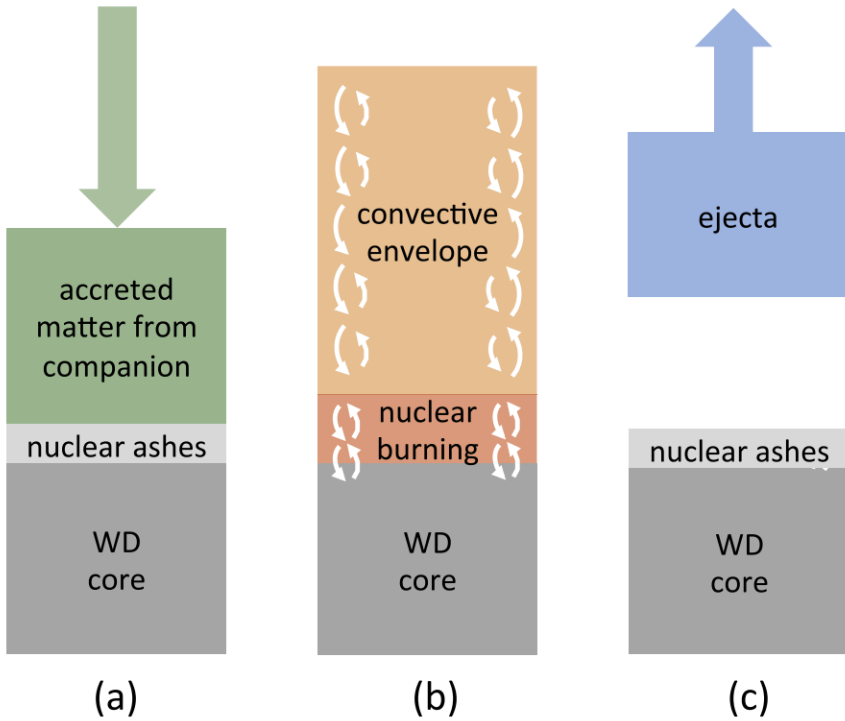
Figure 1.2 *Sketch of the processes involved in a classical nova [27].*

velocities in excess of 10^3 km/s. This ejecta is then mixed in to the interstellar medium (ISM), where it may join molecular clouds and eventually contribute to the galactic chemical abundance for subsequent generations of stars and planetary systems [23, 24]. A sketch of this process is shown in Figure 1.2. These events are observed as classical novae; sudden increases in the luminosity of a star that subsequently dims over several weeks or months, the galactic rate of which is predicted to be 50^{+31}_{-23} yr^{-1} [25], ejecting material in to the interstellar medium at a rate of $\sim 7 \times 10^{-3}$ $M_\odot$ yr^{-1} [26].

Novae are powered by explosive hydrogen burning, reaching high temperatures that peak at 0.1-0.4 GK [28]. Several isotopes with low terrestrial abundances are produced in novae, including large amounts of ^{13}C, ^{15}N, ^{17}O and, depending on the conditions of the particular nova, ^{7}Li, ^{20}Ne, ^{26}Al or ^{30}Si [29]. The production of these isotopes results in the formation of pre-solar grains with isotopic ratios distinct from solar abundances. This allows the identification of pre-solar grains with likely origins in novae, with signatures such as low ^{12}C/^{13}C, ^{14}N/^{15}N ratios and high ^{30}Si/^{28}Si, ^{22}Ne/^{20}Ne ratios compared to solar abundances [29, 30]. Observations of abundances of Ar and Ca in novae up to 10 times higher than that from solar composition have been measured. Experimental studies have sought to constrain our understanding of the amount of Ar and Ca produced in novae

6

[31] and the ratio of sulphur isotopic ratios (^{33}S/^{32}S and ^{34}S/^{32}S) [32]. A ratio of Al/Mg above the solar abundance ratio, in correlation with excesses of ^{26}Mg, is also a key indicator of a pre-solar grain of nova origin [33], as is discussed in the following subsection.

Novae can occur by accretion on to either CO (carbon-oxygen) rich or ONe (oxygen-neon) rich white dwarves. CO white dwarves are less massive than ONe white dwarves, with a mass cut of $\sim$1.1 $M_\odot$ expected [21]. As they reach the highest temperatures, ONe novae are of the greater interest for understanding nucleosynthesis. Models of these novae indicate that production of the radioactive isotopes ^{22}Na and ^{26}Al are expected to be distinct abundance signatures for these events [34].

1.2.2   Evidence of ^{26}Al in our Galaxy

In contrast to the stable isotope, ^{27}Al, that is widely found on Earth, ^{26}Al is an unstable isotope that undergoes β-decay. This isotope can be synthesised in stellar environments in its ground state (^{26}Al^g), or as a low-lying isomer (^{26}Al^m) [35]. As can be seen in Figure 1.3, the large angular momentum change of $\Delta J = 3$ associated with the second forbidden decay of the ground state to the excited state of ^{26}Mg ($5^+ \rightarrow 2^+$) gives it a long half-life of 7.2×10^5 yr [36], while the isomeric state has a super-allowed β-decay with an angular momentum change of $\Delta J = 0$ ($0^+ \rightarrow 0^+$), giving it a much shorter half-life of 6.36 s. While the ground state of ^{26}Mg that ^{26}Al^m decays to, by definition, emits no further radiation, the excited state of ^{26}Mg that ^{26}Al^g decays to rapidly γ-decays, giving off a γ ray with a distinct energy of 1.8087 MeV [37]. It is the measurement of this particular γ-ray energy by γ-ray telescopes that allows the detection of ^{26}Al in our Galaxy.

Along with the observation of the unstable element Tc in stars [39] and the observations of neutrinos from the Sun [40], the measurement of the characteristic radioactive decay line associated with ^{26}Al was one of the first pieces of direct evidence that stars are active sites of nucleosynthesis [41]. This isotope had been previously produced in laboratories, with its half-life measured to be $\sim$10^6 years, a much shorter timescale than that of the Universe [42], indicating it must be actively synthesised. Previous hints at the production of ^{26}Al in stellar environments had been found in the form of isotopic anomalies in meteorites,

Al-26 Decay Scheme
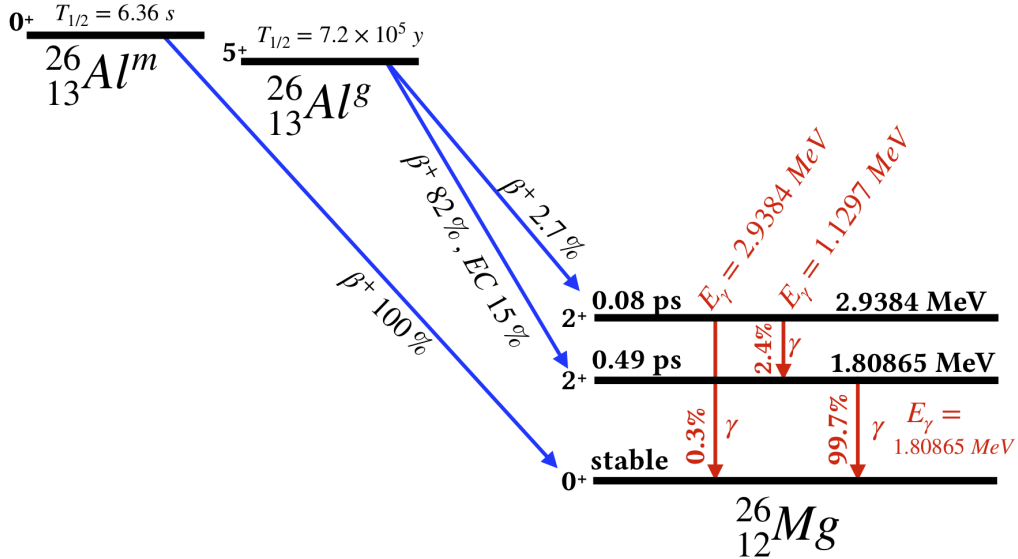
Figure 1.3 *Decay scheme of the ground and isomer states of the isotope* ^{26}Al *[38].*

with excesses of ^{26}Mg being detected in correlation with excesses of the Al/Mg ratio, which could be explained by the *in situ* decay of ^{26}Al [33].

More recent observations of the 1.8087 MeV line from the decay of ^{26}Al have provided increasingly precise estimates of the amount of the isotope currently present in our Galaxy. The COMPTEL telescope, on board the Compton Gamma-ray Observatory, has measured the distribution of the γ ray along the galactic plane, as can be seen in Figure 1.4, while the intrinsic width of the emission line has been well constrained by the RHESSI satellite [43]. The measured Doppler shift of the emission line across the Galaxy indicates it moves at a higher velocity than other objects, as shown in Figure 1.5. Measurements by the spectrometer SPI aboard the INTEGRAL satellite have measured the mass of ^{26}Al in our Galaxy to be 2.8±0.8 $M_\odot$ [44], and more recently, 2.7±0.7 $M_\odot$ [45]. These measurements have also localised the areas of our Galaxy where the flux of this distinct gamma ray is most intense, indicating which regions are producing ^{26}Al most rapidly. This has identified massive stars in their Wolf-Rayet phase and their supernovae as the main sites of production of ^{26}Al [46]. However, since the time of the first detection of the decay of ^{26}Al in our Galaxy, the explosive environments of novae have been considered possible sources for a significant
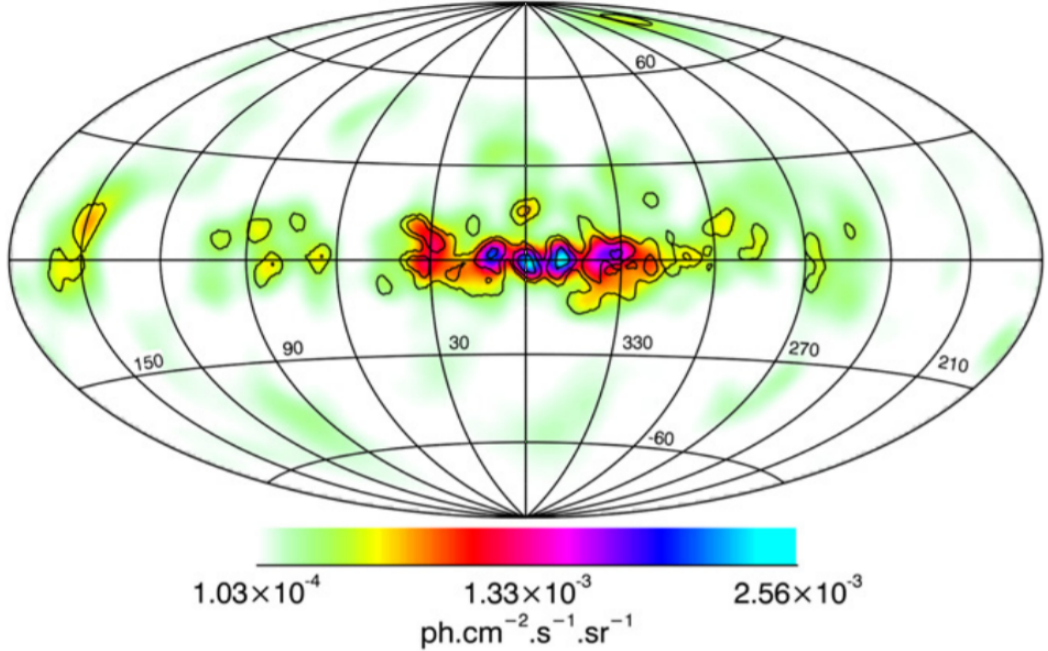
Figure 1.4 *Photon flux of the 1809 keV γ ray across the galactic plane, as observed by SPI aboard INTEGRAL [47].*

fraction of the ^{26}Al in our Galaxy [41].

Other sources of Galactic ^{26}Al

The early solar system (ESS) contained a large abundance of ^{26}Al, and its apparent homogeneous distribution in this epoch allows it to be used as a reliable chronometer for pre-solar grains measured [49]. However, a simulation of several radioactive isotopes in our Galaxy by Côté *et al.* [50] has shown that the amount of ^{26}Al in the early solar system cannot be explained by our current understanding of galactic chemical evolution, in the same way that ^{55}Mn and ^{60}Fe can.

Massive stars (of initial mass greater than 10 $M_\odot$) are well known producers of significant amounts of ^{26}Al [49]. Simulations of stars with mass 25 $M_\odot$ and solar metallicities indicate that convective shell carbon burning results in the production and eventual ejection of a non-negligible amount of ^{26}Al [51], indicating massive stars as a significant source of ^{26}Al in this phase. In the CCSN (core-collapse supernova) phase, further ^{26}Al is produced in the ONe shells during the explosion [52]. Wolf-Rayet stars are pre-CCSN stars which have had their hydrogen layers removed by strong winds. ^{26}Al is produced via a series of proton
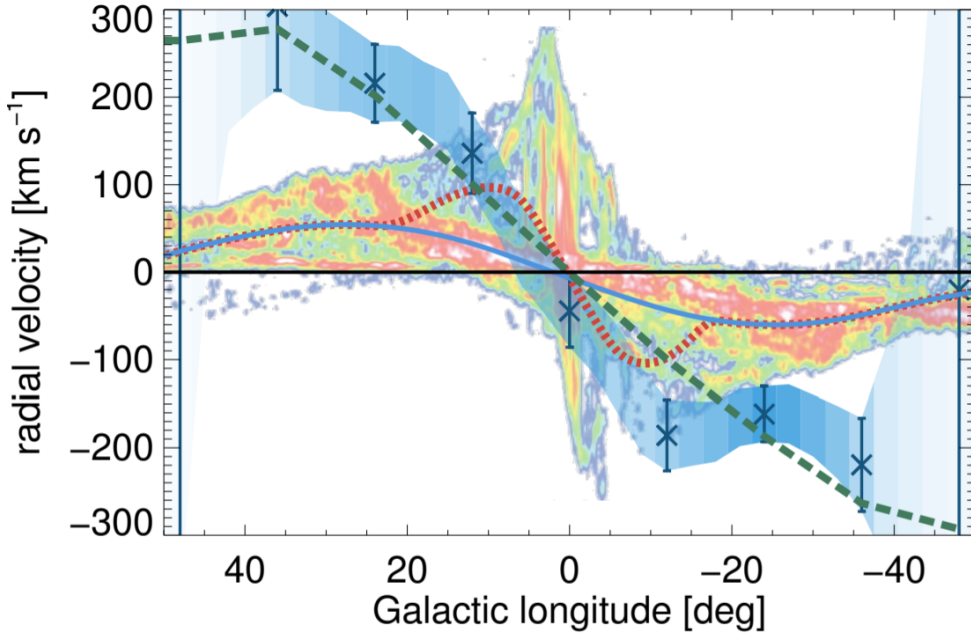
Figure 1.5 *Longitude-velocity diagram comparing the radial velocity from ^{26}Al observations (dark blue crosses and light blue shaded area) against other objects in our Galaxy, based on observed Doppler shifts [48]. Dashed green and red and solid blue lines represent expected distributions from different kinematic models. The velocities of CO-traced molecular gas are shown in the colour overlay.*

captures in the hydrogen burning phases of these stars, before being ejected in to the interstellar medium during the Wolf-Rayet phase [53].

During the later stages of the lives of stars of mass 0.6–10 $M_\odot$, the AGB (asymptotic giant branch) phase is entered, with core material being dredged up towards the surface of the star via convection and other mechanisms. For AGB stars of initial mass greater than 5 $M_\odot$, hydrogen burning at the base of the convective envelope leads to proton captures in the Mg-Al region, leading to the production of ^{26}Al [54], providing some of the galactic abundance of ^{26}Al [49].

Another γ-ray emitting long-lived radioactive isotope, ^{60}Fe ($\tau_{1/2}$=2.62×10^6 yr), is produced by massive stars in their CCSN and Wolf-Rayet phases, in addition to ^{26}Al. Therefore, the observed astronomical ^{60}Fe/^{26}Al flux ratio provides a calibration point for massive star models [55]. This means, to reliably validate stellar evolution theory against γ-ray observations of these radioactive isotopes, the synthesis of both of these radioactive isotopes in several stellar environments must be understood. This includes understanding the amount of ^{26}Al produced in nova explosions [56], which is only dependent on a small number of reactions, including the ^{25}Al$(p, \gamma)^{26}$Si reaction [57].

10

1.2.3   The Nucleosynthesis of ^{26}Al in Novae

The possibility of novae being a source of ^{26}Al began to be investigated soon after the detection of isotopic anomalies in meteorites [58–60].

In nova explosions, a series of proton capture reactions and β-decays lead to the production of ^{26}Al. The reaction network is predicted to end with the following reactions:

$$^{24}\text{Mg}(p,\,\gamma)^{25}\text{Al}(\beta^+\,\nu)^{25}\text{Mg}(p,\,\gamma)^{26}\text{Al}. \tag{1.1}$$
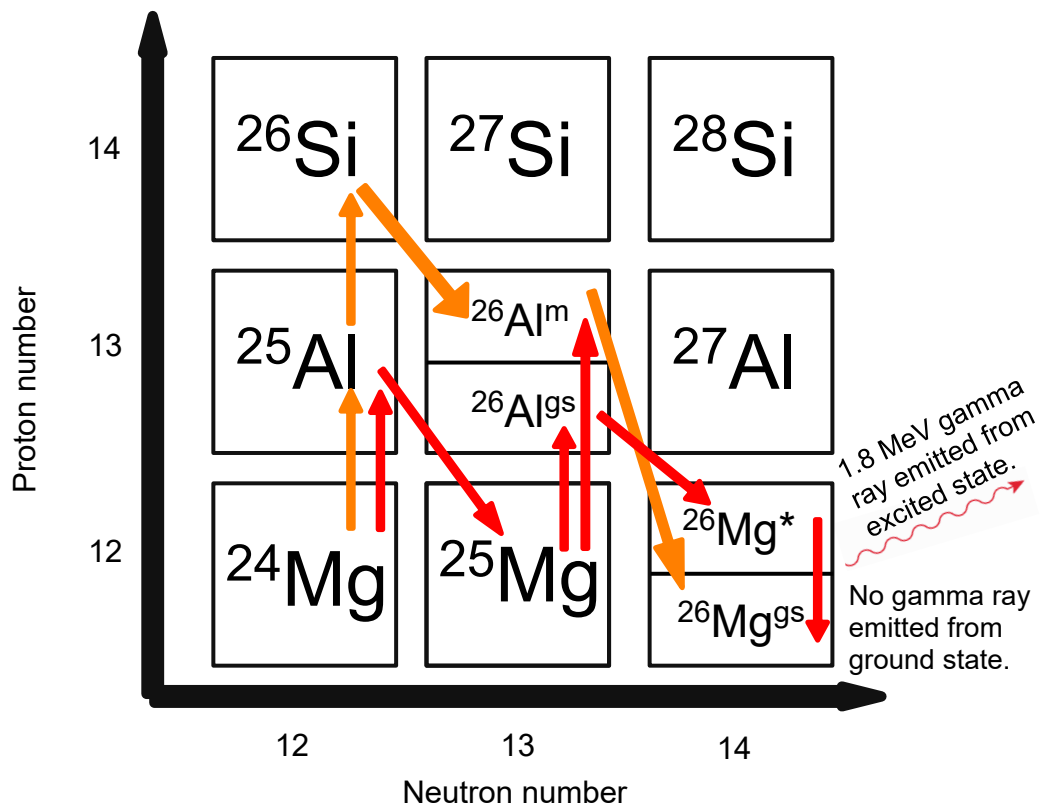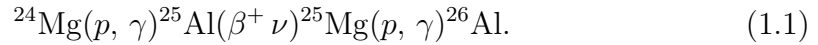
Figure 1.6   *Reaction network around A∼26 in novae. The production pathway that produces the cosmic γ-ray emitter $^{26}Al^g$ is shown in red. The $^{25}Al(p,\gamma)^{26}Si$ reaction instead leads to the production of the short-lived isomer $^{26}Al^m$, shown in the orange reaction network.*

However, at higher temperatures reached in novae, the ^{25}Al$(p,\gamma)^{26}$Si reaction is activated, and at temperatures above 0.1 GK has the possibility of competing

effectively with the β-decay of ^{25}Al ($\tau_{1/2} = 7.2$ s) [61]. This reaction produces ^{26}Si, which preferentially decays to the short lived 0^+ isomeric state of ^{26}Al, instead of the long-lived 5^+ ground state that is responsible for the characteristic γ-ray emission, as can be seen in Figure 1.6.

The 92 keV resonance that dominates the ^{25}Mg$(p,\gamma)^{26}$Al reaction at nova temperatures has had its strength directly measured at the Laboratory for Underground Nuclear Astrophysics (LUNA) [62]. More recently, the fractional decay of this resonance to the ground state of ^{26}Al has been accurately measured [35], meaning the reaction that produces ^{26}Al^g in novae is now well experimentally constrained. Therefore, the rate of the ^{25}Al$(p,\gamma)^{26}$Si reaction is one of the few reaction rate uncertainties that has the potential to strongly affect the amount of ^{26}Al produced in nova models [57].

1.2.4   Constraining the ^{25}Al(p, γ)^{26}Si reaction rate at nova temperatures

At the temperatures involved in novae, the rate of the ^{25}Al$(p,\gamma)^{26}$Si reaction depends on resonances in ^{26}Si just above the proton threshold S_p=5.51401(11) MeV [63]. However, only one of the resonances in ^{26}Si has had its resonance parameters directly constrained by experiment. This has meant that quantifying strengths for the other resonances has relied on shell-model calculations for estimates of the resonance parameters. In addition, some spin/parity ambiguities remain in the states of ^{26}Si. As mentioned previously, this is one of a small number of the most significant reactions for the rate of production of ^{26}Al in novae, and to reliably constrain this reaction rate, more information on the resonance parameters of this reaction is required. The experiment performed to constrain the rate of this reaction is described in Chapter 4.

1.3 Neutron production reactions for the s-process

1.3.1 Neutron Capture Nucleosynthesis

The modern understanding of stellar nucleosynthesis indicates that the production of the vast majority of elements heavier than iron is comprised of two neutron-capture processes: the slow neutron capture process (s-process) and the rapid neutron capture process (r-process) [64, 65].

Peaks in the abundances of certain heavy elements were seen in the spectra of elements published by Hans Suess and Harold Urey in 1956 [66]. Peaks were seen for the elements strontium, barium, and lead (A = 90, 138, 208), which correspond to the closed neutron shells of N = 50, 82 and 126 that the shell model predicts to provide structural stability to the corresponding elements. Wider peaks were also seen at mass numbers of A = 82, A = 130 and A = 196, roughly 8 atomic mass units less than the nuclei of closed shells.

These abundance patterns are explained by the synthesis of elements through two neutron capture processes. The peaks at magic numbers can be explained by the s-process, that involves a series of neutron captures on much longer timescales than the subsequent β-decays, leading to a reaction pathway that closely follows the valley of stability in the nuclear chart. This reaction pathway slows down at magic numbers, where neutron cross sections producing higher mass nuclei are smaller, leading to larger abundances around A = 90, 138, 208. The contrasting r-process involves neutron captures on a shorter timescale than the β-decays of unstable nuclei, meaning the reaction pathway to higher masses approaches the neutron dripline. Whenever this pathway encounters closed neutron shells (at so called waiting points), the mass fractions of nuclei accumulate, ultimately decaying back towards stability with a larger abundance whenever the local neutron source is exhausted. This results in the production of isotopes with neutron numbers slightly below that of closed shells, with wider abundance peaks than the s-process peaks. The solar system abundances of heavy elements, with the s and r-process peaks labelled, can be seen in Figure 1.7, with the decay back to stability across the nuclear chart shown in Figure 1.8.
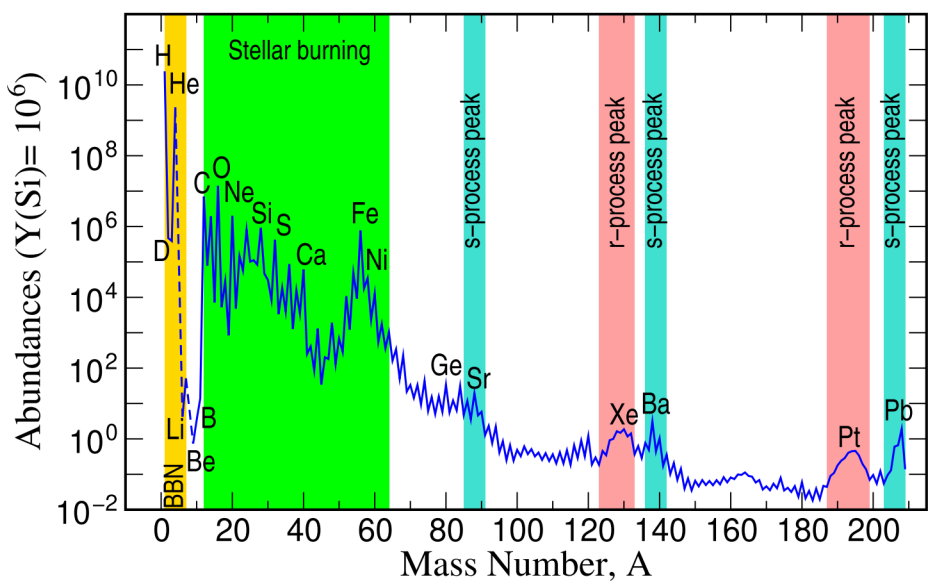
Figure 1.7 *Solar system abundances of the elements as a function of mass number, with nucleosynthesis processes indicated [65].*
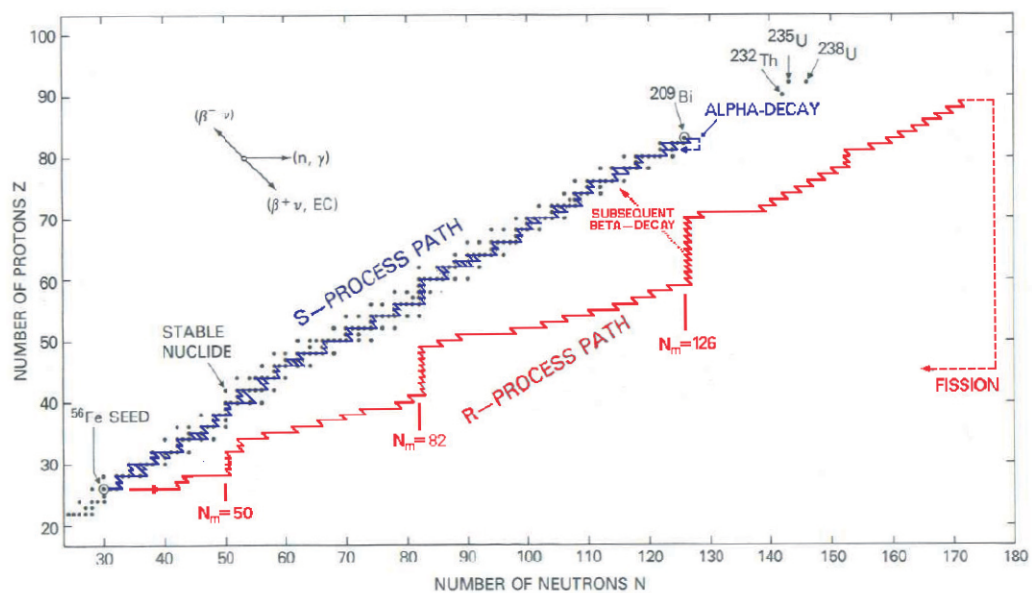
Figure 1.8 *Pathways for the s and r-process across the nuclear chart, with closed-shell numbers noted [64].*

14

The B^{2}FH paper (described in §1.1) provided a table assigning the origin of the heavy elements to either the s or r-process [13], with Clayton *et al.* (1961) [67] providing the first quantitative calculations of the s-process and Seeger *et al.* (1964) [68] providing the first quantitative calculations of the r-process.

Modern developments have increased understanding of these two processes, in terms of their astrophysical sites and the underlying nuclear physics, with each process understood to provide about half of the elements heavier than iron (with a smaller amount produced by other processes, for example, the so-called p-process).

The main historical issue with the r-process has been finding a site for its nucleosynthesis, with neutron-star mergers and core-collapse supernovae being considered as environments neutron-rich enough to provide the neutron flux required for this process. The simultaneous gravitational wave and electromagnetic radiation detection of the binary neutron-star merger event designated GW170817 provided spectra that showed the production of r-process elements, confirming it as a site of the r-process [69].

Several sites are known to be locations of the s-process, which is now understood to have several components operating in different environments with neutron density $N_n \geq 10^{11}$ cm^3, as is discussed in the following subsection.

A key nuclear astrophysics issue for determining the amount of s-process nucleosynthesis is the amount of free neutrons available for neutron-capture reactions that drive these processes. The number of neutrons available for each component of the s-process is dependent on the rate of the reactions that produce free neutrons in those environments. This means that to understand the amount of neutron capture nucleosynthesis that can take place in each environment, the rates of these neutron producing reactions must be quantified. These neutron production reactions and the different components of the s-process that they drive are discussed in the following subsection.

1.3.2   Components of the s-process

The main s-process

The main s-process (sometimes simply referred to as the s-process), is responsible for the production of s-process elements $A \geqslant 90$ and occurs mainly in AGB stars. These stars contain a thin helium intershell between the degenerate C-O core and
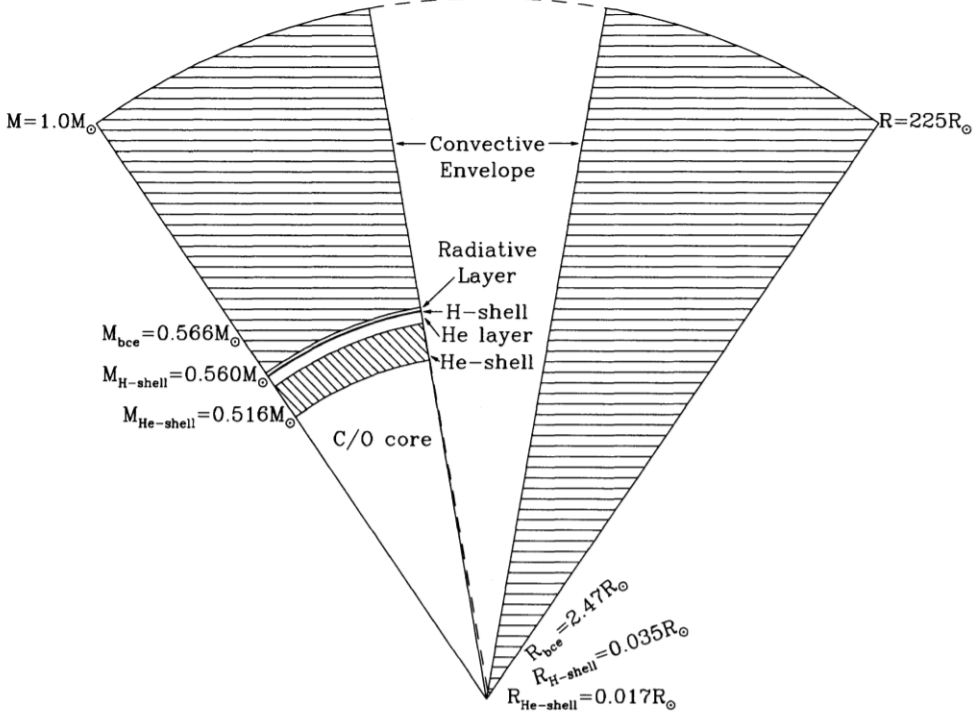
Figure 1.9 *Cross section of a 1 $M_\odot$ AGB star. Regions of the star are plotted as a mass function on the left, and as a function of radius on the right. The base of the convective envelope is labelled M_{bce}, while the masses at the middle of the hydrogen and helium burning shells are labelled $M_{H-shell}$ and $M_{He-shell}$ respectively [70].*

convective hydrogen-rich envelope, as can be seen in Figure 1.9.

These environments undergo recurrent thermal pulses, at the start of which a ^{13}C pocket forms [72]. When this region reaches roughly 90-100 MK, the ^{13}C$(\alpha, n)^{16}$O reaction is activated, which is the main source of neutrons for relatively low-mass AGB stars [73]. For more massive AGB stars, the maximum temperature in the helium flash can exceed 300 MK, which activates the ^{22}Ne$(\alpha, n)^{25}$Mg reaction, which then becomes the dominant neutron source. This can be seen in Figure 1.10.

The strong s-process

The strong s-process, first introduced by Clayton and Rassbach [74], is responsible for the production of roughly half of the lead found in our Galaxy. Stellar models have shown this occurs through neutron-capture reactions in low mass, low metallicity AGB stars [75]. The neutrons required by this process are provided by

16
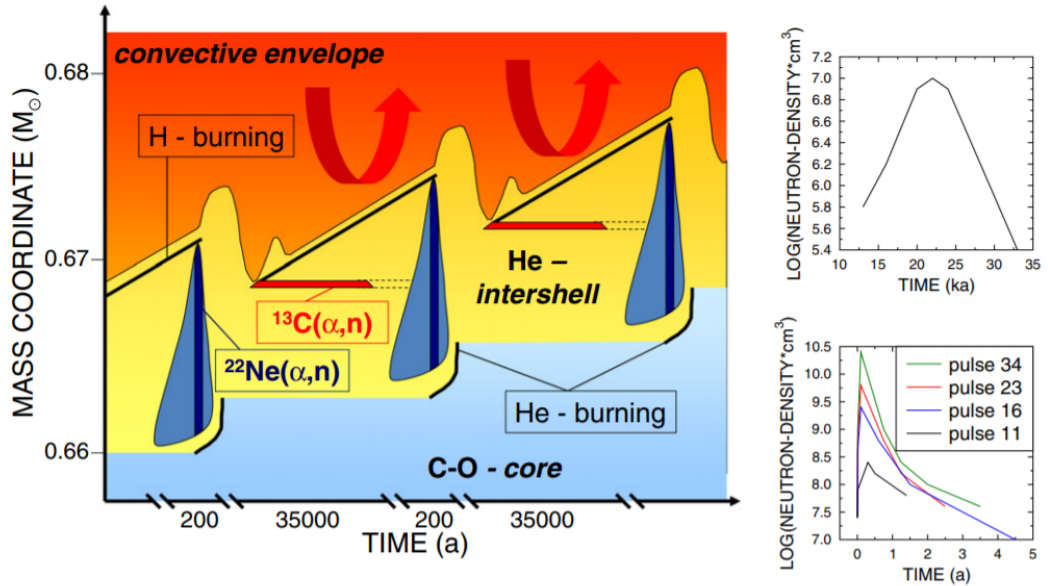
Figure 1.10 *Radial and temporal structure of an AGB star, with locations of neutron production sites for the s-process indicated (left). Neutron density as a function of time from the $^{13}C(\alpha, n)^{16}O$ (top right) and $^{22}Ne(\alpha, n)^{25}Mg$ (bottom right) reactions for a low mass AGB star. The higher efficiency of the $^{22}Ne(\alpha, n)^{25}Mg$ neutron production at later pulses is due to the increase in bottom burning temperature [71].*

the $^{13}C(\alpha, n)$ reaction, with the majority of the neutron-capture nucleosynthesis in these environments taking place inside the ^{13}C pocket [76].

The weak s-process

The weak s-process produces elements between Fe and Sr (i.e. of mass number $60 \lesssim A \lesssim 90$) [77]. This process occurs in massive stars ($M > 8\ M_\odot$), a simplified structure of which can be seen in Figure 1.11, and is predominantly driven by free neutrons produced by the $^{22}Ne(\alpha, n)^{25}Mg$ reaction [78].

During the H-burning phases of the star's evolution, the CNO cycle uses carbon, nitrogen and oxygen isotopes as catalysts to convert hydrogen nuclei to helium nuclei. The slowest reaction in this cycle is the $^{14}N(p, \gamma)$ reaction, resulting in a build up of ^{14}N when hydrogen is locally exhausted [80]. ^{14}N then undergoes the

17
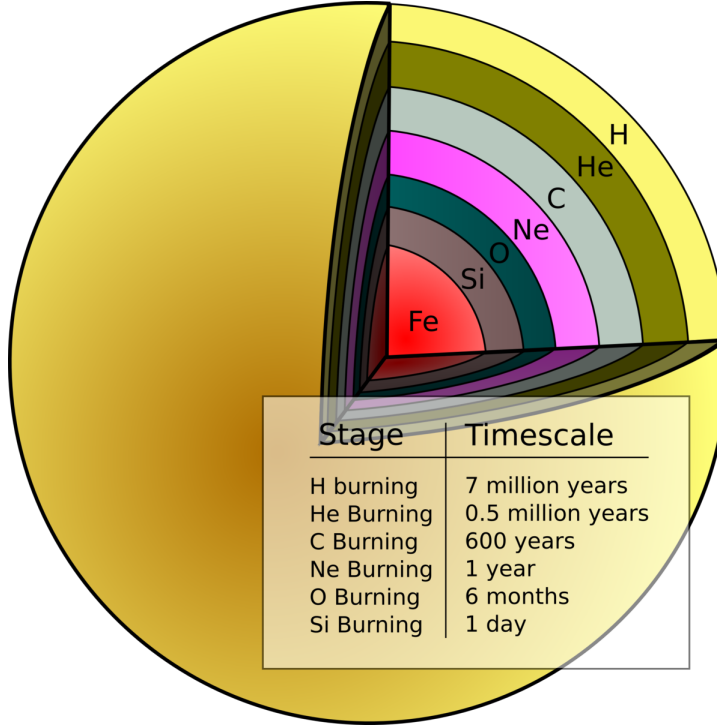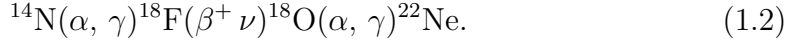
Figure 1.11 *Schematic of the inside of a pre-supernova massive star, with the timescales for different stages of burning for a star of 25 $M_\odot$ given [79].*

following reaction sequence during He-burning to produce ^{22}Ne [78]:

$$^{14}\text{N}(\alpha, \gamma)^{18}\text{F}(\beta^+ \nu)^{18}\text{O}(\alpha, \gamma)^{22}\text{Ne}. \tag{1.2}$$

Due to the large cross section of the $^{14}\text{N}(n, p)^{14}\text{C}$ reaction, ^{14}N removes neutrons from the budget for the s-process. The reaction pathway in equation 1.2 removes this neutron poison from the local environment, increasing the amount of s-process nucleosynthesis possible. Once the temperature in the helium core passes roughly 0.25 GK, the $^{22}\text{Ne}(\alpha, n)^{25}\text{Mg}$ (Q value=-478.34(5) keV [81]) reaction is activated, producing neutrons for the weak s-process [78]. However, the $^{22}\text{Ne}(\alpha, \gamma)^{26}\text{Mg}$ reaction (Q value=10614.74(3) keV [81]) can be activated at lower temperatures than the $^{22}\text{Ne}(\alpha, n)^{25}\text{Mg}$ reaction, removing α-particles that would have otherwise been available to produce free neutrons. At the end of the He-burning phase, not all the ^{22}Ne in the star is used up, allowing the $^{22}\text{Ne}(\alpha, n)^{25}\text{Mg}$ and $^{22}\text{Ne}(\alpha, \gamma)^{26}\text{Mg}$ reactions to be re-activated using α-particles produced in the $^{12}\text{C}(^{12}\text{C}, \alpha)^{20}\text{Ne}$ reaction during C-burning. This provides a second burst of neutrons for the weak s-process, which can provide a neutron exposure comparable to that generated in the He-burning core previously [82]. Neutron contributions from the $^{12}\text{C}(^{12}\text{C}, n)^{23}\text{Mg}$ reaction have also been shown

18

to be responsible for the production of a small amount of s-process elements, but ^{22}Ne$(\alpha, n)^{25}$Mg remains the main source of neutrons for the production of elements in this mass range [83]. Therefore, for a full understanding of neutron production in the weak s-process, the reaction rates of both the ^{22}Ne$(\alpha, n)^{25}$Mg and ^{22}Ne$(\alpha, \gamma)^{26}$Mg reactions across the appropriate temperature ranges must be reliably quantified.

1.3.3 Constraining the ^{22}Ne(α, γ)^{26}Mg and ^{22}Ne(α, n)^{25}Mg reactions for the weak s-process

Understanding the neutron budget available in massive stars will reduce uncertainty on all the (n, γ) reactions that take place in the weak s-process, including the ^{59}Fe(n, γ) reaction, which produces the γ-ray emitting long-lived isotope ^{60}Fe in massive stars [55]. As mentioned previously in §1.2.3, the ^{60}Fe/^{26}Al flux ratio is used as an indicator for the accuracy of models of massive stars, meaning understanding the nucleosynthesis of these radioactive isotopes allows benchmarking of stellar models with greater certainty [56].

Both the ^{22}Ne$(\alpha, n)^{25}$Mg and ^{22}Ne$(\alpha, \gamma)^{26}$Mg reactions proceed through natural parity resonance states in ^{26}Mg. The ^{22}Ne$(\alpha, \gamma)^{26}$Mg reaction proceeds through excited states above the alpha threshold (S_α=10614.8(1) keV [84]), while the endothermic ^{22}Ne$(\alpha, n)^{25}$Mg reaction involves states above the neutron threshold (S_n=11093.09(4) keV [84]).

While the ^{22}Ne$(\alpha, \gamma)^{26}$Mg reaction can operate at lower temperatures in stars (0.1–0.2 GK), the ^{22}Ne$(\alpha, n)^{25}$Mg reaction is not activated until the end of helium burning in massive stars (temperatures in the range 0.2–0.3 GK). Many properties of the important resonance states in ^{26}Mg remain uncertain. These states of interest have been investigated in several reaction studies, including direct and indirect reactions that allow the extraction of the properties of states that these resonances proceed through, including the excitation energies, partial widths and spin/parities of these states.

The second experiment that comprises this thesis, described in Chapter 5, seeks to constrain the rates of the ^{22}Ne$(\alpha, n)^{25}$Mg and ^{22}Ne$(\alpha, \gamma)^{26}$Mg reactions by investigating properties of states of ^{26}Mg above the alpha threshold through the ^{25}Mg(d, p) reaction and so constrain the number of neutrons available for the weak s-process.

Chapter 2

Theory

2.1 Overview

As previously mentioned, this thesis describes two experiments using the ^{25}Mg$(d,p)^{26}$Mg reaction to constrain the ^{25}Al$(p,\gamma)^{26}$Si reaction at nova temperatures and the ^{22}Ne$(\alpha,\gamma)^{26}$Mg and ^{22}Ne$(\alpha,n)^{25}$Mg reactions in massive stars for the weak s-process. These astrophysically significant reactions involve two charged nuclei fusing together, after tunnelling through the potential barrier between the two nuclei. The rates of these reactions of astrophysical interest are dominated by resonances associated with states in their compound nuclei, ^{26}Si, and its mirror nucleus, ^{26}Mg.

At nova temperatures, the ^{25}Al$(p,\gamma)^{26}$Si reaction is known to proceed through a small number of resonance states above the proton threshold. At the temperatures in environments the weak s-process proceeds through, the ^{22}Ne$(\alpha,\gamma)^{26}$Mg and ^{22}Ne$(\alpha,n)^{25}$Mg reactions proceed through natural-parity (0^+, 1^-, 2^+, 3^-...) resonance states above the alpha and neutron thresholds in ^{26}Mg respectively. Despite the high level density at these excitation energies in ^{26}Mg, it is only a small number of these resonances that dominate the ^{22}Ne$(\alpha,\gamma)^{26}$Mg and ^{22}Ne$(\alpha,n)^{25}$Mg reaction rates. Extracting parameters of the resonances of these reactions directly is very challenging, for a variety of reasons. To measure the resonance parameters of the ^{25}Al(p,γ) reaction, a beam of the radioactive isotope ^{25}Al is needed, which cannot currently be produced at sufficiently high intensities. For the ^{22}Ne $+ \alpha$ reactions, measurements of the relevant resonances require very low beam energies, where the reaction yield becomes increasingly inhibited by the

Coulomb barrier. This means that to quantify the reaction rates, the properties of the resonance states must be constrained through indirect methods.

Transfer reactions are a useful tool to probe the resonant states of interest, allowing measurements of their excitation energies and the differential cross section angular distributions of the transfer reactions populating those states. The shapes of these angular distributions indicate the possible orbital angular momentum (ℓ) transfers that can populate the states, constraining the spin/parities of the states. The magnitude of the angular distribution for a state determines its spectroscopic factor, i.e., to what degree the state resembles a pure single-particle state. Transfer reactions as a tool to extract properties of resonant states are discussed in greater detail in this chapter.

States in ^{26}Si that the ^{25}Al(p,γ) reaction proceeds through have been experimentally identified, but only one of these states has had its resonance properties experimentally measured, and some spin/parities ambiguities remain. By measuring the neutron spectroscopic factors of states in ^{26}Mg, the proton partial widths and thus, the resonance strengths of the mirror states in ^{26}Si, will be estimated.

The spin/parities of nuclear states above the ^{26}Mg alpha threshold will be constrained by determining the ℓ-transfers that populate them in the ^{25}Mg(d,p) reaction, which have distinct angular distribution shapes. This will allow the alpha partial widths of states previously identified in alpha transfer reactions to be constrained, reducing the uncertainty in their contribution to the ^{22}Ne$(\alpha,\gamma)^{26}$Mg and ^{22}Ne$(\alpha,n)^{25}$Mg reactions.

How transfer reactions, combined with nuclear theory, can constrain the resonance properties of nuclear states is discussed in more detail in this chapter. Understanding these properties allows reaction rates in stellar environments to be calculated, improving understanding of the reactions that drive stellar nucleosynthesis.

2.2 Charged particle resonant reactions in stellar environments

In a stellar medium of temperature, T, the velocity distribution of the particles can be described by the Maxwell-Boltzmann distribution, $\phi(v)$:

$$\phi(v) = \left(\frac{m}{2\pi kT}\right)^{3/2} 4\pi v^2 \exp\left(-\frac{mv^2}{2kT}\right),$$ (2.1)

where

$m \equiv$ mass of particle

$k \equiv$ Boltzmann constant

$T \equiv$ temperature of stellar medium.

The stellar environments of interest in this thesis have temperatures in the range $\sim$0.1–0.4 GK. This corresponds to average kinetic energies in the range $\sim$9–35 keV. The ions that take part in nuclear reactions in stellar plasmas will have rest masses of the order of several GeV (with the proton having a rest mass of 938 MeV). As the kinetic energies of these particles are much less than their rest masses, the non-relativistic equation for kinetic energy of a particle of mass m and velocity v, $E = \frac{1}{2}mv^2$, can be substituted into the Maxwell Boltzmann distribution to be written in terms of kinetic energy:

$$\phi(v) = \left(\frac{1}{2\pi kT}\right)^{3/2} 4\pi m^{3/2} v^2 \exp\left(-\frac{mv^2}{2kT}\right),$$ (2.2)

$$\phi(E) = \left(\frac{1}{2\pi kT}\right)^{3/2} 8\pi m^{1/2} E \exp\left(-\frac{E}{kT}\right) \propto E \exp\left(-\frac{E}{kT}\right).$$ (2.3)

At stellar temperatures, nuclei have kinetic energies lower than the Coulomb potential barrier that originates in the electrostatic repulsion between the two positively charged nuclei. Therefore, for a charged particle reaction to proceed, a charged nucleus must tunnel through the Coulomb potential barrier, V_C:

$$V_C = \frac{Z_1 Z_2 e^2}{4\pi\epsilon_0 r},$$ (2.4)

where

$Z_1 \equiv$ atomic number of first reactant

$Z_2 \equiv$ atomic number of second reactant

$e \equiv$ elementary charge

$\epsilon_0 \equiv$ permittivity of free space

$r \equiv$ separation of two reactants.

Considering a particle of mass m and energy E approaching a Coulomb barrier, the probability of transmission, $T(E)$, (assuming no centrifugal barrier) can be approximated by [85]:

$$T(E) \approx \exp\left(-2\pi\sqrt{\frac{m}{2E\hbar^2}} Z_1 Z_2 e^2\right). \tag{2.5}$$

The probability of penetration through the Coulomb barrier occurring for a particle in a stellar environment of energy E, $P(E)$, is given by the product of the energy distribution of particles, $\phi(E)$, (equation 2.3) and the quantum tunneling probability, $T(E)$, (equation 2.5). The region of maximum penetration probability is known as the Gamow peak. The Gamow peak indicates to nuclear astrophysicists which centre-of-mass energies barrier penetration is most likely at for two charged particles at a certain stellar temperature, and therefore, which resonance states may contribute to nuclear reactions between those two charged particles at that temperature.

Estimates of the centre-of-mass energies at which the Gamow peak is at its highest, E_0, and the full width half maximum (FWHM) of that peak, ΔE, can be calculated empirically using the following equations [85]:

$$E_0 = 0.122\left(Z_1^2 Z_2^2 \frac{M_1 M_2}{M_1 + M_2} T_9^2\right)^{1/3} \text{MeV}, \tag{2.6}$$

$$\Delta E = 0.237\left(Z_1^2 Z_2^2 \frac{M_1 M_2}{M_1 + M_2} T_9^5\right)^{1/6} \text{MeV}, \tag{2.7}$$

where Z_1, Z_2, M_1 and M_2 refer to the atomic numbers and masses of the two nuclei respectively, and T_9 is the temperature in units of GK.

For the ^{25}Al$(p,\gamma)^{26}$Si reaction at a temperature of 0.3 GK (reached during nova explosions), the centre-of-mass Gamow window ($E_0 \pm \Delta E/2$) covers 0.20–0.40 MeV, corresponding to an excitation energy range of E_x=5.71–5.91 MeV in ^{26}Si. This is shown in Figure 2.1, with the resonance states in ^{26}Si thought to contribute to the reaction rate at this temperature labelled.

24
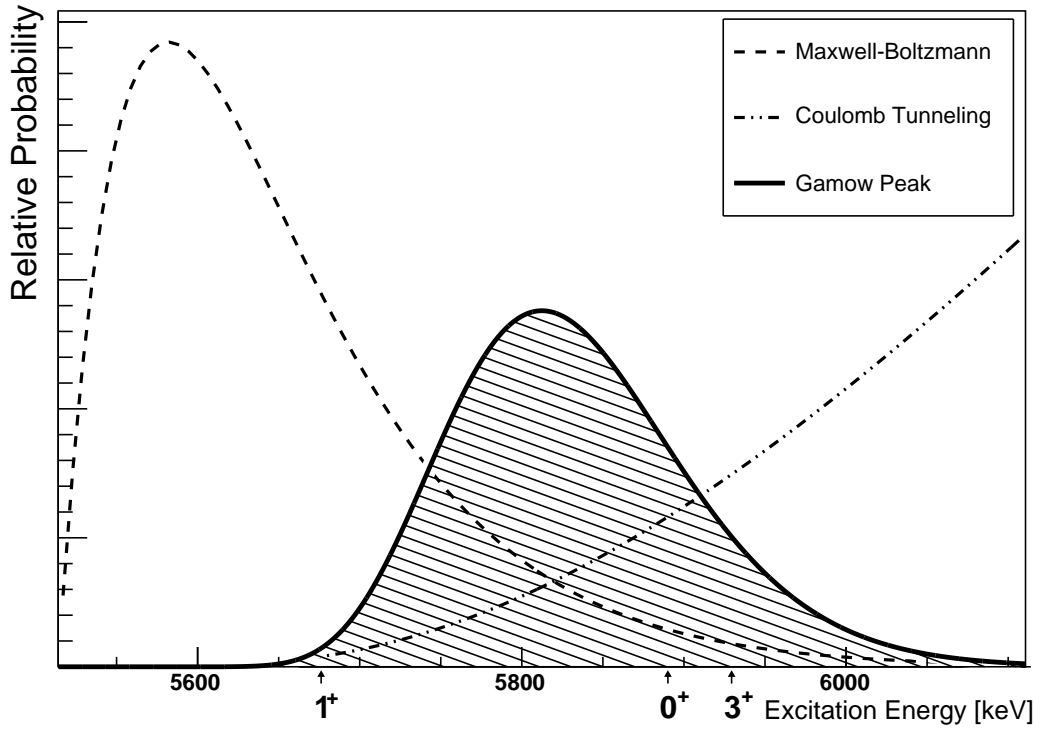
Figure 2.1   *The Gamow peak of the $^{25}Al(p,\gamma)^{26}Si$ reaction at a stellar temperature of 0.3 GK, calculated as a product of the Maxwell-Boltzmann distribution (equation 2.3) and the tunnelling probability (equation 2.5). The peak is given as a function of the excitation energy of the compound nucleus, with the labelled states within the Gamow window showing the resonances that can contribute to this reaction at this temperature.*

Many nuclear reaction rates are dominated by nuclear resonances in the Gamow peak – energies at which the cross section of the reaction will increase sharply, associated with certain discrete excited states of the compound nucleus formed by the reaction.

The Breit-Wigner formula describes the contribution of a narrow and well-isolated resonance, E_r, to the cross section of a reaction, for a particle a entering the nucleus, and a particle b leaving the compound nucleus, at a centre-of-mass energy E_{CM}:

$$\sigma = \frac{\pi \lambda_a^2 \omega \Gamma_a \Gamma_b}{(E_r - E_{CM})^2 + \Gamma^2/4},\qquad(2.8)$$

25

where

$\sigma \equiv$ resonant cross section of reaction (a,b)

$\lambda \equiv$ reduced de Broglie wavelength of incoming particle

$\Gamma_a \equiv$ partial width of entrance channel for the compound nucleus

$\Gamma_b \equiv$ partial width of exit channel for the compound nucleus

$\Gamma \equiv$ total width of resonance state in compound nucleus

$\omega \equiv$ statistical factor.

The statistical factor, ω, is given by:

$$\omega = \frac{(2J_f + 1)}{(2J_p + 1)(2J_i + 1)}, \tag{2.9}$$

where

$J_f \equiv$ spin of state populated in compound nucleus

$J_p \equiv$ spin of projectile nucleus

$J_i \equiv$ spin of initial state in target nucleus.

The reaction rate per particle pair at a certain stellar temperature, T, is given by:

$$\langle \sigma v \rangle = \sqrt{\frac{8}{\pi \mu}} \frac{1}{(kT)^{3/2}} \int_0^\infty \sigma(E) E e^{-E/(kT)} dE \ \text{cm}^3 \ \text{s}^{-1} \ \text{mol}^{-1}. \tag{2.10}$$

For a narrow resonance, one with a total width much smaller than the Gamow window, one can take the Maxwell-Boltzmann distribution, all the widths, and the de Broglie wavelength of the incoming particle to be constant across the resonance. Substituting in the formula for the resonant cross section given in equation 2.8 in to equation 2.10 and evaluating the integral results in an expression for the reaction rate per unit of time and unit of volume from a narrow resonance at a certain stellar temperature [86]:

$$N_A \langle \sigma v \rangle = 1.540 \times 10^{11} (\mu T_9)^{-3/2} \omega \gamma e^{-E_{res}/(kT_9)} \ \text{cm}^3 \ \text{s}^{-1} \ \text{mol}^{-1}. \tag{2.11}$$

Where N_A is Avogadro's number, μ is the reduced mass of the system, T_9 is the temperature in GK, $\omega \gamma$ is the resonance strength in MeV and E_{res} is the resonance energy in the centre of mass system in MeV. Thus, the reaction rate at

26

a certain stellar temperature, T, is dependent on the resonance energies and the resonance strengths of states in the Gamow window. The resonance strength for a target nucleus of initial state i capturing into a compound state f in a reaction (a, b) is given by:

$$\omega\gamma_{if} = \frac{(2J_f + 1)}{(2J_p + 1)(2J_i + 1)} \frac{\Gamma_{af}\Gamma_{bf}}{\Gamma_{totalf}}, \tag{2.12}$$

where

$\Gamma_{af} \equiv$ partial width of entrance channel for the compound nucleus state f

$\Gamma_{bf} \equiv$ partial width of exit channel for the compound nucleus state f

$\Gamma_{totalf} \equiv$ total width of channels for the compound nucleus state f.

Thus, for a nucleus in an initial state i, the resonant reaction rate over all compound nuclear states f above the reaction threshold, for narrow isolated resonances, is given by:

$$
\begin{aligned}
N_A \langle \sigma v \rangle_{\text{res}\, i} = {} & 1.540 \times 10^{11} (\mu T_9)^{-3/2} \\
& \times \sum_f \omega\gamma_{if} e^{-E_{res}/(kT_9)} \text{ cm}^3 \text{ s}^{-1} \text{ mol}^{-1}.
\end{aligned} \tag{2.13}
$$

In addition to the resonant capture into specific excited energy levels, the non-resonant capture into states into the residual nucleus will contribute to the reaction. The rate from this mechanism is described by the equation from Ref. [87]:

$$
\begin{aligned}
N_A \langle \sigma v \rangle_{\text{DC}} = {} & 1.86 \times 10^{7} (\mu T_9)^{-3/2} \\
& \times \sum_f S(E_0)_{if} e^{-23.195/T_9^{1/3}} \text{ cm}^3 \text{ s}^{-1} \text{ mol}^{-1},
\end{aligned} \tag{2.14}
$$

where $S(E_0)_{if}$ is the S-factor for a state f in the compound nucleus. The S-factor factors out the dependency of the Coulomb barrier from the cross section (σ), leaving a component that describes only the nuclear component of the reaction probability at a centre-of-mass energy E_{CM}:

$$S(E_{CM}) = \frac{E_{CM}}{\exp(-2\pi\eta)} \sigma(E_{CM}), \tag{2.15}$$

27

where η is the dimensionless Sommerfeld parameter:

$$\eta = \frac{Z_1 Z_2 e^2}{4\pi\epsilon_0 \hbar v},$$ (2.16)

where

$Z_1 Z_2 e^2 \equiv$ product of the charges of the reactants

$v \equiv$ magnitude of relative incident velocity.

For low temperature stellar environments, the direct capture rate will generally make the most significant contribution to the stellar reaction rate. However, in stellar environments at higher temperatures, if a resonance is present in the Gamow window of a reaction in a stellar environment, the resonant component of the rate can dominate over the non-resonant component [85].

Using equation 2.12, resonance strengths for a proton capture reaction (assuming other decay channels are not open, as is the case just above the proton threshold in ^{26}Si) are given by:

$$\omega\gamma = \frac{(2J_f + 1)}{(2J_p + 1)(2J_i + 1)} \frac{\Gamma_p \Gamma_\gamma}{\Gamma_p + \Gamma_\gamma},$$ (2.17)

where

$\Gamma_p \equiv$ proton partial width

$\Gamma_\gamma \equiv \gamma$ partial width.

Whenever one partial width is significantly smaller than the other, the smaller partial width will determine the resonance strength, e.g., for a proton capture reaction where $\Gamma_p \ll \Gamma_\gamma$ (with no other exit channels open), the resonance strength depends strongly on the proton partial width:

$$\omega\gamma = \omega \frac{\Gamma_p \Gamma_\gamma}{\Gamma_p + \Gamma_\gamma} \approx \omega \frac{\Gamma_p \Gamma_\gamma}{\Gamma_\gamma} = \omega\Gamma_p.$$ (2.18)

At excitation energies just above the proton threshold in nuclei, the proton partial widths of states are often smaller than the γ partial widths, meaning that resonant capture into these states is often dominated by the proton partial widths. As discussed in Chapter 4, this is the case for the 1^+ state in ^{26}Si just above the proton threshold, which is predicted to have a proton width many orders of

magnitude smaller than the γ partial width [86], meaning its resonance strength is likely completely determined by its proton partial width. This is also true to a lesser extent for the 0^+ state just above the proton threshold in ^{26}Si, which has a predicted proton partial width about half that of its γ partial width [86].

The partial width of a state (e.g. the proton partial width Γ_p), can be calculated as a product of its single-particle width, Γ_{sp} [88], which is defined as the FWHM of the resonance of a pure single particle state, and its spectroscopic factor, C^2S, which represents how much the state resembles that which would be described by the nuclear shell model as a pure "single particle" excited state:

$$\Gamma_p = C^2S\Gamma_{sp}. \tag{2.19}$$

The calculation of the single-particle width of a resonance state and the estimation of its spectroscopic factor will be discussed in the following subsections.

2.2.1 Determination of partial widths for astrophysically relevant resonance states

The single-particle width of a state is related to the reduced width γ^2 and barrier penetration probability $P(\ell,\,E)$ of that state [85]:

$$\Gamma_{sp} = 2\gamma^2 P(\ell,\,E). \tag{2.20}$$

The reduced width of a state can be calculated as follows [86]:

$$\gamma^2 = \frac{\hbar^2 c^2}{2\mu R_c^2}, \tag{2.21}$$

where
$\qquad \hbar \equiv$ the reduced Planck's constant
$\qquad c \equiv$ the speed of light in a vacuum
$\qquad \mu \equiv$ the reduced mass of the system
$\qquad R_c \equiv$ radius of the channel.

As well as the ℓ-transfer populating a state, the penetrability is sensitive to the
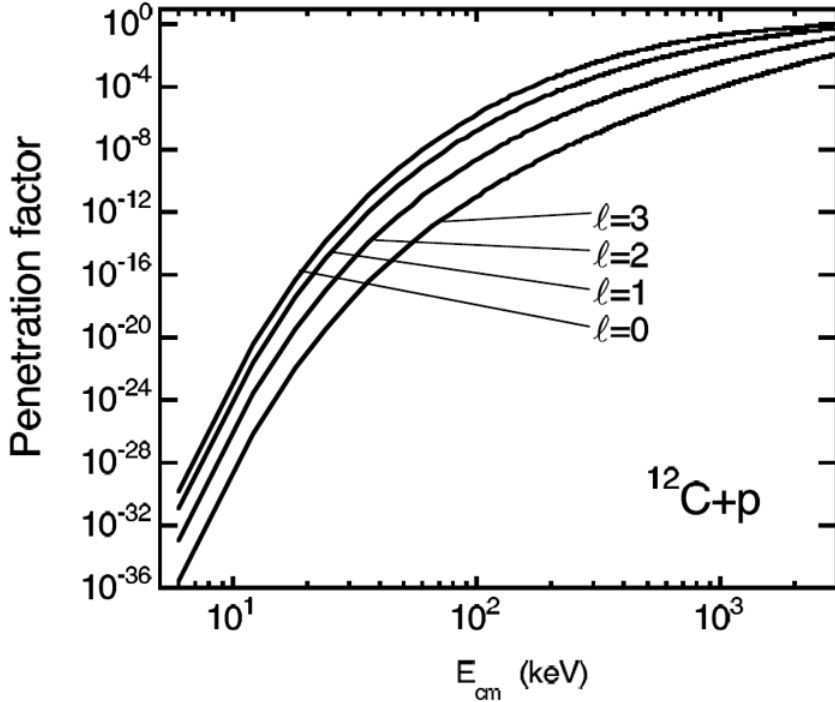
Figure 2.2 *Dependence of the penetrability factor on the ℓ-transfer and the centre-of-mass energy for the $^{12}C+p$ reaction [85].*

energy E of the system, as shown in Figure 2.2, which is dependent on the excitation energy of the state in the compound nucleus being populated.

The centrifugal barrier suppresses nuclear-fusion reactions, meaning reactions with lower orbital angular momenta are more likely to penetrate to the target nucleus and complete the reaction, as can be seen in Figure 2.2. If conservation rules permit a mixture of ℓ-transfers to populate a state, lower orbital angular momenta generally will have a higher penetrability likelihood, $P(\ell, E)$, i.e. s-wave resonances will dominate over p-wave resonances, which will dominate over d-wave resonances and so forth. This means the lowest permitted ℓ-transfer generally has the greatest effect on the partial width value when a mixture of ℓ-transfers can populate the state. For charged particle reactions, the penetrability factor of each ℓ-transfer that can populate a state have a different dependency on the centre-of-mass energy (shown in Figure 2.2). This means the centre-of-mass energy, and thus the excitation energy of the populated state, affects the relative contribution of angular momentum values to the particle width of the state.

This dependence of the partial widths on the orbital angular momentum values is much more pronounced in proton-capture reactions (e.g. ^{25}Al$(p, \gamma)^{26}$Si) than in α-capture reactions (e.g. ^{22}Ne$(\alpha, \gamma)^{26}$Mg and ^{22}Ne$(\alpha, n)^{25}$Mg).

30

Spectroscopic factors and partial widths of nuclear states can be estimated using shell-model calculations. For example, Richter *et al.* [86] used the Universal *sd*-shell B (USDB) model to calculate spectroscopic factors and proton partial widths for positive-parity states in the *sd* shell nucleus ^{26}Si below an excitation energy of 8 MeV. Spectroscopic factors (and by extension, partial widths) of nuclear states can also be extracted experimentally and are one of the most common properties to be measured in transfer reaction experiments.

2.3 Modelling transfer reactions using reaction theory

2.3.1 Transfer reactions to extract resonance properties of states

Transfer reactions are used to probe the single-particle strengths of nuclear states. This is quantified by comparing the experimental cross sections to those predicted by nuclear theory calculations for a single particle state to extract the spectroscopic factor of the state. The spectroscopic factor represents how much the state resembles that which would be described by the shell-model as a pure "single-particle" state [89], and is experimentally determined using the following equation:

$$\sigma_{exp} = C^2 S \sigma_{th}, \tag{2.22}$$

where $C^2 S$ is the spectroscopic factor of that state (with C the isospin Clebsch-Gordon coefficient) and σ_{exp} and σ_{th} represent the experimental and theoretical cross sections for that state respectively. The theoretical cross section, σ_{th}, of an excited state is found by calculating the cross section expected for a pure single-particle state, with distorted wave Born approximation (DWBA) calculations performed in the current work.

Using the (d, p) stripping reaction to study excited nuclear states is one of the most commonly used transfer mechanisms to gain knowledge about nuclear structure [90]. In the ^{25}Mg$(d, p)^{26}$Mg reaction described in this thesis, more than one ℓ-transfer may populate an excited state, depending on the spin/parity of that state, with the strength of each ℓ-transfer being described by an individual

spectroscopic factor.

The assumption of isospin symmetry to estimate properties of mirror nuclei (nuclei with proton and neutron numbers exchanged) is a useful tool for nuclear astrophysics, with Refs. [91] and [92] describing how the spectroscopic factors of the neutron-rich nucleus in a mirror pair can be used to estimate proton partial widths in the proton-rich nucleus in that pair. As described in Chapter 4, the experimentally measured neutron spectroscopic factors of states in ^{26}Mg will be used to estimate the proton spectroscopic factors in ^{26}Si, and thus provide estimates for proton partial widths of states relevant to the ^{25}Al$(p, \gamma)^{26}$Si reaction at nova temperatures.

Isospin symmetry of mirror states

Each nuclear state can be considered to have a total isospin of T, with a projection T_Z, which are conserved in nuclear reactions and decays. With convention defining the proton and neutron to have isospin projections $-\frac{1}{2}$ and $+\frac{1}{2}$ respectively, a nucleus of Z protons and N neutrons will have T_Z given by:

$$T_Z = (N - Z)/2. \tag{2.23}$$

For a state of given T, the value of T_Z will be in the range $T_Z = T, T - 1,...,-T$. As the interactions of protons and neutrons through the strong force are very similar, they can be considered to be projections of the same fermion. From this, mirror nuclei (those nuclei with numbers of protons and neutrons exchanged), are expected to have states with identical spins and parities. This property of nuclei is known as mirror symmetry, the validity of which is dependent on isospin conservation [93], and states in sets of nuclei with shared mass numbers and the same isospins are referred to as isobaric analogue states (IAS).

At lower excitation energies, with guidance from shell model predictions of the existence of states, identification of mirror pairs can be done with a high degree of certainty. In addition, light and medium mass stable nuclei tend to have simpler structures than more massive nuclei, due to single-particle excitations playing a more significant role in their structure than collective excitations. The nuclear interaction is expected to contribute only slightly to isospin-breaking effects in nuclei [94], and since the electromagnetic force is well understood, the difference in states originating in the Coulomb force can be easily described [94].

32

This means, for light and medium-mass nuclei, if the mass difference of the ground states of a mirror-pair is known, the energy level density at the excitation energy of interest is low enough, and the spin/parities of the excited states are well known, the assumption of isospin symmetry between states of the same J^π at similar excitation energies is a good approximation. Therefore, in circumstances where measuring properties of nuclear states directly is challenging, probing mirror states is an effective approximation for extracting properties of states, including spectroscopic factors. This approximation of isospin symmetry is used in Chapter 4 to estimate properties of states in ^{26}Si through the measurement of properties of states in its mirror nucleus ^{26}Mg.

As the excitation energy of a nucleus increases, the density of energy states increases. Due to this, determining which states are analogous between mirror nuclei become increasingly difficult at higher energies, even with guidance from shell models of which states are expected to exist. However, the nuclear interaction is expected to contribute only slightly to isospin-breaking effects in nuclei [94], and the electromagnetic force is well understood, so the difference in states originating in the Coulomb force can be easily described [94].

2.3.2 Direct and compound reaction mechanisms

The population of states through the (d, p) reaction can be described as happening through either a direct or a compound reaction mechanism, schematics of which can be seen in Figure 2.3. To describe the angular distributions of transfer reactions and thus extract accurate spectroscopic factors, fitting the experimental data with both reaction mechanisms is often necessary. This can be seen in Chapter 4, where some states of interest in ^{26}Mg for the ^{25}Al$(p, \gamma)^{26}$Si reaction required a compound contribution to model their angular distributions (see, for example, Figures 4.8 and 4.9).

By assuming that the fluctuations of excitation functions of intermediate processes sum to zero, the total cross section (σ) of a reaction can be assumed to simply be the sum of the direct and compound contributions [95]:

$$\sigma = \sigma_{DI} + R\sigma_{CN}, \tag{2.24}$$

where σ_{DI} is the direct reaction mechanism contribution, and σ_{CN} is the output from Hauser-Feshbach calculations (described in §2.4.1), scaled down by a reduction factor R [95].

The direct reaction mechanism tends to dominate (d, p) reactions at high beam energies, whereas the compound reaction mechanism is the dominant reaction pathway at low beam energies (generally contributing to the reaction yield at beam energies below 10 MeV [96]). At "intermediate" beam energies, both mechanisms can contribute to the reaction. For (d, p) reactions, this behaviour has been observed at beam energies between 6 and 12 MeV [97, 98].

In transfer reactions, the direct reaction mechanism involves the transferred nucleon (or set of nucleons) directly entering the excited state of the final nucleus, on a typically very short reaction time of roughly $\sim 10^{-22}$ s. The differential cross section of these reactions has a strong dependency on the angle the products are measured at, and so the angular distributions have distinct shapes, with unique angular distributions based on the orbital angular momentum transfer involved in the reaction. This reaction mechanism can be described using techniques like the DWBA, described in section 2.3.

In contrast, the compound reaction mechanism involves the incoming nucleus fusing with the target nucleus, creating a compound state, which decays to the final product nuclei. This reaction mechanism typically has a timescale of $\sim 10^{-18}$–10^{-16} s and gives nearly flat differential cross section angular distributions in the centre-of-mass frame. Statistical methods like the Hauser-Feshbach method have been used to calculate the compound component of reactions.
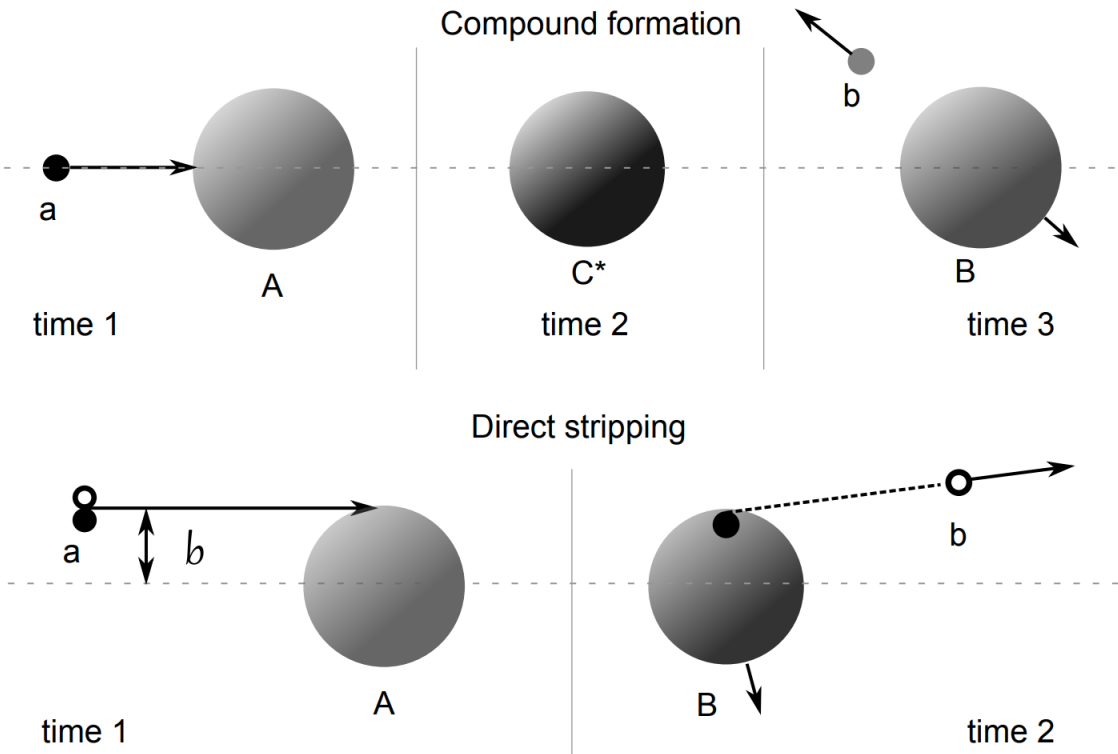
Figure 2.3 *Direct and compound reaction mechanisms for stripping reaction a(A, B)b reaction, with a compound nucleus C*. This illustrates how compound reactions are associated with smaller impact parameters (labelled b in this figure) in transfer reactions than direct reactions [96].*

Studies of the ^{24}Mg$(d, p)^{25}$Mg reaction have used the approach of summing the direct and compound reaction mechanisms to fit experimental angular distributions, as seen in Refs. [97–99]. Measurements of the ^{12}C$(^7$Li$, t)^{16}$O reaction to constrain resonance parameters for the ^{12}C$(\alpha, \gamma)^{16}$O reaction also used this method effectively [100, 101]. These studies calculated the contribution to the differential cross section angular distributions of the compound reaction mechanism using Hauser-Feshbach calculations, which are discussed in §2.4.1.

2.3.3   DWBA Theory Overview

The distorted wave Born approximation (DWBA) is a technique commonly used to model nuclear reactions. DWBA theory models the reaction using a single-step, first-order perturbation and has been used extensively to extract spectroscopic information from nuclear states by modelling transfer reactions, including (d, p)

reactions. The effects of the breakup of the weakly bound (BE=2.2 MeV) deuteron are not modelled in the reaction (although these effects may be included in the deuteron-target potential), however the study of Nguyen *et al.* [102] finds that the effects of finite-range deuteron breakup on the size of calculated cross sections are less than 10% at low energies (below 20 MeV/u). In this subsection, the neutron-transfer reaction A(d,p)B is considered, the co-ordinates of which are shown in Figure 2.4.
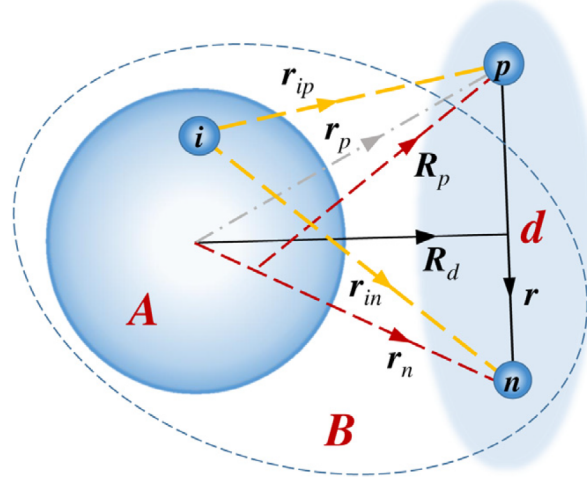
Figure 2.4 *Definitions of co-ordinate scheme for DWBA calculations [90].*

The DWBA amplitude for the (d,p) reaction, T_{dp}, is defined by the following expression:

$$T_{dp} = \sqrt{S} \int d\boldsymbol{r} d\boldsymbol{R}_d \chi_p^\dagger(\boldsymbol{R}_p) \phi(\boldsymbol{r}_n) V_{np}(\boldsymbol{r}) \psi_d(\boldsymbol{r}) \chi_d(\boldsymbol{R}_d), \qquad (2.25)$$

where χ_d and χ_p are the distorted waves describing the deuteron-target elastic scattering in the entrance channel, and the relative motion between the proton and the final nucleus, respectively. The single-particle wavefunction of the neutron transferred from the deuteron to the target state is represented by ϕ, while the ground state of the deuteron is represented by ψ_d. V_{np} represents the neutron-proton interaction in the incident deuteron, while the spectroscopic factor of the relevant state in the final nucleus is represented by S. The co-ordinates $\boldsymbol{r}$, $\boldsymbol{R}_d$, $\boldsymbol{R}_p$ and $\boldsymbol{r}$ are defined in Figure 2.4.

Often it is not practical to obtain the amplitude of the reaction directly from the representation in equation 2.25 and other forms must be derived. For example, the amplitude of the reaction f_{dp} at an angle θ can be calculated using the following

expression:

$$f_{dp}(\theta) \equiv -\frac{\mu_{pB}}{2\pi\hbar^2}T_{dp} = -\frac{\mu_{pB}}{2\pi\hbar^2}\int d\tau_{A+2}\chi_B^\dagger(\tau_B)\phi_p^\dagger\chi_{k_p}^\dagger(\boldsymbol{R}_p)$$
$$\times\left(V_{np}(\boldsymbol{r}) + \sum_{i\in A}V_{ip}(\boldsymbol{r}_{ip}) - U_p(\boldsymbol{R}_p)\right)\Psi_{k_d}^{(+)}(n,p,A), \qquad (2.26)$$

where μ_{pB} is the reduced mass of the p-B system and χ_{k_p} is a distorted wave. An auxiliary potential, U_p, is commonly chosen to take the flux from elastic scattering into account.

The differential cross section of the reaction $A(d,p)B$, $\frac{d\sigma_{dp}}{d\Omega}$, is related to the amplitude of the reaction at an angle θ, $f_{dp}(\theta)$, by the following equation:

$$\frac{d\sigma_{dp}}{d\Omega} = \left(\frac{v_{pB}}{v_{dA}}\right)|f_{dp}(\theta)|^2, \qquad (2.27)$$

where v_{pB} is the velocity of the proton relative to the target in the exit channel, and v_{dA} is the velocity of the deuteron relative to the target in the entrance channel. A more detailed formalisation of the DWBA, including its limitations, can be found in Ref. [90].

Many modern codes allow DWBA calculations to be performed, one of the most popular of which is FRESCO [103, 104], with several details of the reaction required to be specified, as described below.

2.3.4 DWBA Calculations

For both experiments described in this thesis, the differential cross section angular distributions were compared to finite-range DWBA calculations performed by the nuclear reaction program FRESCO [103, 104]. By providing the relevant nuclear information (including final state information and the potentials involved in the reaction) to the program, calculations for a single-particle state can be performed, with the differential cross section angular distribution outputted.

Input required for DWBA Calculations

The details of the final excited state of the target must be described in terms of what angular momentum transfer (ℓ) populates the state, the total angular

momentum (J) of that state, and the number of nodes in its wavefunction (equal to the principal quantum number of the state for FRESCO).

For the reaction A(d,p)B, there are five potentials to be described. This includes the potentials between A-d (the entrance channel potential), B-p (the exit channel potential), A-n (the potential experienced by the transferred neutron) and A-p (the core-core potential). These interactions are usually described with a Coulomb potential, a volume potential with real and imaginary components, a surface potential with an imaginary component, and a spin-orbit potential with a real component. The non-Coulomb potentials are commonly described by a Woods-Saxon shape:

$$V(r) = \frac{-V_0}{1 + \exp(\frac{r-R}{a})}, \tag{2.28}$$

where the potential has depth V_0, half-height radius R and diffuseness a. The other potential required to describe the reaction is the n-p potential in the deuteron, which is usually described by a Gaussian potential or a Reid soft-core potential. The parameters for these potentials are found by fitting to scattering data sets. The parameters for bound and unbound DWBA calculations used in the current work are described below.

In the first experiment described in this thesis, the experimental differential cross section angular distributions were compared to those expected for a pure single-particle state, calculated using the DWBA approximation with FRESCO, to extract spectroscopic factors for nuclear states.

A selection of optical parameter sets were considered, the beam energy and mass number ranges of which overlapped with our experimental configuration. By considering several different arrangements, the set that matched the shape of angular distributions most closely was chosen, shown in Table 2.1. An uncertainty of $\sim$20% in the extracted spectroscopic factor from the choice of parameters for modelling the reaction was estimated, based on the range in spectroscopic factors extracted when considering different parameter sets, for example Refs. [105, 106]. A Gaussian potential was used to describe the $p + n$ interaction in the deuteron, similar to that in Refs. [107, 108]:

$$V(r) = -V_0 e^{(-r/r_0)^2}, \tag{2.29}$$

where

$V_0 \equiv$ depth of potential

Potential	V_v	r_v	a_v	W_v	r_{wv}	a_{wv}	W_D	r_D	a_D	V_{so}	r_{so}	a_{so}	r_c
^{25}Mg + d [110]	83.9	1.17	0.81	0.0	1.56	0.83	18.6	1.33	0.60	3.70	1.23	0.81	1.70
^{26}Mg + p [111]	53.7	1.17	0.67	0.64	1.17	0.67	8.02	1.34	0.53	5.69	0.97	0.59	1.33
^{25}Mg + p [111]	53.7	1.17	0.67	0.64	1.17	0.67	8.02	1.34	0.53	5.69	0.97	0.59	1.33
^{25}Mg + n [112]	52.1	1.16	0.64	-	-	-	-	-	-	5.50	0.96	0.59	1.26

Table 2.1 *Optical model potential parameters used for DWBA calculations of angular distributions for states excited in the $^{25}Mg(d,p)^{26}Mg$ reaction, with a deuteron beam energy of 8 MeV. The entrance and exit channels of the reaction are described by the first two potential sets respectively. The third set refers to the core-core interaction in the reaction and the fourth corresponds to the binding energy of the residual nucleus. Energies are in MeV and distances in fm, with parameters having meanings are defined in Ref. [111].*

$r_0 \equiv$ root mean squared of potential.

Parameters of V_0=72.2 MeV and r_0=1.48 fm were chosen, extracted from the fitting of the potential to reproduce the deuteron binding energy, as performed in Ref. [109]. The other chosen parameter sets, as well as their corresponding channels and interactions, are shown in Table 2.1. In these finite-range DWBA calculations, the correct binding energies of the excited states of ^{26}Mg were produced by varying the depth of the central potential.

As the states measured in the second experiment in this thesis were close to or above the neutron threshold, the weakly bound approximation [113–115] was used for the DWBA calculations. This calculation involves forming an excited state at the relevant excitation energy, then giving it an artificial finite binding energy (0.2 MeV in the current work). As the artificial binding energy has little effect on the shape of the angular distribution, this approximation does not hamper efforts to distinguish between the shapes of different ℓ-transfers, and so is appropriate for the analysis performed for the second experiment in this thesis. The weakly-bound state approximation has been used previously in Refs. [116], [117] and [118] to model transfer reactions.

These DWBA calculations were again performed using FRESCO, with the potential parameters used shown in Table 2.2. As in the bound state calculations previously described, a Gaussian potential was used to describe the $p + n$ interaction of the deuteron, with parameters V_0=72.2 MeV and r_0=1.48 fm chosen.

Potential	V_v	r_v	a_v	W_v	r_{wv}	a_{wv}	W_D	r_D	a_D	V_{so}	r_{so}	a_{so}	r_c
^{25}Mg + d [110]	83.2	1.17	0.81	0.0	1.56	0.83	18.2	1.33	0.60	3.70	1.23	0.81	1.70
^{26}Mg + p [111]	51.7	1.17	0.67	0.67	1.17	0.67	8.39	1.34	0.53	5.58	0.97	0.59	1.33
^{25}Mg + p [111]	51.1	1.17	0.67	1.08	1.17	0.67	9.10	1.34	0.53	5.58	0.96	0.59	1.26
^{25}Mg + n [112]	50.5	1.16	0.64	-	-	-	-	-	-	5.37	0.96	0.59	1.26

Table 2.2 *Optical model potential parameters used for DWBA calculations of angular distributions for states excited in the $^{25}Mg(d,p)^{26}Mg$ reaction, with a deuteron beam energy of 13 MeV. The entrance and exit channels of the reaction are described by the first two potential sets respectively. The third set refers to the core-core interaction in the reaction and the fourth corresponds to the binding energy of the residual nucleus. Energies are in MeV and distances in fm, with parameters having meanings are defined in Ref. [111].*

2.4 Modelling the contribution of the compound reaction to the (d, p) stripping reaction

2.4.1 Hauser-Feshbach Theory

Hauser-Feshbach (HF) theory is a statistical model of nuclear reactions, of which the quantum mechanical formalism describing the reaction cross sections of final excited states was described in 1952 by Hauser and Feshbach [119]. The simplest form of the theory is based on the Bohr independence hypothesis, which assumes the decay of the compound nucleus is independent of its formation. This version of HF theory gives the cross section of entering a final state β as the product of the probability of forming a compound nucleus α and the probability of decay into a final state β:

$$\sigma_{\alpha\beta} = \sigma_\alpha P_\beta. \tag{2.30}$$

For a particular orbital angular momentum, the compound cross section for an incident particle of reduced de Broglie wavelength λ and transmission coefficient T_α populating a compound state α is given by:

$$\sigma_\alpha = \pi \lambda_\alpha^2 T_\alpha, \tag{2.31}$$

with the probability of decay to a final state β given by:

$$P_\beta = \lambda T_{\widehat{\beta}} = \frac{T_{\widehat{\beta}}}{\sum\limits_{\alpha} T_\alpha}, \tag{2.32}$$

where the time reversed states are designated $\widehat{\alpha}$ and $\widehat{\beta}$ and λ is a constant.

This finally gives the cross section of the formation of a compound nucleus α and that decaying in to a final state β:

$$\sigma_{\alpha\beta} = \pi\lambda_\alpha^2 \frac{T_\alpha T_{\widehat{\beta}}}{\sum\limits_\alpha T_\alpha},\tag{2.33}$$

giving effectively the simplest form of the Hauser-Feshbach formula [120].

Several improvements to this theory have been implemented over time. Correlations between the incident and outgoing waves in the elastic channel are taken in to account by the width fluctuation correction. In addition, the knowledge of nuclear structure that is used as an input into Hauser-Feshbach calculations has allowed more accurate calculations, including low-lying nuclear levels, separation energies, level densities, and γ-ray strength functions.

The use of Hauser-Feshbach calculations is only considered appropriate at a high density of excited states in the compound nucleus, as described in Ref. [121]. The Q value of the formation of the compound nucleus, ^{25}Mg+d$\rightarrow^{27}$Al, is 17139.80(7) keV [122]. When summed with the centre-of-mass energy 7.41 MeV (for a deuteron beam energy of 8 MeV), the compound nucleus is excited up to the level of roughly 24 MeV. An estimation of level densities for several spin/parities from Ref. [123], calculated using the configuration-interaction nuclear shell model, indicates that at $\sim$24 MeV in ^{27}Al, the energy level density is roughly 600 MeV^{-1}. The high level density at this excitation energy indicates that the use of the HF method for calculating the compound contribution is appropriate.

As direct non-elastic processes remove flux from the compound reaction mechanism, the compound cross section calculated by HF methods (which do not take in to account this loss of flux) will replicate the shape of the angular distribution of a compound reaction, but not the magnitude of the yield of the reaction. Thus, whenever HF calculations are fitted to experimental data, the theoretical cross sections are scaled by a reduction factor, R. This can be treated as a free parameter when fitting to experimental transfer reaction cross sections, provided R does not exceed 1 [95]. The Hauser-Feshbach calculations fitted to experimental data in this work (as shown in Chapter 4) all satisfy this limit. A more comprehensive discussion of progress in HF calculations and the limitations of statistical methods can be found in Ref. [124].

For (d, p) stripping reactions, the lower the beam energy used in a reaction, the more likely the differential cross section angular distribution of an excited state is to be dominated by a compound reaction mechanism, rather than a direct

reaction mechanism.

The expected compound contribution for an excited state is also dependent on the excitation energy of the state being populated. At higher excitation energies, excited states have a greater number of states open below to decay to. As the decay of a compound state is statistically more likely to populate an energy region of high energy density, the decay is more likely to move to a state of slightly lower energy than that of a significantly lower energy. The remainder of the excitation energy will be released in the ejected particle, resulting in a higher average energy of the particle being emitted. However, at these higher excited states, more channels are available to the excited compound nucleus. This means the probability of the state decaying via a single type of particle decay (e.g. purely proton decay) is reduced, as the exit channel flux will be taken up by other decay mechanisms.

2.4.2   Hauser-Feshbach calculations

To calculate the shape of the component of the experimental angular distributions that may correspond to the compound reaction mechanism in the first experiment presented in this thesis, the nuclear reaction program TALYS [125] was used. Hauser-Feshbach calculations of differential cross sections of the formation of the compound nucleus and subsequent emission of a proton at a range of angles were performed.

The Hauser-Feshbach calculations performed included width fluctuation correlations (WFC), which increase the size of the elastic channel and thus decreases the size of other open channels. A comparison of several methods of calculating WFC was performed in Ref. [126], which found the Moldauer method to be the most accurate, and so this was used in the calculations in the current work.

Chapter 3

Experimental Setup

3.1   Introduction and Overview of Facility

The two experiments described in this thesis were performed at the Triangle
Universities Nuclear Laboratory (TUNL) at Duke University, North Carolina,
U.S.A. This chapter describes the experimental set up used to collect the data in
both of these experiments.

The TUNL facility contains a 10-MV FN tandem Van de Graaff accelerator, a
recently re-commissioned Enge split-pole spectrograph and a detector system for
the purpose of performing high-resolution spectroscopy measurements (with the
possibility of γ-particle coincidence measurements) for reactions of interest to
nuclear astrophysics. The layout of the tandem lab is show in Figure 3.1.
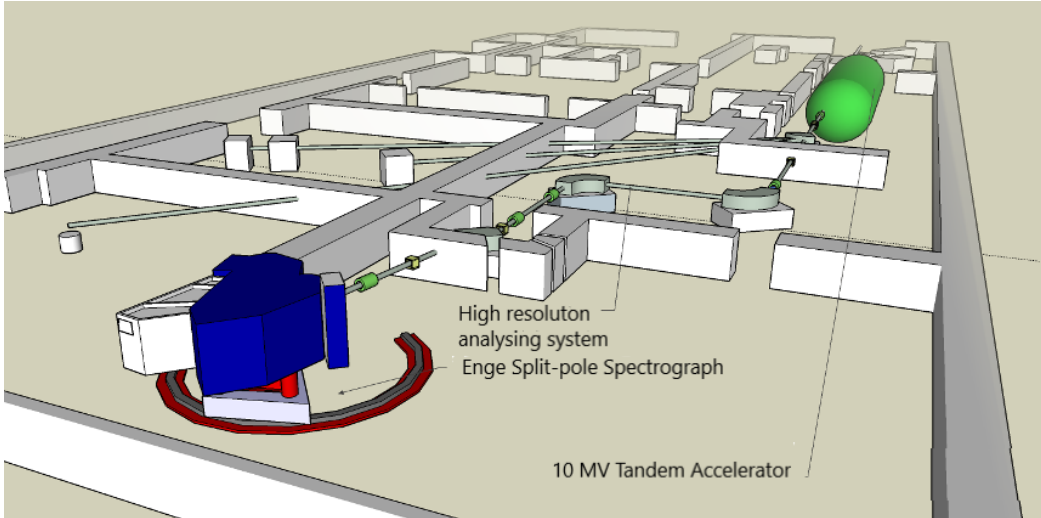
Figure 3.1 *Model of the TUNL laboratory, showing the tandem accelerator, analysing system and spectrograph [127].*

3.2   Tandem Accelerator

The 10-MV FN tandem Van de Graaff accelerator at TUNL, shown in Figure 3.2, is able to produce beams of charged particles, including ^{1}H, ^{2}H, ^{3}He and ^{4}He, in either pulsed or DC form. The negatively charged ions from the ion source are attracted towards the centre of the tandem accelerator, where a carbon foil strips them of their electrons, before they are accelerated towards the high energy end of the accelerator. Ions passing through the tandem accelerator gain an energy $(q + 1)V$, where q is the charge of the particle being accelerated and V is the terminal voltage of the accelerator. The tandem accelerator and beam stabiliser are described in detail in Ref. [128]. After the tandem, two 90 $^\circ$ magnets provide high-resolution momentum analysis of the beam line. These two magnets share a power supply, facilitating calibration of the beam energy. Both magnets contain a nuclear magnetic resonance (NMR) probe, which controls and measures the magnetic fields produced. The frequency of the NMR in MHz, f, is related to the energy of the beam, E, by the following relation:

$$K = \left(\frac{ME}{q^2 f^2} \right) \left[1 + \frac{E}{(2Mc^2)} \right], \tag{3.1}$$

where

$\quad K \equiv$ the magnetic calibration constant

$\quad q \equiv$ the charge of the particle in the beam

$\quad M \equiv$ the mass of the particle in the beam in amu

Figure 3.2 *TUNL FN tandem Van de Graaff accelerator.*

$Mc^2 \equiv$ the rest mass of the particle.

The original beam energy calibration was performed by fitting the proton energies of various threshold and resonance reactions, which have had their Q values measured previously, against the magnet calibration constant, K [129]. This allows the beam energy to be derived from the NMR frequency, measured by the gaussmeter, used in the two $90°$ magnets, within ± 2 keV, using equation 3.1.

3.3 Spectrograph

The use of magnetic spectrographs to measure the energy of charged particles is a method that has been used in nuclear physics research since the earliest studies of radioactivity, and has remained popular in modern times. While various detectors can determine the energy of particles, including ionisation chambers, scintillation counters and solid-state counters, the magnetic spectrograph provides a low

signal-to-background ratio with a very high resolving power, that in theory is not limited. This contrasts with other detectors, for example, solid-state counters, which have intrinsic limitations.

In a magnetic field of strength $\mathbf{B}$, a charged particle with a velocity $\mathbf{v}$ and charge q is subject to a force $\mathbf{F}$, perpendicular to its velocity:

$$\mathbf{F} = q(\mathbf{v} \times \mathbf{B}). \tag{3.2}$$

Magnetic spectrographs utilise this force so that particles with the same charge but different momenta (energies) will experience different turning radii in a magnet (where the applied magnetic field is perpendicular to the motion of the particles), focusing them on separate positions on a focal plane.

Thus, a magnetic field of constant field direction will move a charged particle of momentum p in a circle of radius ρ, given by the following equation:

$$B\rho = \frac{p}{q}. \tag{3.3}$$

The quantity $B\rho$ is referred to as the magnetic rigidity. For particles of the same charge, this equation shows how the momentum of a particle is proportional to its magnetic rigidity. This results in charged particles of different momenta (and thus energies) becoming spatially separated whenever they traverse the spectrograph. Charged reaction products from experiments performed are then focused on to the focal plane of a spectrograph, where their position and other properties can be detected [130].

Enge Split-pole Spectrograph

Harald Enge first designed the Enge Split-pole Spectrograph while working for High Voltage Engineering Corporation, in an effort to increase the solid angle for spectroscopy experiments. An Enge split-pole spectrograph, like the one used in this work, separates charged particles of different magnetic rigidities using two magnets powered by the same coils, and thus with the same magnetic field strength [131]. This allows higher precision spectroscopy via double focusing, second-order aberration corrections and additional vertical focusing. The design
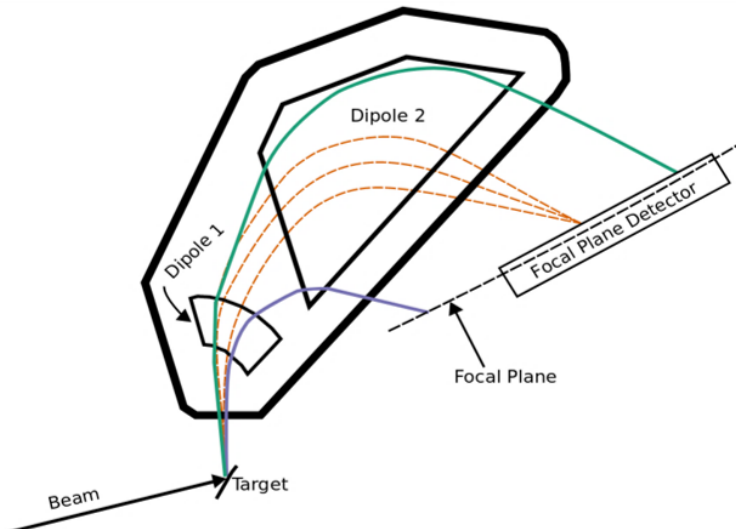
Figure 3.3 *Schematic of Enge split pole spectrograph, showing the two dipole magnets focusing charged particles on to the focal plane [132].*

of a split-pole spectrograph can be seen in Figure 3.3. The focal plane in the TUNL Enge split-pole spectrograph is slightly curved and charged particles are focussed on to this, lying at an angle of $41.5\,^{\circ}$ to the magnetic exit.

3.4   Spectrograph Focal Plane Detector System

Charged particles were accepted by the high-resolution Enge split-pole spectrograph, with a magnetic field strength of 0.66 T used in the current work, before being focussed on to the focal plane of the spectrograph, where their channel positions are recorded by the position-sensitive detector system described in §3.4.2 and their energy loss and residual energy for the purpose of particle identification were recorded by the detector system described in §3.4.3. The path of charged particles through the TUNL detector is shown in Figure 3.4.
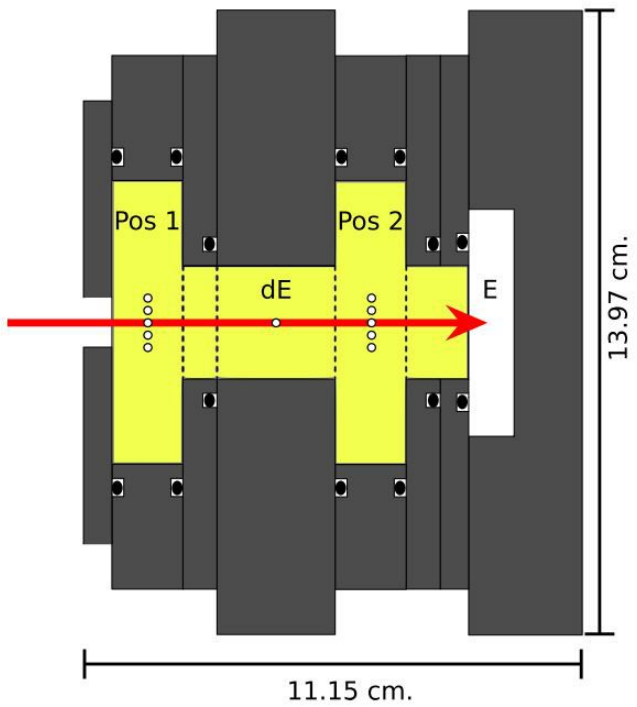
Figure 3.4 *Entire detector package used at the TUNL spectrograph. The direction of particles leaving the spectrograph is indicated by the red arrow, with the gas filled regions shown in yellow. The individual gas-filled detectors are separated by aluminised mylar and filled with gas isobutane at a pressure of 200 Torr [132].*

3.4.1 Detection of charged particles by gas detectors and scintillators

A variety of detectors are utilised in modern nuclear physics experiments, including ionisation chambers, proportional counters, Geiger-Muller tubes and scintillators. Each of these have their own advantages and disadvantages, and so are chosen depending on the needs of the experimental set up.

The detection of any type of particle in a detector is based on how that particle interacts with matter and loses its energy. In the case of the detection of charged particles, e.g. protons, the Coulomb interaction results in energy loss as the positively-charged particle passes through the material, depositing part of its energy and possibly exciting or removing the negatively charged orbital atomic electrons from their constituent atoms (ionisation). Charged particles interact with many atomic electrons as they pass through the material, with each individual reaction only removing a small proportion of the charged particle's total energy, giving the particle a nearly straight path through the material. The

induced ionisation processes create many electron-ion pairs along its trajectory through the detector, leaving a path of ionisation in the charged particle's wake. Gas-filled detectors, like the ones used in the particle positions and energy loss measurements in the current work, are based around the principle of detecting this ionisation, which is proportional to the energy of the incoming charged particle [133].

Often too few ion-electron pairs are produced by a charged particle in a detector for direct detection, and so proportional counter detectors amplify the original charge produced using gas multiplication. This involves applying an electric field to the detection gas with a high enough voltage to accelerate electrons liberated from atomic orbitals to significant kinetic energies (positive and negative ions have too large an inertia to participate significantly in this process). If the liberated electron gains a high enough kinetic energy, it may in turn liberate another atomic electron, which may cause further ionisation using the same mechanism. This cascade of charge produced is known as a Townsend avalanche and greatly increases the charge resulting from the interaction of a charged particle with a gas detector, as can be seen in Figure 3.5. Once again, the size of the electrical pulse produced will be proportional to the kinetic energy of the incoming charged particle [133].

The detection of charged particles by scintillating materials is based on the principle of charged particles exciting the bound electrons of the molecules that comprise the scintillator, which then de-excite and emit light. This light is then converted in to a usable electrical signal by a photomultiplier tube or a photo diode [133]. This type of detector is used in the detection of the residual energy of charged particles in the current work.
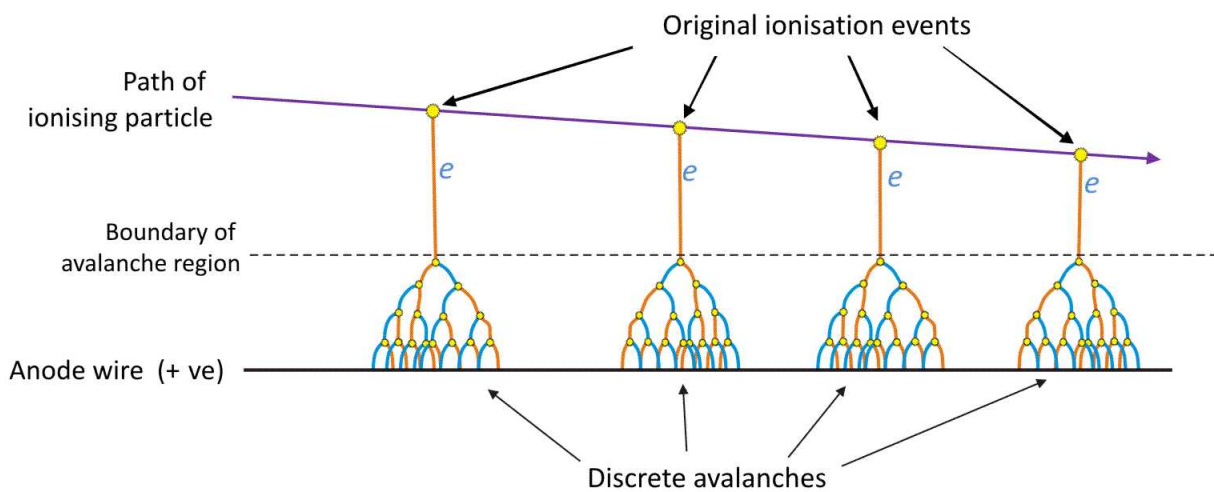
Figure 3.5 *Diagram of discrete avalanche counter events in a proportional counter [134].*

3.4.2   Position-Sensitive Detection System

The first and third detectors struck by particles accepted by the detector system consisted of position-sensitive avalanche counters. This is shown in Figure 3.4, with the two detectors measuring the positions of the incident particles on the TUNL spectrograph.

At the entrance of each of these detectors, an etched cathode foil consists of several electrically isolated strips. As a charged particle passes through the detector, it ionises the fill gas, inducing an electron avalanche on the anode wire at the centre of the counter. This in turn induces a positive charge on the cathode foils - the etched cathode foil at the entrance of the detector and the ground foil at the exit of the detector.

The strips in the etched cathode foil are connected together by a delay line, increasing the time delay between strips that correspond to a certain detection position. With the charge measured over multiple strips, a distribution of the charge can be interpolated, as shown in Figure 3.6. This improves the charge spatial resolution to sub-mm levels, instead of being limited by the strip width. The grounded cathode foil on the exit of the position section helps isolate and shape the electric field from the anodes. A cartoon of the position section and its principle of operations can be found in Figure 3.6. In the current work, both the forward and backwards position-sensitive detectors were biased with voltages of +1800 V, with particles focussed on the centre of the front position system.
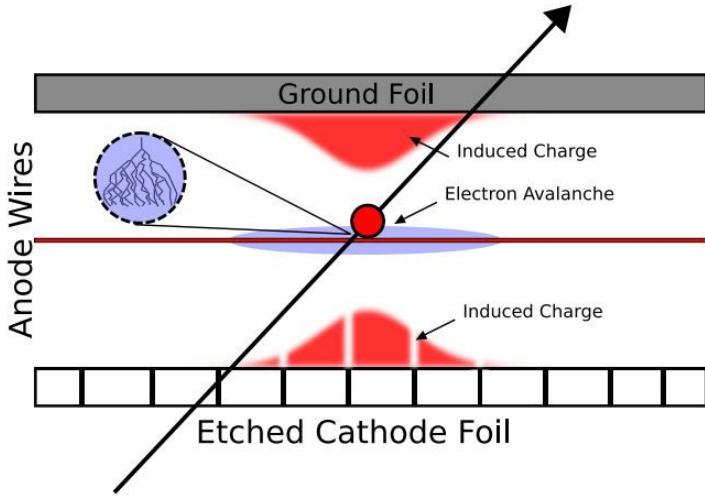
Figure 3.6 *Cartoon of one of the position-sensitive avalanche counters that comprise the position-sensitive component of the focal-plane detector system [132].*

Although not used in the work described in this thesis, particle tracing is possible with this detector system.

3.4.3 Particle Identification System

The second and fourth detectors are used for the identification of the types of incident particles, and consist of a gas proportional counter, which measures the energy loss of the particle (ΔE), and a plastic scintillator which stops the particle and measures its remaining energy (E), as shown in Figure 3.4.

This allows the identification of different species of particles leaving the spectrometer, as can be seen by the clear separation of different charged particles in Figure 3.7.

Energy Loss (ΔE) Detector

A gas proportional counter comprises the ΔE section of the detector system. The anode consists of a single wire, with the back cathode consisting of a strip of aluminised mylar and the front cathode sharing the front position-sensitive detector's grounded cathode plane. This detector was biased with a voltage of

51
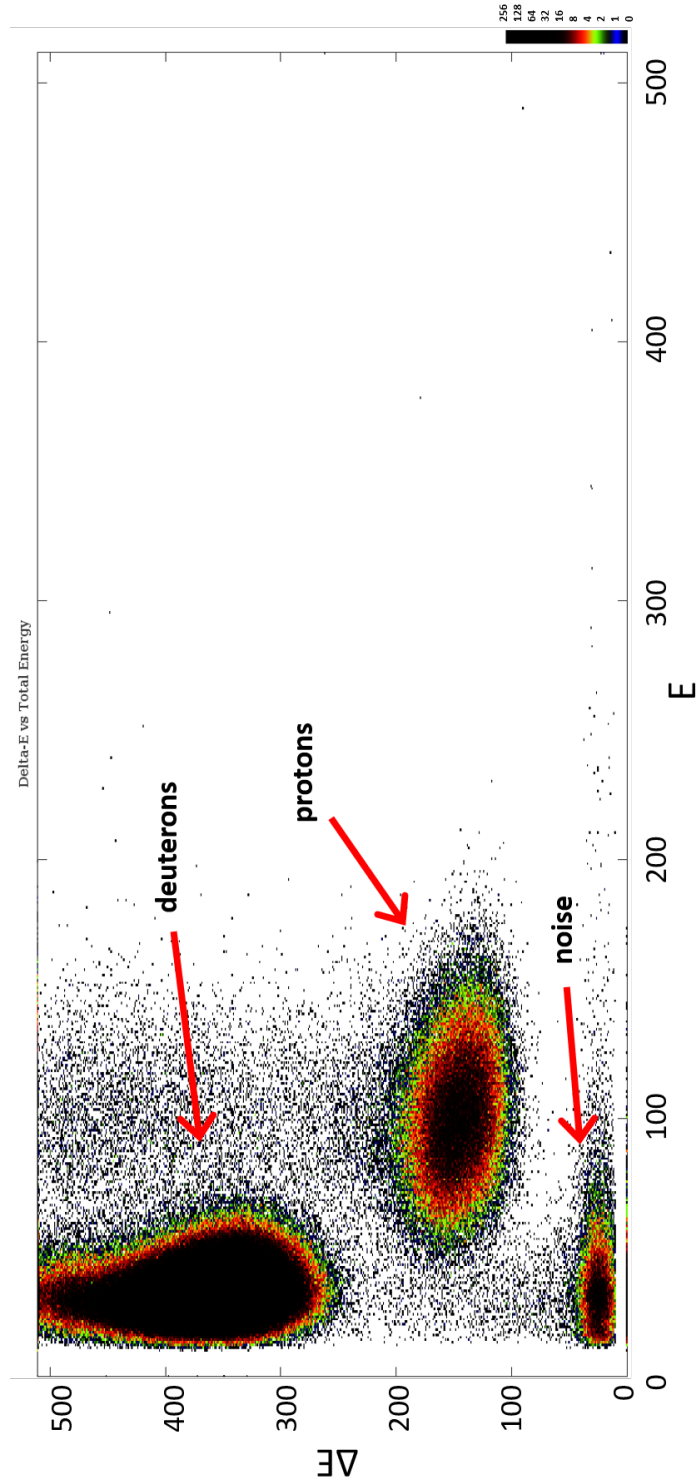
Figure 3.7 *Example* $\Delta E - E$ *plot showing* ΔE *against E for an experimental run, with a beam energy of 8 MeV and charged particles measured at a lab angle of 13°. The counts at (100, 150) correspond to detected protons, with the counts at higher values of* ΔE *produced by detected deuterons and the counts near the origin originating from noise.*

+500 V in the current work.

Residual Energy (E) Detector

The residual energy of the particles is absorbed as they stop in this detector, which is made of a Saint-Gobain BC-404 organic plastic scintillator. The fast timing response of this material (with a rise time of 0.7 ns [135]) makes it ideal for the trigger for the data acquisition system, and its dimensions have been customised to cover the length of the detector, ensuring all light particles will stop in the material. This detector is wrapped in thin, reflective aluminium foil to maximise light collection while maintaining a sealing surface against the rest of the detector system.

Bicron BCF-91A optical fibers of 1 mm diameter collect the light output from eight grooves in the scintillator, and bend it into a photomultiplier tube (PMT), which produces a measurable electrical voltage. The PMT used is a Hamamatsu H6524, chosen as it has the highest quantum efficiency for the wavelengths of interest, peaking at 27% [136].

A voltage of -1600 V was provided to this detector in the current work.

In the current work, the protons detected by the Enge spectrometer's focal plane were easily separated from background noise and other charged particles, i.e., deuterons, by selecting events at the appropriate position on the $\Delta E - E$ plot, using JAM [1] [137], which can be seen in Figure 3.7.

3.4.4 Detector Readout and Electronics

This subsection describes the hardware and electronics used to collect the detector signals in the current work. A schematic of the electronics for all four detectors is shown in Figure 3.8.

---

[1]https://sourceforge.net/projects/jam-daq/
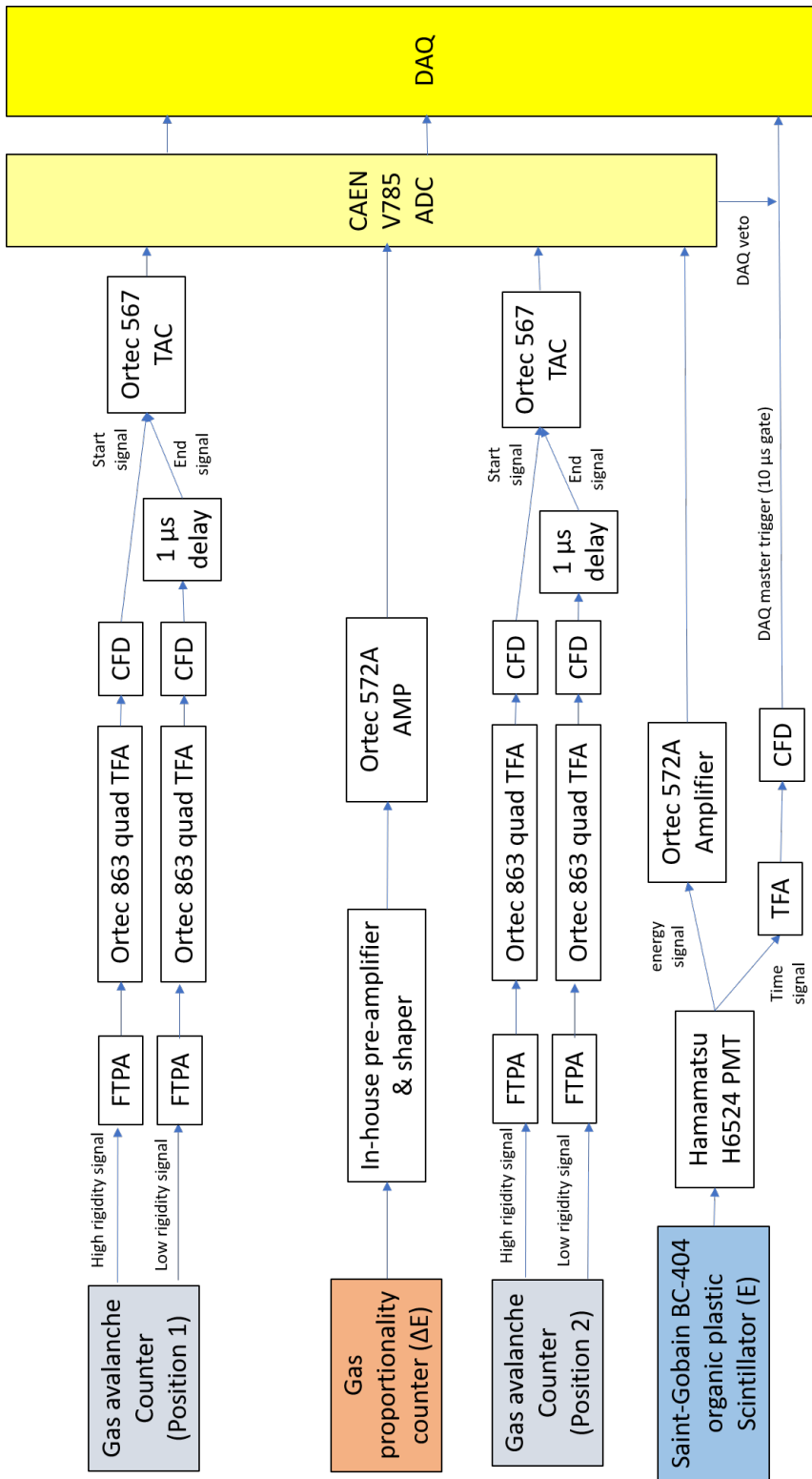
Figure 3.8   *A schematic of the electronics setup for readout from the focal plane detectors used in the current work.*

In the position-sensitive detection system, 5 ns of delay is provided by each tap in each delay chip, of model Data Delay Devices 150750A, with a 50 Ω impedance to match the signal cables. The 10 taps in each of the 20 chips in the delay line thus provide a total of 1 μs of delay. The signal cables are connected to the delay lines with a vacuum type method by Bayonet Neill-Concelman feedthroughs, attached to national pipe taper (NPT) threads. The relationship between the delay time and position of the electrical charge can be non-linear, with non-linearity in this conversion minimised by keeping a ratio of around 0.8 between the cathode strip width (2.54 mm) and the separation of the anode and the cathode (3.00 mm), as suggested in Ref. [138]. As each of the two position-sensitive detectors has a readout on each side of high and low magnetic rigidity, four position signals are generated whenever a charged particle passes through the position-sensitive detection system, as can be seen in Figure 3.8, coming from the gas avalanche counters. Each of these signals is preamplified through a fast-timing preamplifier, before being shaped in an Ortec 863 quad timing filter amplifier (TFA). The output levels of the TFA are roughly 300 mV, and so the thresholds on each channel are matched to be just below this value. A constant fraction discriminator (CFD) performs the final noise rejection and shaping on the signal. An Ortec time-to-amplitude (TAC) converter is started by the signal from the high magnetic rigidity end of the detector and ended by the signal from the low magnetic rigidity end of the detector, which is subject to a 1 μs delay. The output from the TAC is then recorded for later analysis by a CAEN V785 peak-sensing analog-to-digital converter (ADC).

The residual energy scintillator is connected to a PMT, which collects the light from the scintillator and produces a dynode signal, providing separate timing and energy signals. An Ortec 572A amplifier processes the energy signal, which is then recorded. Each event count is generated by the timing signals passing through a TFA and CFD, which shapes the pulse and rejects noise, which triggers the master gate in the data acquisition (DAQ) system. A 10 μs gate is produced and the ADC saves all coincident signals (providing the ADC buffer is not full and thus will not veto the trigger). As can be seen in Figure 3.8, the low rigidity signals from the position-sensitive detectors are subject to a signal delay, meaning signals from this side of the focal plane will be recorded later than those from the same location on the high-rigidity side of the focal plane. This means a gate produced by the position section would induce some position-dependence on the gate timing. However, the E detector is used to produce the gate, thus removing the charged particle position dependency from the gate timing. The monitoring

of beam currents and diagnosis of electronics problems is made easier by this set up, with count rates recorded for all detector signals, gates generated, and gates vetoed by an ADC busy signal.

An in-house charge-sensitive preamplifier based on the Cremat CR-110 operational amplifier preamplifies and provides a 1 μs shaping time to signals from the ΔE detector. Afterwards, an Ortec 572A amplifier shapes the signal, which is then sent to the ADC.

3.5 Setup of experimental target for the present experiments

The ^{25}Mg$(d, p)^{26}$Mg experimental campaign performed at TUNL in August 2018 consisted of two similar experiments measuring the angular distributions of excited states of ^{26}Mg of interest to astrophysically important reaction rates. Two separate targets were used in these experiments consisting of two thin targets of ^{25}Mg, isotopically enriched to a nominal value of 99.2$\pm$0.1 %, manufactured at Argonne National Laboratory and transported to TUNL under vacuum. The two targets had nominal thicknesses of 90 and 112 μg/cm^2, supported on gold foils of 165 and 170 μg/cm^2 thicknesses respectively. These thicknesses were found by measuring the energy loss of alpha particles passing through the targets, with an estimated uncertainty of $\pm$10 %.

Gold was chosen as the target support for several reasons. A support of carbon would increase the number of counts from contaminant reactions on carbon isotopes. This was an issue in previous measurements of the ^{25}Mg$(d, p)^{26}$Mg reaction, where protons from the population of the key 0^+ 6.125 MeV state of ^{26}Mg arrived at a similar position on the focal plane to those produced in the ^{12}C$(d, p)^{13}$C(g.s.) reaction (see Refs. [139, 140]). Aluminium was also considered as a backing, but due to the similarities in atomic masses and the Q values of the ^{25}Mg$(d, p)^{26}$Mg (Q value=8868.51 keV [141]) and the ^{27}Al$(d, p)^{28}$Al (Q value=5500.53 keV) reactions, a large overlap of protons from excited states was expected, so this idea was discarded. In addition, the isotopic purity of gold reduces the expected number of contaminant peaks from the target support.

The energy loss of particles through the target can contribute significantly to the resolution capabilities of the experiment and so, by using thin targets, the resolution of the experiment was maximised. The outgoing proton from the

56

^{25}Mg$(d, p)^{26}$Mg reaction will lose energy less rapidly than the incoming deuteron, due to its smaller mass and energy boost received from the positive Q value of the reaction. With this in mind, the targets were orientated with the magnesium side upstream of the beam, instead of the gold backing. This further minimised the energy loss the system experienced, leading to the high resolution that can be seen in Figure 3.9.

The main nominal impurities in the target consisted of other magnesium isotopes: 0.47 % ^{24}Mg and 0.33 % ^{26}Mg. The next abundant impurities were iron (800 ppm), calcium (<100 ppm) and sodium (47 ppm). This isotopic analysis was performed by Trace Sciences International and cosigned by Argonne National Laboratory, the results of which can be found in Appendix A. While no impurities from carbon, oxygen or hydrogen are mentioned in the analysis certificate, and the amount of time each target was exposed to the atmosphere was minimised, the spectra showed that the target became contaminated with an amount of these organic chemicals as the experiment progressed, likely originating from sources like oil pumps in the beam line and attaching to the target as it is heated.

For each run, the proton counts were binned as a function of channel number, allowing the events corresponding to each excited state populated by the (d, p) reaction to be observed. The background counts that could not be assigned to a known excited state were very low.
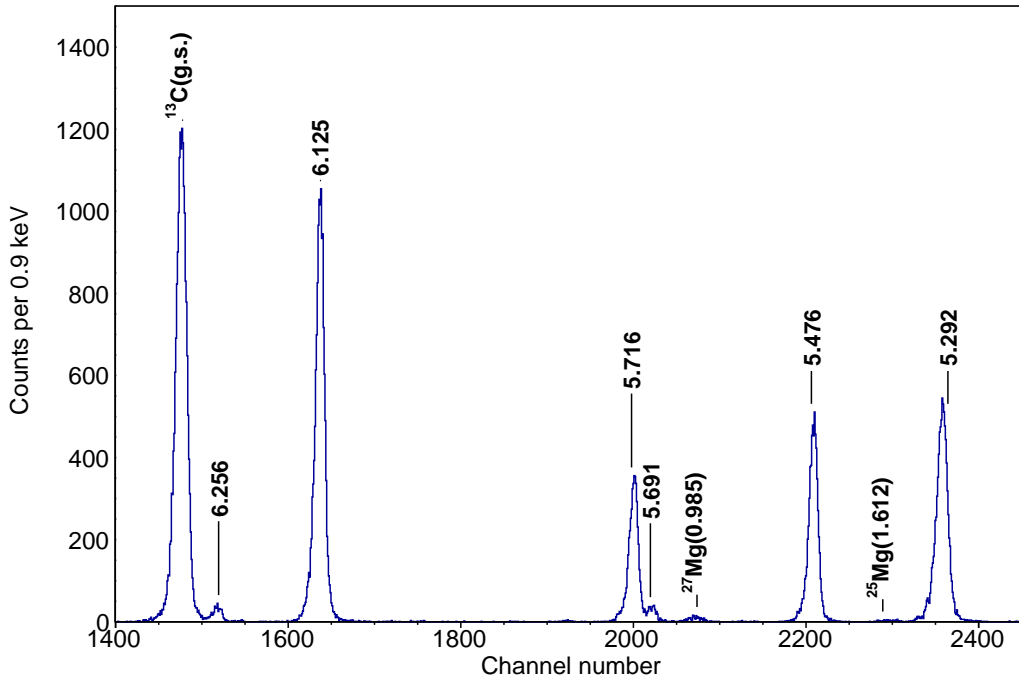
Figure 3.9 *Energy spectrum of protons from the $^{25}Mg(d,p)^{26}Mg$ reaction, measured at $\theta=30°$. Peaks corresponding to the excited states of ^{26}Mg are labelled with their excitation energy in MeV, taken from Ref. [81]. The final excited states of contaminant peaks are also labelled.*

3.5.1 Calculation of experimental cross sections

Experimental differential cross sections in the lab frame $\frac{d\sigma}{d\Omega}$ were calculated as follows:

$$\frac{d\sigma}{d\Omega} = \frac{Y}{I_d n \Delta\Omega(1-\tau)},$$
(3.4)

where

$Y \equiv$ yield of protons for that peak in a run

$I_d \equiv$ number of deuterons in a run

$n \equiv$ number density of ^{25}Mg in the target

$\Delta\Omega \equiv$ solid angle of acceptance of particles from target

$\tau \equiv$ fraction of deadtime in a run.

Charge from the beam was collected by a Faraday cup at a position of $0°$, which

58

sent signals to a Brookhaven current integrator (BCI), set to give a logic pulse every 10^{-10} C of charge deposited. Therefore, the number of deuterons in a run, I_d, was found as follows:

$$I_d = \frac{BCI}{e} \times 10^{-10},$$ (3.5)

where e is the elementary charge in coulombs. A low voltage applied to the Faraday cup suppressed the production of secondary charges, ensuring the beam current was not overcounted.

The nominal target thickness in units of $\mu g/cm^2$ is represented as ρ. To convert the target thickness to a number density in units of cm^{-2}, n, the following equation was used:

$$n = \frac{\rho N_A \times 10^{-6}}{A},$$ (3.6)

where

$N_A \equiv$ Avogadro's constant,

$A \equiv$ mass number of nuclei in target (25 in these experiments).

The DAQ system recorded the time for each run (RUNTIME) and the time spent unable to take a new reading (BUSY), allowing the fractional dead time (typically $\tau \leq 0.01$) to be calculated as:

$$\tau = 1 - \frac{\text{BUSY}}{\text{RUNTIME}}.$$ (3.7)

The angles and differential cross sections were transformed from the lab frame to the centre-of-mass frame using the method described in Appendix B.

3.5.2 Beamtime runs and condition monitoring

The first experiment described in this thesis aimed to measure the angular distribution of states in ^{26}Mg at excitation energies around 5.5-6.3 MeV, corresponding to mirror states in ^{26}Si of astrophysical interest, the results of which are presented in Chapter 4. A beam of energy 8 MeV was used in this

experiment. While previous studies of the ^{25}Mg$(d, p)^{26}$Mg reaction used a higher beam energy (see Refs. [139, 140]), this beam energy was chosen to separate protons from the ^{12}C$(d, p)^{13}$C(g.s.) reaction and protons corresponding to the 6.256 MeV 0^+ state in ^{26}Mg state. The 0^+ 6.256 MeV state of interest is populated by an ℓ=2 angular momentum transfer in the (d, p) reaction, which peaks around 25-30°, roughly around where the 0^+ state overlaps with the peak corresponding to protons from the ^{12}C$(d, p)^{13}$C reaction. Due to the Coulomb barrier between ^{25}Mg and a deuteron being around 3.3 MeV, very low beam energies were also not suitable for this experiment.

As a carbon nucleus is lighter than a magnesium nucleus, the carbon contaminant peak will move to higher focal plane channel numbers at a faster rate as the measured angle increases than a peak corresponding to an excited state of magnesium will. This results in the 6.256 MeV state appearing at lower channel numbers than the carbon peak at small angles, and at higher channel numbers at larger angles.

The beam energy used is less than that typically employed in transfer studies for nuclear astrophysics ($\sim$5-10 MeV/u), and so increases that the likelihood of the compound reaction mechanism being included in the reaction, in addition to the direct reaction mechanism.

Measurements of the reaction products were taken at multiple lab angles between 13-55°, with separations of typically 3° between measurements, providing good coverage of the range where the DWBA calculation of the ℓ=2 transfer that populates the 0^+ state could be well fitted.

An energy resolution across these angles of 13-14 keV FWHM was measured from fitting a Gaussian distribution to the peaks, and no damage to the targets appeared in the spectra.

The second experiment described in this thesis studied higher energy excited states, above the alpha threshold in ^{26}Mg, S_α=10.615 MeV, using a 13 MeV beam to populate states. Across all angles, an energy resolution of 14-16 keV FWHM was achieved.

Measurements were taken at lab angles ranging from 10-39°. These angles were chosen as these forward angles are the best described by DWBA calculations, thus allowing discrimination between different ℓ-transfers populating each state. Measurements at angles smaller than 10° degrees were not possible due to issues with vacuum seals at small angles and the high elastic scattering rate at these angles. Beam time runs would typically last for an hour, to ensure a significant

60

number of counts had been measured for the states of interest. The DAQ trigger rate varied between ∼50-1000 Hz. The spectra were checked regularly during runs, to ensure that significant peak counts were being recorded for each peak, and online fitting of spectra allowed monitoring of peak profiles, ensuring there was no broadening of the peaks, which would have indicated target damage. During the runs, the dead time was kept under 1%. Ongoing monitoring of the rates allowed a balance to be found between keeping the count rate high enough to get a large number of statistics while ensuring the deadtime did not get too high. For the lower energy experiment, this was done by varying the beam current on the target between ∼250-300 nA and opening the solid angle of acceptance of the protons between 0.5 and 1.0 msr. For the higher energy measurement, the beam current was varied between ∼150-270 nA, with a solid opening angle between 0.5 and 1.0 msr.

Chapter 4

Study of states populated in the ^{25}Mg(d, p)^{26}Mg reaction for the ^{25}Al(p, γ)^{26}Si rate in nova burning conditions

4.1 Astrophysical background and previous work to constrain the ^{25}Al(p, γ)^{26}Si reaction rate

The study of the states of interest in ^{26}Mg discussed in this chapter have been reported in a peer-reviewed publication of which I was the principal author (see Ref. [1]).

At the temperatures involved in novae, the ^{25}Al$(p, \gamma)^{26}$Si reaction proceeds through resonances in ^{26}Si corresponding to excited states just above the proton threshold, S_p=5.51401(11) MeV [63]. Four excited states in ^{26}Si in the relevant Gamow window for the reaction have been observed, including states at 5.676, 5.890 and 5.929 MeV of spin/parities of 1^+, 0^+ and 3^+ respectively, and a state at 5.946 MeV with uncertain properties. Only the 3^+ state has had its resonance properties measured in the ^{26}Si nucleus thus far, through measurements of the proton and γ partial widths of the state.

The 1^+, 0^+ and 3^+ states mentioned have had their mirror states identified in ^{26}Mg at energies of 5.691, 6.256 and 6.125 MeV respectively, as seen in Figure

4.1, which shows the current understanding of states of ^{26}Mg matched to mirror states of ^{26}Si relevant for the ^{25}Al$(p, \gamma)^{26}$Si reaction in novae. The state in ^{26}Mg at 5.716 MeV has been matched to a mirror 4^+ state in ^{26}Si, but as this state lies below the Gamow window at nova temperatures, it has no known astrophysical significance. A γ-ray study from Ref. [142] measured a γ ray associated with the decay of an excited state in ^{26}Mg at 5.711 MeV to a lower-lying 0^+ state, in addition to γ rays corresponding to the neighbouring states at 5.691 and 5.716 MeV that have already been mentioned. Transition rules indicate that the decay of the state at 5.711 MeV to a 0^+ state would only be possible for a state of $J=(1, 2)$. No corresponding mirror state in ^{26}Si has been confirmed for this state thus far.

Studies of the resonance properties of these mirror states of interest in ^{26}Mg have either not been able to accurately separate the states of interest [139, 140], or have extracted anomalously large spectroscopic factors [143], calling in to question understanding of the reaction mechanisms involved.

The objective of the current experiment was to extract estimates for the proton partial widths for states of ^{26}Si of astrophysical interest. This was achieved by fitting experimental angular distributions of the mirror states in ^{26}Mg, populated by the ^{25}Mg(d, p) reaction, to theoretical angular distributions, extracting neutron spectroscopic factors for each state. Under the assumption of isospin symmetry, as described in §2.3.1, the neutron spectroscopic factors of states in ^{26}Mg will be equal to the proton spectroscopic factors for the corresponding mirror states in ^{26}Si. Knowledge of the proton spectroscopic factor of each state allows an estimate to be made for the proton partial width of each state. The resonance strengths of the resonances the ^{25}Al$(p, \gamma)^{26}$Si reaction proceeds through at nova temperatures are strongly dependent on the proton partial widths of these resonance states. Constraining these proton partial widths will reduce uncertainty in the contribution of each resonance to the ^{25}Al$(p, \gamma)^{26}$Si reaction rate and thus the amount of ^{26}Al expected to be produced in classical novae.
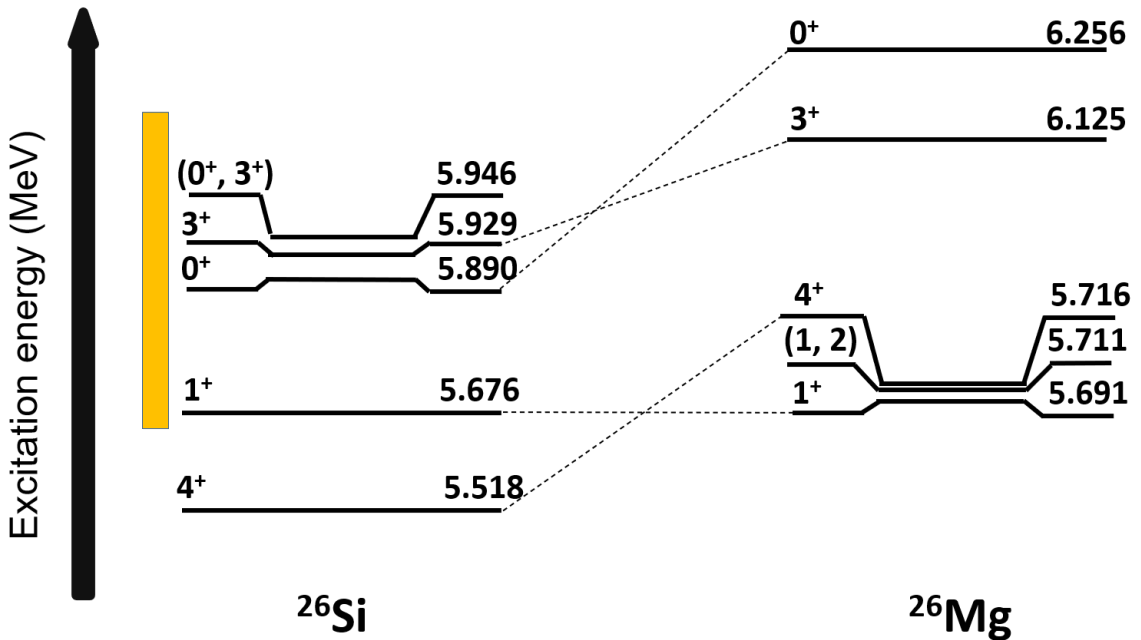
Figure 4.1 *Excited states of ^{26}Si above the proton threshold, matched with the most likely mirror states in ^{26}Mg. Excitation energies are in MeV, taken from Ref. [81], with the Gamow window for the $^{25}Al(p,\gamma)^{26}Si$ reaction at nova temperatures marked in orange.*

4.2 Identification of excited states of ^{26}Mg populated using the ^{25}Mg(d, p)^{26}Mg reaction at a beam energy of 8 MeV

The current experiment investigated states of ^{26}Mg at excitation energies around 5.5–6.3 MeV, the region containing states that are mirror states to those of astrophysical interest in the $^{25}Al(p,\gamma)^{26}$Si in novae. Proton spectra were measured at multiple lab angles in the range 13-55°. The states of astrophysical interest can be seen in Figures 4.2 and 4.3, at lab angles of 30 and 13° respectively. This section shall focus on those states of astrophysical interest to the $^{25}Al(p,\gamma)^{26}$Si reaction rate.

The channel numbers and excitation energies of well-known, strongly populated states of ^{26}Mg were fitted with a second order polynomial fit, allowing the clear, unambiguous identification of the states of astrophysical interest at 5.691, 6.125 and 6.256 MeV, with all other states observed agreeing within 5 keV of literature energy levels [81].

The 3$^+$ state was clearly observed across all angles as a very strong peak, as
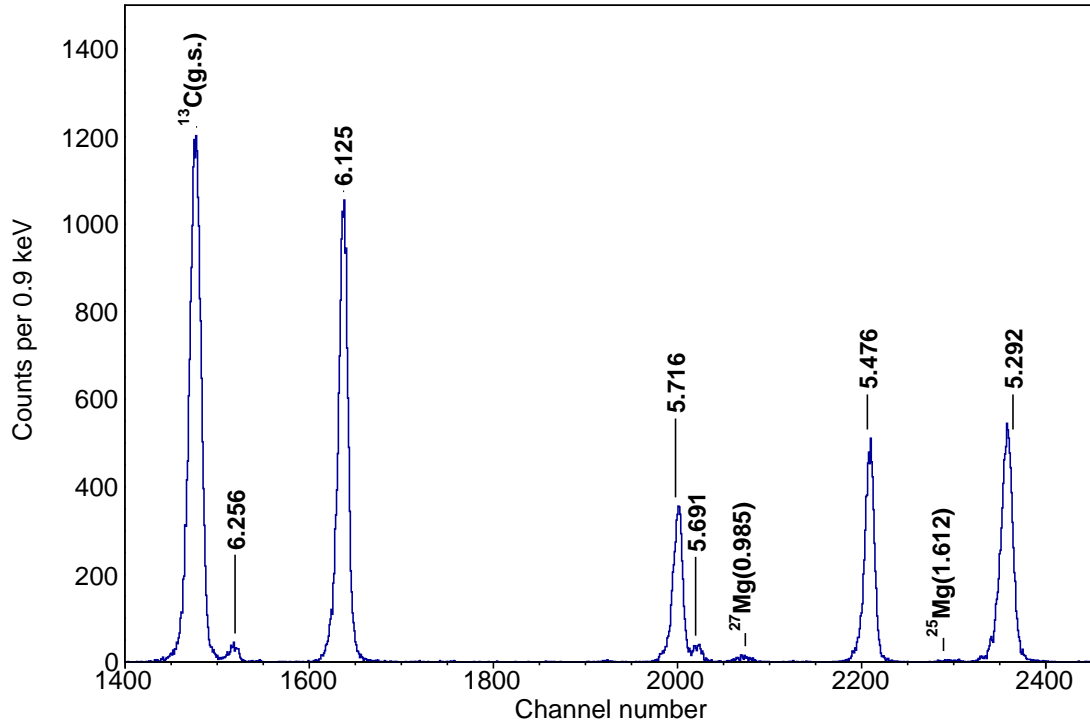
Figure 4.2 *Energy spectrum of protons from the $^{25}Mg(d,p)^{26}Mg$ reaction, zoomed in on the states of interest in this study, measured at $\theta{=}30°$. Peaks corresponding to the excited states of ^{26}Mg are labelled with their excitation energy in MeV, taken from Ref. [81]. The final excited states of contaminant peaks are also labelled.*

expected from previous studies, consistent with its large spectroscopic factor. The 0^+ state was observed separated from other peaks at multiple angles, the first time for a $^{25}\mathrm{Mg}(d,p)^{26}\mathrm{Mg}$ study. At lab angles $19°$ and less (as shown in Figure 4.3), protons from the state appeared at a lower rigidity than those corresponding to the $^{12}\mathrm{C}(d,p)^{13}\mathrm{C}$(g.s.) reaction, and at $27°$ and greater, they appeared at a higher rigidity than the contaminant protons (as shown in Figure 4.2). Between these two regions, the 0^+ peak was obscured by the carbon peak and thus no reliable cross sections could be measured.
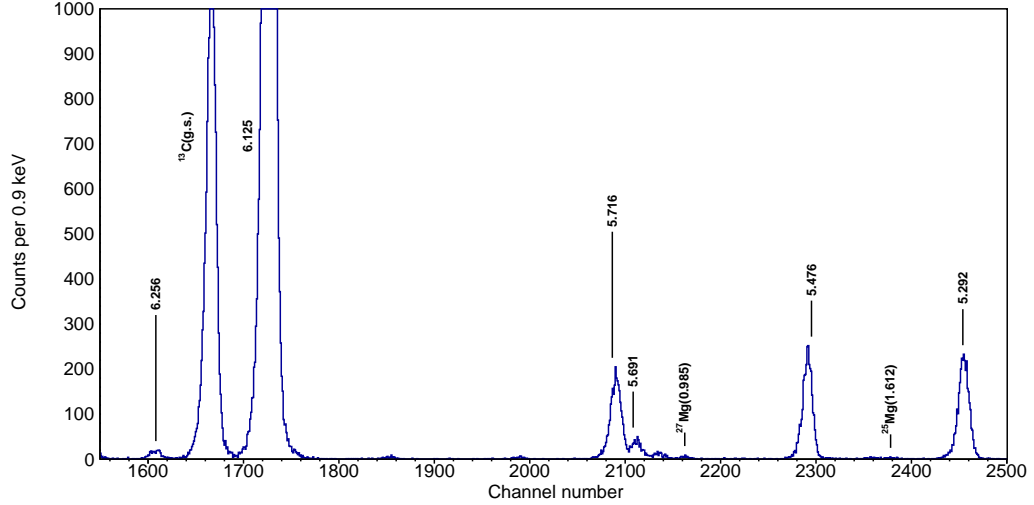
Figure 4.3 *Energy spectrum of protons from the $^{25}Mg(d,p)^{26}Mg$ reaction, zoomed in on the states of interest in this study, measured at $\theta=13°$. Peaks corresponding to the excited states of ^{26}Mg are labelled with their excitation energy in MeV, taken from Ref. [81]. The final excited states of contaminant peaks are also labelled.*

The 1^+ 5.691 MeV state was observed alongside the neighbouring peak at 5.71 MeV, while previous (d,p) studies were not able to distinguish the two peaks. They were fitted well by a double Gaussian fit across all angles, as shown in Figure 4.4. For clearly isolated peaks, the proton yield for each peak was found by summing bin counts around that peak. Unresolved doublets (for example the two peaks around 5.7 MeV and the 6.256 MeV state at angles where it merged with the carbon peak) were fitted with a combination of two Gaussian functions where the widths were fixed. Differential cross section angular distributions were fitted with a combination of DWBA calculations of the direct reaction mechanism for allowed angular momentum transfers and the compound nucleus mechanism, with the magnitudes of both contributions allowed to vary freely.
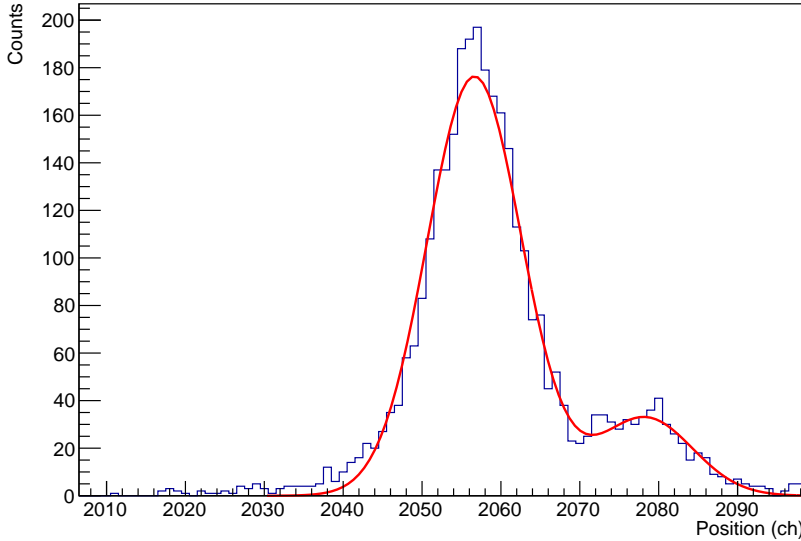
Figure 4.4 *States around an excitation energy of 5.7 MeV, populated with the $^{25}Mg(d,p)^{26}Mg$ reaction, at a lab angle of 22°, fitted with a double Gaussian fit (red).*

4.3 Angular distributions of states populated in the ^{25}Mg(d, p)^{26}Mg reaction relevant to the ^{25}Al(p, γ)^{26}Si reaction in novae

This subsection presents the angular distributions of excited states of ^{26}Mg measured in this study and their fits to theoretical calculations, which were used to extract spectroscopic factors for states of astrophysical interest in the current work. The protons detected can be easily assumed to have a Poisson distribution, giving a relative statistical uncertainty of $1/\sqrt{N}$, where N is the number of counts in the peak. The angular distributions presented in this thesis show simply the statistical uncertainties in the differential cross sections, unless otherwise stated. Experimental cross sections of excited states observed in this first experiment were fitted to DWBA and HF theoretical angular distributions, as described in §2.3 and §2.3.2 respectively. To fit the two components of the angular distribution to the experimental data, the direct and compound components are added together, with their magnitudes allowed to vary freely, until a minimum in the chi-squared value of the fit was found.
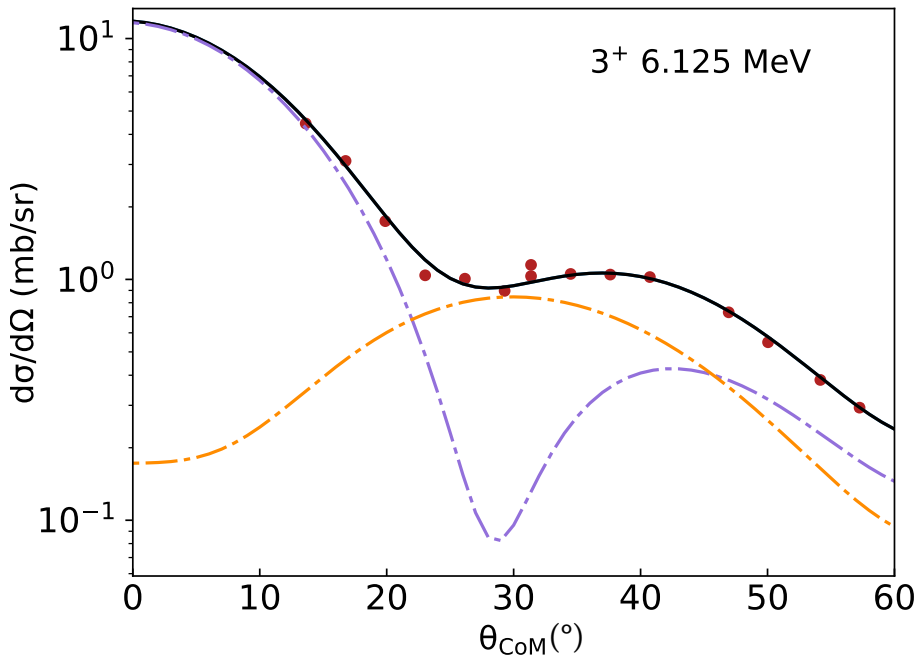
Figure 4.5 *Differential cross section measurements for the state at 6.125 MeV state, populated using the $^{25}Mg(d,p)^{26}Mg$ reaction at a beam energy of 8 MeV. This state is fitted by a linear combination of the $\ell=0$ (purple) and $\ell=2$ (orange) direct reaction components. Error bars showing statistical uncertainties are included, but are too small to see on the scale [1].*

3^+ state at 6.125 MeV

As can be seen in Figure 4.5, the angular distribution of the 3^+ state measured in the current work has a distinctive sharp decline in differential cross section at forward angles, before flattening, and then declining sharply again at more backwards angles. This distribution is fitted well by the $\ell=0 + 2$ combination of ℓ-transfers, and its shape is very similar to that seen in previous (d,p) studies [139, 140], despite the difference in beam energies.

This contrasts with the angular distribution of the 2^+ state at 5.292 MeV, which is fitted well by a pure $\ell=2$ transfer, as shown in Figure 4.6. This is consistent with previous measurements, which also found this state much more strongly populated by an $\ell=2$ transfer [139, 140], despite angular-momentum conservation rules allowing an $\ell=0$ transfer.

The extracted $C^2S(\ell=0)$ value of the 3^+ state agrees very well with the previous studies of Burlein *et al.* [139] and Arciszewski *et al.* [140], as shown in Table 4.1. However, the extracted $C^2S(\ell=2)$ value is slightly larger than that of Burlein *et al.* [139], and about half the size of that reported by Arciszewski *et al.* [140]. It is

interesting that although these two previous studies had very similar experimental set ups, including beam energies (12 and 13 MeV respectively), they extract different $\ell=2$ values for the 3^+ state. The $(^4\text{He}, ^3\text{He})$ study of Yasue *et al.* [143] and the shell-model calculations of Richter *et al.* [86] reported $\ell=0$ and $\ell=2$ values that match well with the values we have extracted for this state.
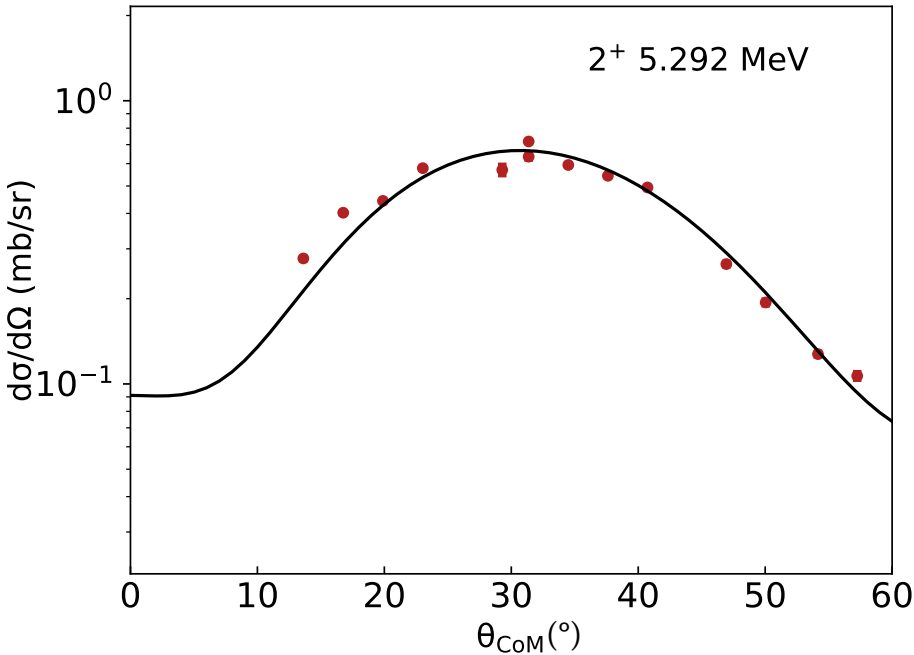
Figure 4.6 *Differential cross section measurements for the state at 5.292 MeV, populated using the $^{25}Mg(d,p)^{26}Mg$ reaction at a beam energy of 8 MeV. This state is well fitted with just an $\ell = 2$ component (black line). Error bars showing statistical uncertainties are included, but are too small to see on the scale [1].*

0^+ state at 6.256 MeV

In Figure 4.7, the angular distribution of the 0^+ state shows a single peak around $30°$, indicative of an $\ell=2$ transfer. However, the peak is flatter than the DWBA calculation predicts. A linear combination of the direct and compound components fits the experimental data points well, as shown in Figure 4.8, allowing the extraction of a value for the spectroscopic factor.

The $C^2S(\ell=2)$ value of 0.042(10) extracted matches well with that measured in the $(^4\text{He}, ^3\text{He})$ study of Yasue *et al.* [143] and shell-model calculations [86], as shown in Table 4.1 and stands as the first (d,p) study to extract a spectroscopic factor for this state.
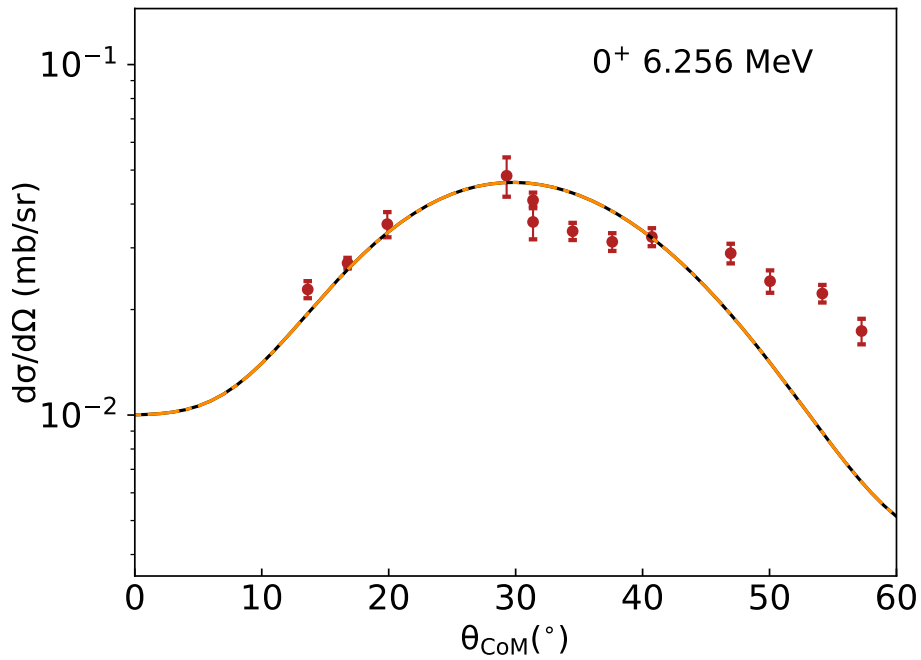
Figure 4.7 *Differential cross section measurements for the state at 6.256 MeV, populated using the $^{25}Mg(d,p)^{26}Mg$ reaction at a beam energy of 8 MeV. The peak of the angular distribution is flatter than the DWBA calculations alone (orange and black) suggest.*
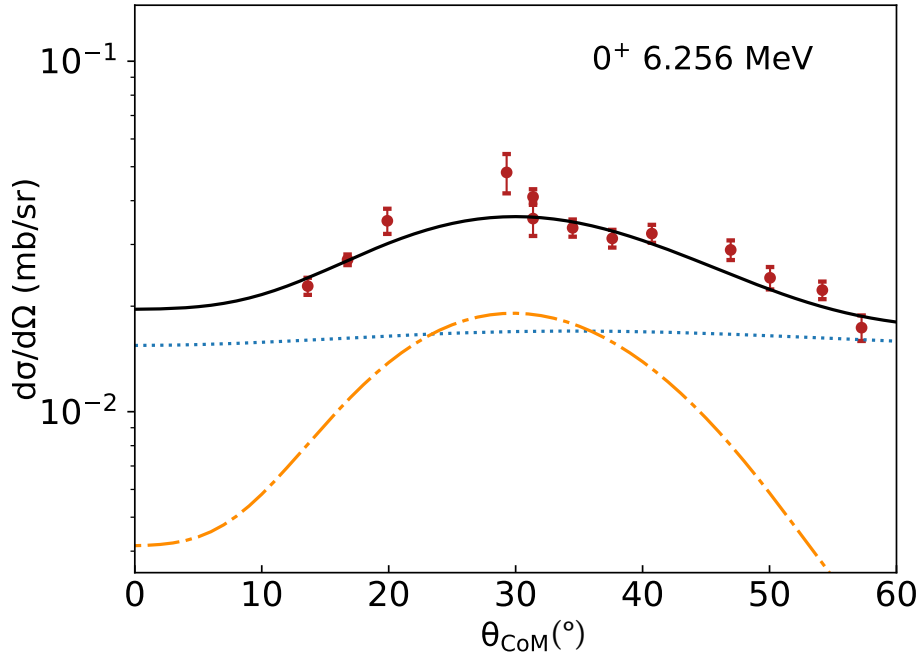
Figure 4.8 *Differential cross section measurements for the state at 6.256 MeV, populated using the $^{25}Mg(d,p)^{26}Mg$ reaction at a beam energy of 8 MeV. This angular distribution is fitted well by a combination of the direct $\ell=2$ component (orange) and the compound nuclear component (dashed blue) [1].*

1^+ state at 5.691 MeV
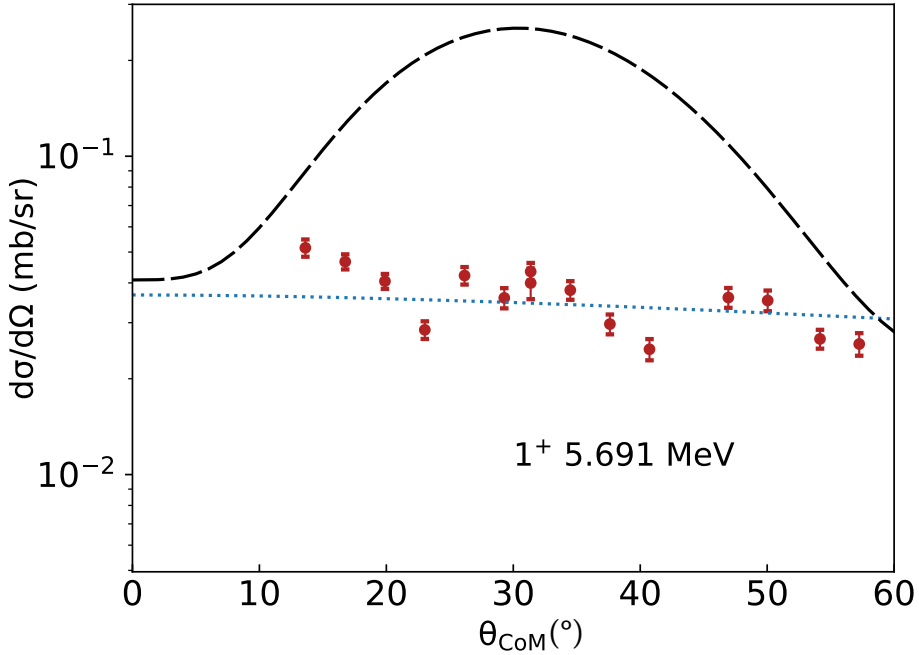
Figure 4.9 *Differential cross section measurements for the state at 6.256 MeV, populated using the $^{25}Mg(d,p)^{26}Mg$ reaction at a beam energy of 8 MeV. This state is best fitted solely by the compound mechanism (dotted blue), while the direct component implied by the $(^4He, ^3He)$ measurement of Yasue et al. [143] is shown in dashed black [1].*

A measurement by Yasue *et al.* of the neutron spectroscopic factor of the 1^+ state, using a ^{25}Mg(^{4}He, ^{3}He)^{26}Mg reaction, extracted a spectroscopic factor of C^2S=0.2 [143]. This is roughly 50 times larger than the spectroscopic factors predicted by shell-model calculations, including C^2S=0.0035 [86], C^2S=0.0040 [144] and C^2S=0.0048 [87]. As stated in the paper describing the ^{25}Mg(^{4}He, ^{3}He)^{26}Mg reaction, the measured spectroscopic factor may have been enhanced by the contribution from multistep reaction processes to the 1^+ state, or possibly from difficulty in resolving the 1^+ state from the neighbouring 4^+ state. Previous (d, p) studies failed to resolve the two peaks [139, 140].

The differential cross section angular distribution that can be seen in Figure 4.9 appears to have a flat shape, with no features that are indicative of a direct reaction mechanism. The data are best fitted by the compound reaction mechanism alone, with no contribution from a direct reaction mechanism. By keeping the magnitude of the compound component constant and varying the direct reaction mechanism component, an upper limit on the direct reaction mechanism at the 1σ level was found, allowing a calculation of an upper limit on

72

the spectroscopic factor.

As shown in Table 4.1, this upper limit of $C^2S < 5.7 \times 10^{-3}$ is consistent with the shell-model calculation of 3.5×10^{-3} [86], but is roughly 40 times smaller than the spectroscopic factor extracted from the $(^4\text{He}, ^3\text{He})$ study of Yasue *et al.* [143]. As discussed here and in the publication of Yasue *et al.* itself, this discrepancy is likely due to an increased yield from multistep processes through lower energy 2^+ states in ^{26}Mg. Thus, the work described in this thesis stands as the first experiment to constrain the spectroscopic factor of the 1^+ state through a reliable, well-understood reaction mechanism.

Summary of spectroscopic factors of astrophysically relevant states

Table 4.1 presents the spectroscopic factors for states of ^{26}Mg of astrophysical interest measured in the current experiment. Comparisons are made to the previous (d, p) studies of Burlein *et al.* [139] and Arciszewski *et al.* [140], the $(^4\text{He}, ^3\text{He})$ study of Yasue *et al.* [143] and the shell-model calculations performed with the USDB Hamiltonian by Richter *et al.* [86].

From a consideration of different sources of potential parameters, including Refs. [105, 106], the uncertainty in the extracted spectroscopic factor from the choice in potential parameters was found to be $\sim$20%, similar to other analyses with DWBA calculations. The calculation of uncertainties for the spectroscopic factors in this experiment was done by adding the uncertainty in the fit (which was dependent on the statistical uncertainties associated with every cross section), the target thickness uncertainty, and the DWBA potential parameters in quadrature.

Table 4.1   *Neutron spectroscopic factors from previous neutron transfer studies and the current work, for states in ^{26}Mg with mirror states of relevance to the ^{25}Al$(p, \gamma)^{26}$Si reaction in novae. Spectroscopic factors for the mirror states in ^{26}Si, from sd-shell model calculations, are also shown for comparison.*

E_x [MeV] [81]	J^π	ℓ	C^2S_{exp}				C^2S_{th}
			(d,p) [139]	(d,p) [140]	$(^4\text{He}, ^3\text{He})$ [143]	Current Work	sd-shell [86]
5.69108(19)	1^+	2			0.20(4)	$<5.7 \times 10^{-3}$ [a]	3.5×10^{-3}
6.12547(5)	3^+	0, 2	0.121, 0.206 [b]	0.106(13), 0.60(14)	0.14(3), 0.30(6)	0.11(2), 0.27(6)	0.14, 0.33
6.25547(5)	0^+	2			0.054(11)	0.042(10)	0.039

[a] Upper limit at 1σ confidence level.
[b] No uncertainties were provided in this reference.

Peak at 5.71 MeV

In addition to the previously mentioned 1^+ state at 5.69 MeV, the $(^4\text{He}, ^3\text{He})$ study of Yasue *et al.* [143] identified a neighbouring peak at 5.71 MeV. The angular distribution of this peak was fitted solely with an $\ell=2$ transfer, with a spectroscopic factor of $C^2S=0.030$ extracted. This is consistent with a known 4^+ state at 5.716 MeV in ^{26}Mg populating the peak. The corresponding 4^+ mirror state in ^{26}Si has an excitation energy of 5.518 MeV, below the Gamow window of the $^{25}\text{Al}(p, \gamma)$ reaction at nova temperatures, meaning it is not astrophysically important. A peak at 5.71 MeV was also identified in the current work, with a differential cross section angular distribution that is described well by a combination of an $\ell=2$ transfer and a compound contribution, as can be seen in Figure 4.10. This is also consistent with a 4^+ state populating the peak and resulted in a spectroscopic factor of $C^2S(\ell=2)=0.030(7)$ being extracted.
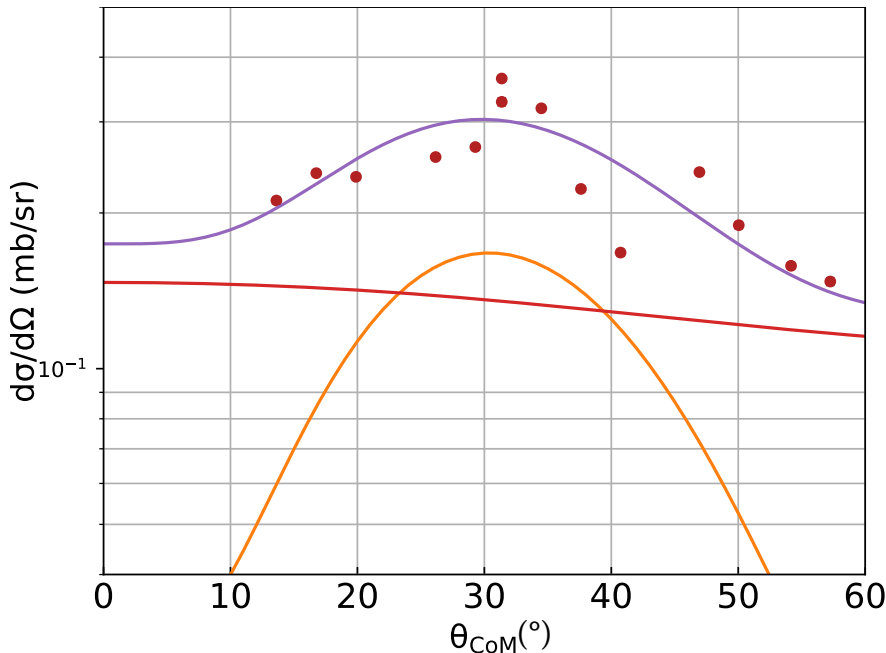
Figure 4.10 *Angular distribution of the peak at 5.71 MeV, fitted by the $\ell=2$ direct reaction mechanism (orange) and compound reaction mechanism (red). Error bars showing statistical uncertainties are included, but are too small to see on the scale.*

However, the study of Bhattacharjee *et al.* [142], in addition to the previously discussed 1^+ state at 5.691 MeV [145, 146] and the 4^+ state at 5.716 MeV [147, 148], observed γ rays associated with a state at 5.711 MeV decaying to a 0^+
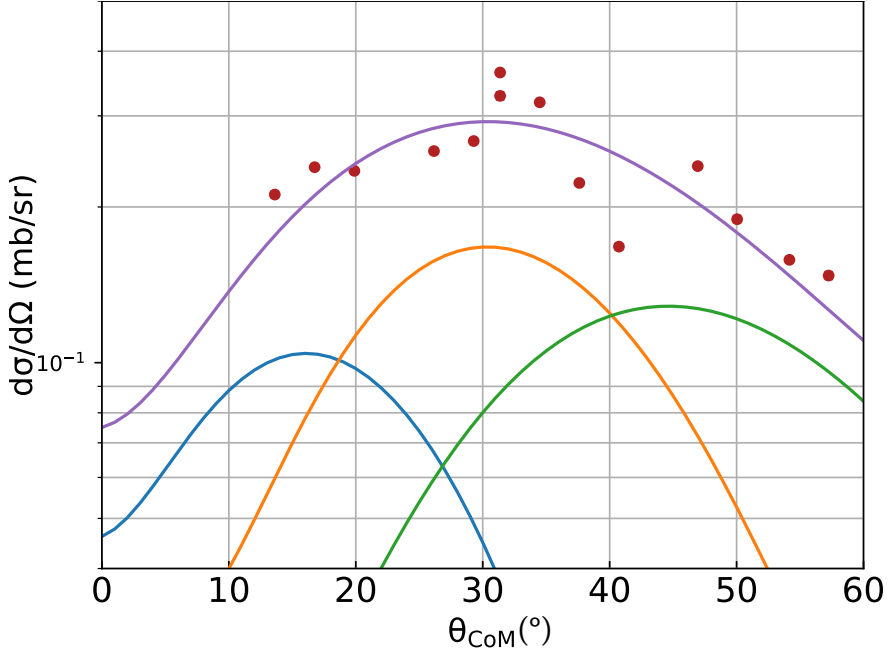
Figure 4.11 *Angular distribution of the peak at 5.71 MeV, fitted by direct mechanisms. The blue, orange and green angular distributions represent the $\ell=1$, 2 and 3 ℓ-transfers respectively. Error bars showing statistical uncertainties are included, but are too small to see on the scale.*

state. As only E1, E2 and M1 transitions would be strong enough to have been observed, the possible spin/parities of the 5.711 MeV state must be restricted to 1^+, 2^+ or 1^-. The (d, p) studies of Arciszewski *et al.* [140] and Burlein *et al.* [139] did not resolve the peaks at 5.69 and 5.71 MeV that were observed in the current work, observing only a single peak. In addition to an $\ell=2$ transfer, both (d, p) studies found evidence for an $\ell=3$ transfer, implying the existence of a negative parity state in this region. Combining the results of these studies implies the existence of a 1^- state at 5.711 MeV in ^{26}Mg.

The prospect of such a negative parity peak being present in this region was investigated in the current work by considering the peak at 5.71 MeV to contain contributions from a positive parity (4^+) state at 5.716 MeV and a negative parity state at 5.711 MeV. The angular distribution of the peak was fitted well by a combination of $\ell=1$, 2 and 3 ℓ-transfers, as can be seen in Figure 4.11. As parity is conserved by the strong force, which facilitates nuclear reactions, negative parity states are exclusively populated by odd ℓ-transfers in the ^{25}Mg$(d, p)^{26}$Mg reaction studied in this work. Thus, the angular distribution observed for this excited state is consistent with the existence of a negative parity state in this region. Assuming no compound mechanism contribution and

positive and negative parity states in the 5.71 MeV peak, spectroscopic factors of $C^2S(\ell=1)=0.009(2)$ and $C^2S(\ell=3)=0.25(6)$ (with the $C^2S(\ell=2)$ value unchanged at 0.030(7)) were extracted.

While no spectroscopic factors of odd ℓ-transfers are provided in the previous (d,p) studies [139, 140] to directly compare to, the fits of the angular distributions imply a large $\ell=3$ spectroscopic factor, consistent with that extracted in the current work. However, both studies did not include any $\ell=1$ component in the fitting of their angular distributions, while the current work has one that contributes noticeably to the shape of the angular distribution. The extracted $\ell=2$ spectroscopic factor for the 4^+ state of $C^2S=0.030(7)$ agrees well with that from the study of Yasue *et al.* [143] ($C^2S=0.030$) and shell-model calculations [86] ($C^2S=0.036$). However, it is smaller than those reported by Arciszewski *et al.* [140] ($C^2S=0.139$) and Burlein *et al.* [139] ($C^2S=0.062$). The tables of results in both (d,p) studies seem to imply, for the extraction of spectroscopic factors, the peak was only fitted using an $\ell=2$ transfer, resulting in a larger spectroscopic factor than would have been extracted given the inclusion of other ℓ-transfers.

To summarise, the investigation performed in the current work cannot conclude on the existence of a negative parity state at 5.71 MeV in ^{26}Mg, but the results are broadly consistent with such a state. As no definite mirror state in ^{26}Si has been identified for the state at 5.711 MeV in ^{26}Mg, it was not included in the ^{25}Al$(p,\gamma)^{26}$Si reaction rate calculations performed in the next section.

4.4 Calculation of the ^{25}Al(p, γ)^{26}Si reaction rate at nova temperatures

4.4.1 Previous work constraining resonance properties of resonance states in ^{26}Si relevant to the ^{25}Al(p, γ)^{26}Si reaction

As mentioned previously, four states in ^{26}Si have been observed in the excitation energy range that corresponds to nova burning temperatures for the ^{25}Al$(p,\gamma)^{26}$Si reaction. These are at excitation energies of 5.676 (1^+), 5.890 (0^+), 5.929 (3^+) and 5.946 MeV (spin/parity uncertain). Only the 3^+ state at 5.929 MeV has had its partial widths constrained in ^{26}Si so far, while estimations of the strengths of

1^+ and 0^+ resonances have relied on shell-model calculations and mirror nuclei studies to constrain their resonance parameters. A summary of knowledge of the states in the Gamow window at nova temperatures is presented below.

The state at 5.676 MeV has had its spin/parity firmly established as 1^+ by the γ-ray study of Seweryniak et $al.$ [149]. Shell-model calculations indicate that the proton partial width is much smaller than the Gamow partial width, meaning the resonance strength is very dependent on the proton partial width of the state.

The state at 5.890 MeV has been firmly established as having a spin/parity of 0^+. This state was observed by de Séréville et $al.$ [150] through the detection of neutrons and γ rays from the ^{24}Mg(^{3}He,$n\gamma$) reaction. The ^{24}Mg(^{3}He,$n\gamma$) studies of Komatsubara et $al.$ [151] and Doherty et $al.$ [152] measured the angular distributions of γ-γ angular correlations, providing a firm assignment to the state of J^π=0^+.

The state in ^{26}Si at 5.929 MeV has had its spin/parity well established to be 3^+, through studies of the ^{28}Si(p,t)^{26}Si reaction [153, 154] and the β-decay of ^{26}P to this state [155, 156].
A measurement of the proton decay in the ^{25}Al(d,n)^{26}Si*(p) reaction allowed the proton partial width of this state to be estimated to be Γ_p=2.9(1.0) eV [157]. However, this study does not give a value for the measured spectroscopic factor of the state, merely describing it as a 'large spectroscopic factor'. The low counts from the experiment, the inability to separate the contributions from the 3^+ and 0^+ resonances and the possibility of an ℓ=2 contribution from the state all contribute to the uncertainty of this result. This measurement of the proton partial width was combined with the intensity of the proton decay from Ref. [155] and measurement of the γ-decay intensity of the state to achieve Γ_γ=4.0 $\pm$ 1.1(stat.)$^{+1.9}_{-1.8}$(lit.) $\times$ 10^{-2} eV by Bennett et $al.$ [156], using the relation I_p/I_γ=Γ_p/Γ_γ. A recent coincidence measurement of the proton and γ-decay of the state by Liang et $al.$ [158] using the same relation gave a concordant γ partial width of $6.04^{+3.00}_{-2.76} \times 10^{-2}$ eV.

Initially the level at 5.946 MeV was assigned spin/parity 0^+ by Parpottas et $al.$ (2004) [159], using the ^{24}Mg(^{3}He,n)^{26}Si reaction. However, this assignment was

based on comparisons to HF calculations, which are only considered reliable at excitation energies of sufficiently high energy level densities and with a purely compound reaction mechanism. As studies at similar beam energies and excitation energies [160–162] show significant direct components, the appropriateness of HF calculations in the study of Parpottas *et al.* seems doubtful, casting significant uncertainty on this spin/parity assignment. Furthermore, a (^{3}He, ^{6}He) study by Caggiano *et al.* (2002) [163] saw an energy level at 5.945(8) MeV, but stated that it could not be a 0^+ state, due to other 0^+ states having a weaker population, assigning a spin/parity of 3^+ to this state. However this was prior to the state at 5.929 MeV being firmly assigned $J^\pi=3^+$ [153–156, 158]. As shell-model calculations do not predict more than one 0^+ or 3^+ state around this excitation energy, and no unmatched 0^+ or 3^+ mirror candidates in ^{26}Mg exist in this region, neither a 0^+ nor a 3^+ assignment can be considered satisfying for the state at 5.946 MeV.

The existence of a negative parity state at 5.711 MeV in ^{26}Mg, as discussed in the previous section, would imply the existence of a matching negative parity state in ^{26}Si, but no state currently appears to be a definite candidate for this assignment. The NNDC compilation does not describe any negative parity states around an excitation energy of $\sim$5–6 MeV in ^{26}Si, with the lowest lying negative parity state described in the compilation a 3^- state at 6.787(4) MeV, matched well to the 3^- state in ^{26}Mg at 6.876 MeV [81]. The state in ^{26}Si at 5.946 MeV (which has had previously conflicting spin/parity assignments), a state observed at 6.101 MeV with no current spin/parity assignment, or a negative parity state in ^{26}Si that has yet to be observed could all possibly be the mirror state of the state at 5.711 MeV in ^{26}Mg. If this mirror state lies within the Gamow window of the ^{25}Al$(p,\gamma)^{26}$Si reaction at nova temperatures (as a state at 5.946 MeV would), it could have a significant effect on the reaction rate through an $\ell=1$ resonance. Due to the uncertain nature of this state's properties, it has not been included in the reaction rate calculations presented here.

78

4.4.2 Extraction of proton partial widths for states of ^{26}Si of astrophysical interest from the current work

Under the assumption of isospin symmetry, as described in §2.3.1, the structure of the mirror nucleus is able to provide nuclear structure information, with the spectroscopic factor of a mirror state allowing the size of the partial width in an unstable nucleus to be estimated.

In Ref. [86], shell-model calculations using the USDB Hamiltonian are used to calculate C^2S and Γ_p values for states in ^{26}Si. The proton partial width of a state, calculated as $\Gamma_p = C^2S\Gamma_{sp}$, scales linearly with both Γ_{sp} (the single-particle width of that state) and the spectroscopic factor of that state. Refs. [92] and [164] compare neutron and proton spectroscopic factors for pairs of light mirror nuclei and find a maximum deviation of ∼25%, with the differences for most pairs ≤15%, indicating the typical uncertainties expected for the spectroscopic factors of mirror nuclear states.

In the current work, under the assumption of isospin symmetry, experimental proton partial widths were extracted by multiplying the theoretical partial widths by the ratio of the experimental ^{26}Mg neutron spectroscopic factor and the theoretical ^{26}Si proton spectroscopic factor for each state. This allowed proton widths for the 3^+ and 0^+ mirror states in ^{26}Si to be calculated and an upper limit to be extracted for the 1^+ state, shown in Table 4.2.

For the astrophysically relevant 0^+ state in ^{26}Si, Ref. [86] took the state to be at 5.946 MeV, however, all recent studies have shown the 0^+ state to be at 5.890 MeV [150–152, 165]. The single-particle width is calculated as $\Gamma_{sp} = 2\gamma^2 P(\ell, R_c)$, where $P(\ell, R_c)$ is the penetrability factor for that state. Using the CRIB Penetrability/Wigner limit calculator [166], written by Dr. YAMAGUCHI Hidetoshi, using theory described in Ref. [167], the ratio of $P(\ell, R_c)$ between 5.890 and 5.946 MeV was found to be 0.2409(16) (with the uncertainty originating in the difference in the choice of nuclear radius). The single particle width of the 0^+ state of interest from Ref. [86] was scaled by this value in the calculation of the proton partial width for this state.

The proton partial width of Γ_p∼2.6 eV calculated for the 3^+ state is in agreement with the value of 2.9(10) eV measured by Peplowski *et al.* [157] through the ^{25}Al$(d, n)^{26}$Si*(p) reaction, as shown in Table 4.2. The measurement of similar proton partial widths for mirror states is significant and gives substantial validity

Table 4.2 *Proton partial widths extracted for states contributing to the $^{25}Al(p,\gamma)^{26}Si$ reaction using the $^{25}Mg(d,p)^{26}Mg$ reaction compared to previous literature measurements.*

			Γ_p [eV]		
$E_x(^{26}Si)$ [MeV] [81]	E_r [MeV] [81]	J^π	Current work	Literature	sd-shell calculations [86]
5.6762(3)	0.1622(3)	1^+	$<1.0 \times 10^{-8}$	–	6.3×10^{-9}
5.8901(3)	0.3761(3)	0^+	4.2×10^{-3}	–	3.9×10^{-3}
5.9294(8)	0.4154(8)	3^+	2.6	2.9(1.0) [a]	3.5

[a] [157].

to the method employed in this work and the assumption of isospin symmetry. A proton partial width of 4.2×10^{-3} eV for the 0^+ resonance in ^{26}Si was calculated, consistent with the proton partial width implied by the shell-model calculations of Ref. [86] (once the change in the penetrability factor due to the new excitation energy has been taken in to account). This is roughly half of the shell-model calculation of the γ partial width, 8.8×10^{-3} eV [86], indicating that the resonance strength is mainly dependent on Γ_p. Between the confirmation of the excitation energy of the 0^+ state by multiple studies and the measurement of the proton partial width by this study, the uncertainty in the contribution of this resonance to the ^{25}Al(p,γ) reaction has been reduced significantly.

An upper limit of the proton partial width for the 1^+ state was determined to be $<1.0 \times 10^{-8}$ eV, much smaller than the γ partial width from shell-model calculations of 0.12 eV. This indicates that this resonance strength is almost completely determined by Γ_p, and therefore this study goes a significant way in reducing the uncertainty in the contribution of the 1^+ resonance to the ^{25}Al$(p,\gamma)^{26}$Si reaction rate.

4.4.3 ^{25}Al(p, γ)^{26}Si Reaction Rate Calculations

To calculate rates for the ^{25}Al$(p,\gamma)^{26}$Si reaction at nova temperatures, contributions from both the resonant and non-resonant components were calculated, using the formalisations set out in §2.2.

For the non-resonant capture component, a total S-factor of 28 keV-b was used, taken from Ref. [87], where S-factor values for individual states were calculated using the USDA interaction. Parameters used to calculate the resonance components of the reaction rate are given in Table 4.3. As the proton

and γ partial widths of the 3^+ state have been measured directly in the ^{26}Si nucleus, in Refs. [157] and [156], they were chosen to be used in the calculations (Ref. [156] has a smaller uncertainty than that quoted in Ref. [158]). shell-model calculations of the γ partial widths for the 0^+ and 1^+ states from Ref. [86] were used, as no measurement (direct or indirect) has been possible so far. No direct measurements for the proton partial widths of the 0^+ and 1^+ resonance exist, and as this work provides the first reliable experimental value for the 0^+ state and first reliable upper limit for the 1^+ state, they were used in the reaction rate calculations.

Figures 4.12 and 4.13 show the calculated reaction rate across relevant nova temperatures, first as an absolute reaction rate, then with each resonance component normalised to the total reaction rate.

Table 4.3 *Parameters of resonances in the $^{25}Al(p,\gamma)^{26}Si$ reaction used to calculate the reaction rate shown in Figure 4.12. A proton separation energy of S_p=5.51401(11) MeV [63] has been used to calculate the resonance energies.*

E_{x} [MeV] [81]	E_{r} [MeV][81]	J^π	Γ_p [eV]	Γ_γ [eV]	$\omega\gamma$ [eV]
5.6762(3)	0.1622(3)	1^+	$<1.0 \times 10^{-8}$	0.12 [a]	$<2.56 \times 10^{-9}$
5.8901(3)	0.3761(3)	0^+	4.2×10^{-3}	8.8×10^{-3} [a]	2.35×10^{-4}
5.9294(8)	0.4154(8)	3^+	2.9 [b]	0.040 [c]	2.30×10^{-2}

[a] [86].
[b] [157].
[c] [156].
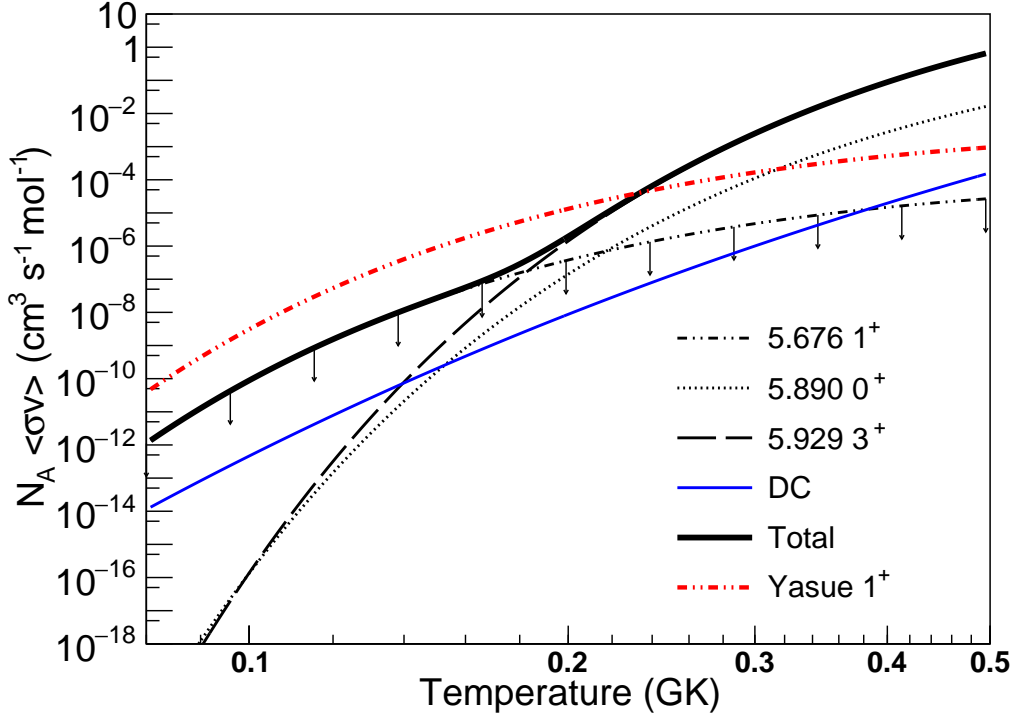
Figure 4.12 *$^{25}Al(p,\gamma)^{26}Si$ rate calculated using the parameters in Table 4.3. The downward-pointing arrows indicate an upper limit from the 1^+ contribution. The dashed red line indicates the contribution that would be implied by the spectroscopic factor measured in the $(^4He, ^3He)$ study by Yasue et al. [143].*

As can be seen, the contribution from the direct capture mechanism is orders of magnitude smaller than the total reaction rate across all temperatures, and thus can be considered negligible to the reaction rate. At lower temperatures, below $\sim$0.2 GK, the 1^+ resonance dominates the reaction rate. At temperatures above $\sim$0.2 GK, the ℓ=0 resonance capture on the 3^+ state dominates the reaction rate. The 0^+ resonance contributes $\lesssim$10% to the reaction rate at these higher temperatures.

An investigation in to the role of the 1^+ resonance in the ^{25}Al$(p,\gamma)^{26}$Si reaction by Parikh and José [61] showed that, even with the larger resonance strength implied by Yasue *et al.* [143], the ^{25}Al half-life by proton capture in nova environments (roughly 200 s) is still significantly longer than the β-decay half-life of ^{25}Al ($t_{1/2}$=7.2 s [168]). In addition, they showed that the difference in ^{26}Al yield from models, using the higher Yasue or lower shell-model spectroscopic factor, was less than 5%. The greatly reduced experimental spectroscopic factor reported in this work emphasises their conclusion that the 1^+ resonance has very little relevance
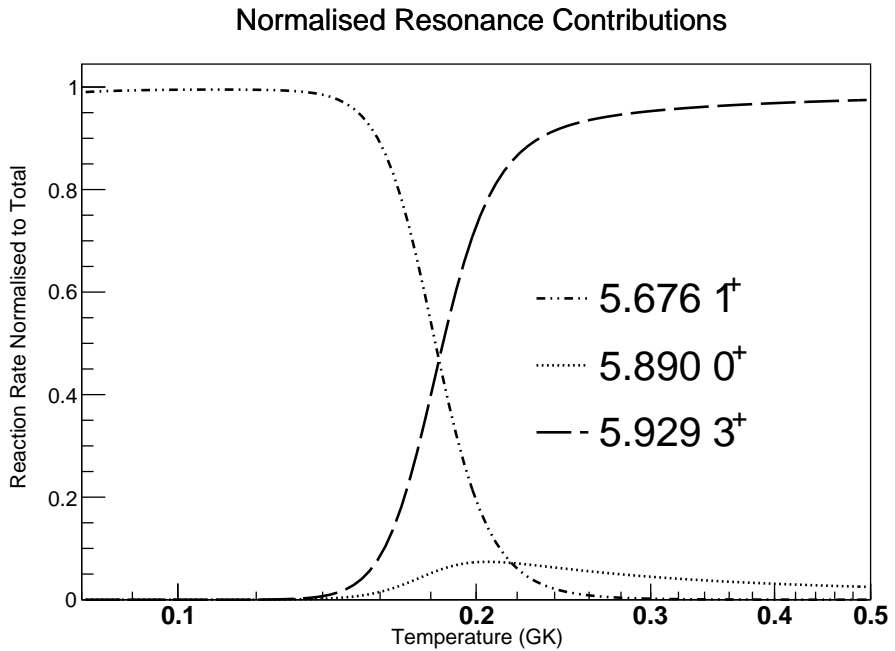
Figure 4.13 *Reaction rates of the three resonances in the $^{25}Al(p,\gamma)^{26}Si$ reaction, normalised to the total reaction rate, using the resonance parameters given in Table 4.3.*

for the determination of the amount of ^{26}Al produced in novae.

This work indicates that the 0^+ resonance has a small effect on the production of ^{26}Al in novae, and stands as the first study to extract a reliable pure spectroscopic factor from the state, thus extracting a proton partial width that can be used with confidence.

4.4.4   Comparison of the ^{25}Al(p, γ)^{26}Si reaction rate to previous work

Figure 4.14 compares the recommended ^{25}Al$(p,\gamma)^{26}$Si reaction rate calculated in the current work and the rate calculated in the Monte Carlo uncertainty analysis of Iliadis *et al.* [169]. It can be seen that the predicted reaction rate is less than that predicted in the study of Iliadis *et al.* [169], mainly due to the measurement of the 3^+ resonance proton partial width being smaller than the shell-model calculation of Iliadis *et al.* [169]. With the constraints placed on the 1^+ and 0^+ resonances in this study, and the reaffirmation of the size of the 3^+ proton partial width, this lower reaction rate has been established
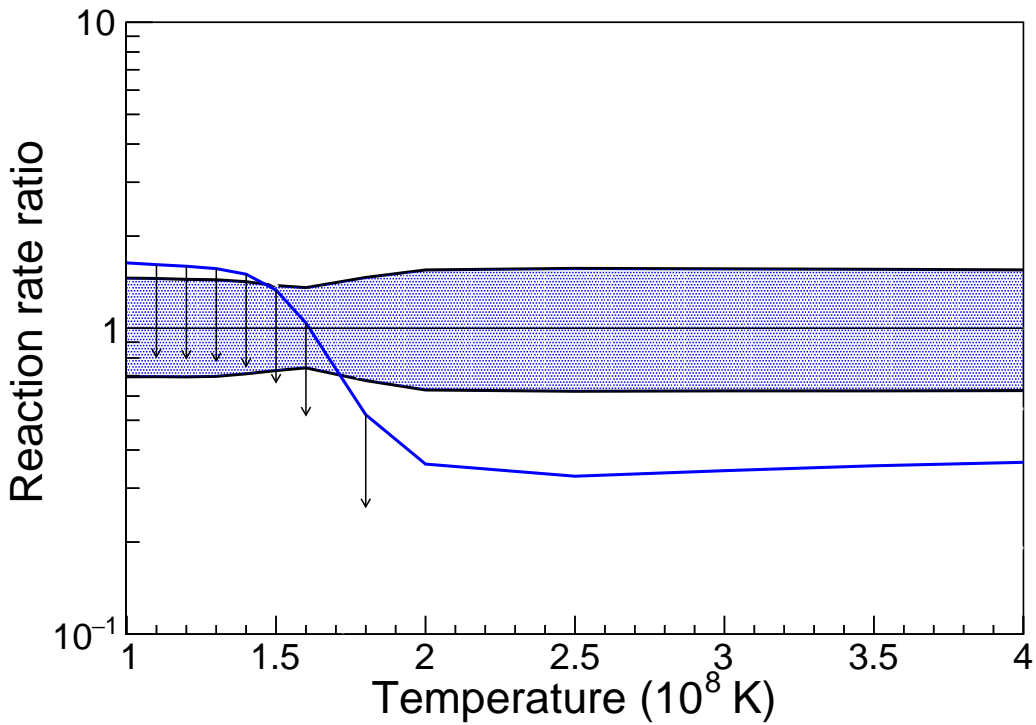
Figure 4.14 *Ratio of the current calculation of the $^{25}Al(p,\gamma)^{26}Si$ reaction rate (blue) to the Monte Carlo uncertainty study of Iliadis et al. [169]. The "low rate" and "high rate" from Iliadis et al. are indicated by the shaded areas. Arrows indicate the temperatures at which the reaction rate ratio should be considered an upper limit due to the 1^+ resonance dominating the reaction rate.*

with greater certainty. A lower ^{25}Al$(p,\gamma)^{26}$Si reaction rate implies less ^{25}Al will follow the ^{25}Al$(p,\gamma)^{26}$Si$(\beta^+\nu)^{26}$Al^m reaction pathway and will instead follow the ^{25}Al$(\beta^+\nu)^{25}$Mg$(p,\gamma)^{26}$Al^g pathway, leading to more ^{26}Al^g production and novae being a more significant source of ^{26}Al in our Galaxy.

Chapter 5

Study of states populated in the ^{25}Mg(d, p)^{26}Mg reaction relevant to ^{22}Ne + α reactions in the weak s-process

5.1 Astrophysical background and properties of interest in states of ^{26}Mg above the alpha threshold

The second experiment presented in this thesis measured the angular distributions of states in ^{26}Mg above the alpha threshold (S_α=10.6148 MeV) using the ^{25}Mg(d,p) reaction. In the weak s-process, the two reactions that determine the neutron budget are the ^{22}Ne(α,γ)^{26}Mg and ^{22}Ne(α,n)^{25}Mg reactions, which both proceed through natural-parity states of ^{26}Mg above the alpha and neutron (S_n=11.0931 MeV) thresholds respectively.

Direct measurements of these reactions are very experimentally challenging and have only allowed measurements of resonance strengths of states down to an excitation energy of 11.3195 MeV (E_r=704.7 keV) [170]. Therefore, measurements of the properties of these states of ^{26}Mg corresponding to lower-energy resonances through indirect reactions are required to constrain the strengths of resonances these reactions proceed through.

For states just above the alpha threshold, the alpha partial width is much smaller than the neutron or γ width, meaning the alpha partial width dominates the resonance strengths contributing to the ^{22}Ne$(\alpha, \gamma)^{26}$Mg and ^{22}Ne$(\alpha, n)^{25}$Mg reaction rates. Extraction of values for these alpha partial widths has been performed using alpha-transfer reactions, as shown in Refs. [171–173], which all used the ^{22}Ne$(^6$Li$, d)^{26}$Mg reaction to populate natural parity states of ^{26}Mg with large alpha widths. Recent alpha-transfer studies, measured at energies both above [174] and below [116] the Coulomb barrier threshold ($\sim$6 MeV), provided further values and upper limits for alpha partial widths across the ^{22}Ne $+ \alpha$ Gamow window at massive star temperatures. However, the extraction of accurate values of alpha partial widths from these experiments is dependent on knowledge of the spin/parity of the states observed.

Previous indirect studies that have also measured properties of these states have included: proton and deuteron scattering experiments to accurately measure excitation energies of states [175], a γ-decay heavy-ion experiment to constrain the properties of high-spin states [176], a photoexcitation experiment to unambiguously constrain the spin/parities and energies of states [177], alpha-scattering experiments to constrain the spin/parities of natural-parity low-spin states [173, 178], and neutron capture experiments that provided information on the energy, spin/parity, and n/γ partial widths of states above the neutron threshold through an R-matrix analysis [179, 180].

In the ^{25}Mg(d, p) reaction discussed in this chapter, the shapes of the angular distributions measured are sensitive to the orbital angular momentum transfers that populate the final states. As a state of a certain J^π can only be populated by certain ℓ-transfers, the shape of angular distributions can constrain the possible J^π values for a certain state. Thus, by fitting weakly-bound DWBA calculations, described in §2.3, to differential cross section angular distributions measured in the current work, the ℓ-transfers that populate these states can be found, constraining the spin/parities of those states. This means the values of alpha partial widths extracted from alpha-transfer experiments [116, 174] can be constrained, reducing the uncertainty in the resonance strengths involved in the ^{22}Ne$(\alpha, \gamma)^{26}$Mg and ^{22}Ne$(\alpha, n)^{25}$Mg reactions. In addition, information on spin/parity can also provide guidance on whether the state has natural parity, and thus will contribute to the ^{22}Ne$(\alpha, \gamma)^{26}$Mg and ^{22}Ne$(\alpha, n)^{25}$Mg reactions. The constraints that can be placed on these states will be discussed in this chapter, with an emphasis on states astrophysically relevant to the ^{22}Ne $+ \alpha$ reactions at

temperatures experienced in massive stars.

5.2 Excited states of ^{26}Mg above the alpha threshold observed in the ^{25}Mg(d, p)^{26}Mg reaction

The spectra obtained in this study (shown later in Figures 5.3, 5.4, 5.5 and 5.6) were calibrated using a polynomial fit of magnetic rigidity ($B\rho$) to channel number for selected excited states of ^{26}Mg that had been observed in previous studies and appeared as well-defined peaks in the current work. Table 5.1 shows the excitation energies used in the calibration of the spectrometer, chosen as they were precisely measured in previous studies, well populated in the current study (with minimal overlap with other states), and covered the region of the spectrometer of astrophysical interest well. A least-squares fit using a second order polynomial was chosen for this calibration due to the lowest reduced chi-squared value of its fit compared to other polynomials.

Table 5.1 *Excitation energies of energy levels used in the energy calibration, with sources of the excitation energy values in footnotes.*

E_x [MeV]	ΔE_x [MeV]
10.6001 [a]	0.0004
10.6819 [a]	0.0003
10.719 [b]	0.002
10.928 [b]	0.001
10.978 [c]	0.003
10.998 [b]	0.001
11.047 [b]	0.001
11.11223 [d]	0.00041
11.15338 [d]	0.00041
11.24286 [d]	0.00041

[a] Basunia *et al.* (2016) [81].
[b] Adsley *et al.* (2018) [175].
[c] Moss *et al.* (1976) [181].
[d] Massimi *et al.* (2017) [180].

The fit of the calibration of $B\rho$ to channel number is shown in Figure 5.1, with the residuals of the fit shown in Figure 5.2. The uncertainties are calculated as a quadrature sum of uncertainty in the literature value and the fit uncertainty.
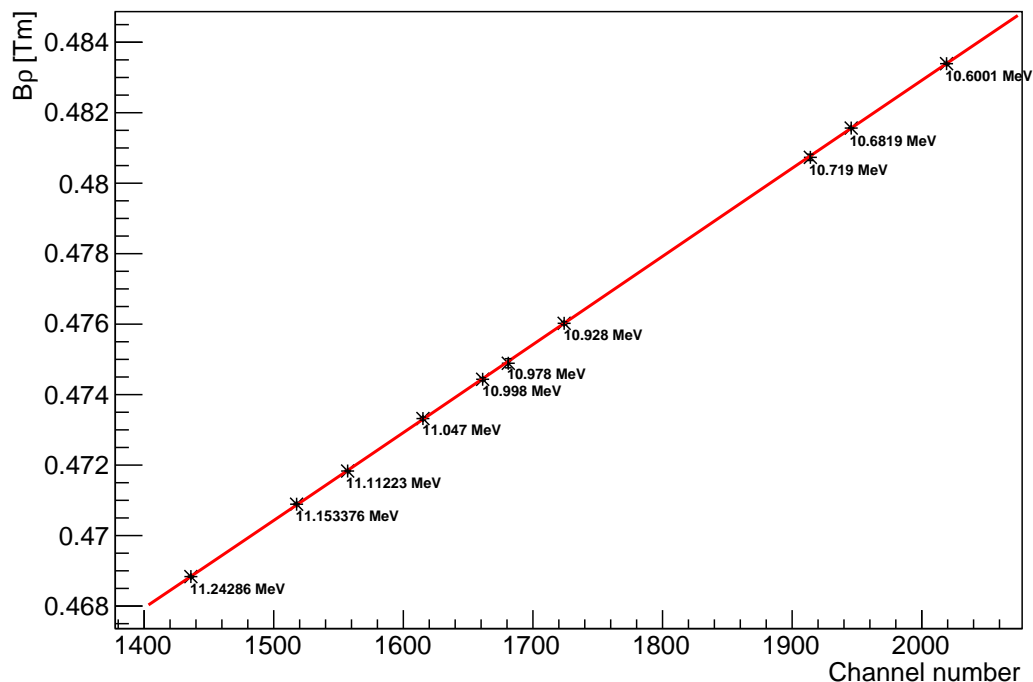
Figure 5.1 *Magnetic rigidity against channel number for known states of ^{26}Mg at a lab angle of $10°$. Excited states used in the fit and their uncertainties are given in Table 5.1.*
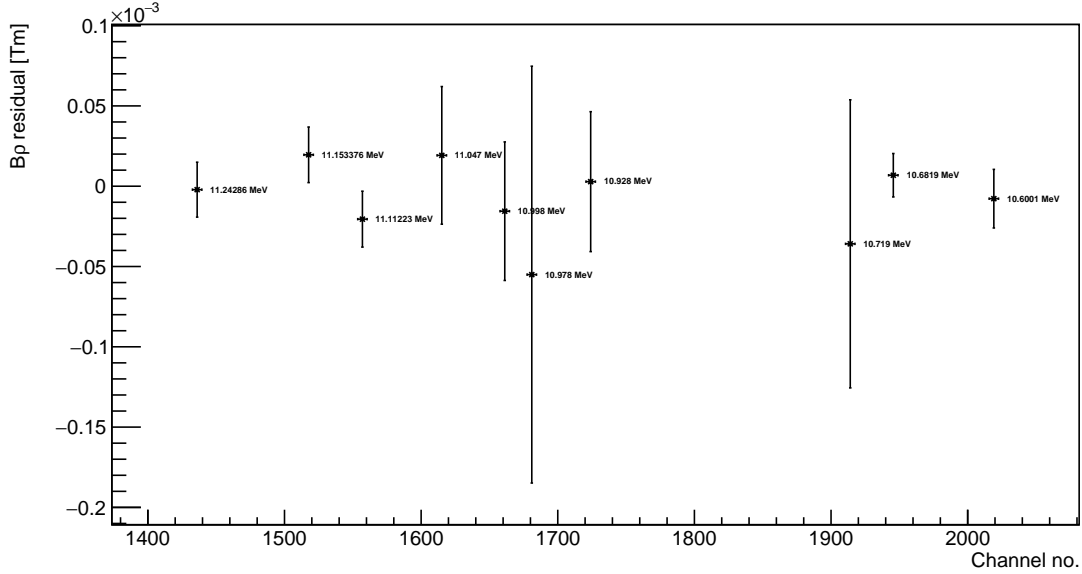
Figure 5.2 *Magnetic rigidity residuals against channel number for known states of ^{26}Mg at lab angle of $10°$. Excited states used in the fit and their uncertainties are given in Table 5.1.*

As can be seen in Figure 5.2, the chosen polynomial fits the data well. The overlap of the residuals with zero does indicate that the uncertainties may be slightly over-estimated, with the uncertainties in magnetic rigidity coming from literature values of excitation energies of ^{26}Mg and the Q-value of the ^{25}Mg(d, p) reaction. Spectra are shown in Figures 5.3, 5.4, 5.5 and 5.6, with states observed in the current experiment labelled and fitted with Voigt functions (the widths of states near and above the neutron threshold may have the intrinsic width of the state contributing to the observed peak width, in addition to the experimental resolution). The Voigt function is defined as a convolution of a Gaussian function and a three-parameter Lorentz (Breit-Wigner/Cauchy) function. The Gaussian function is defined as:

$$G(x) = \frac{A}{\sigma\sqrt{2\pi}} \exp{-\frac{1}{2}\left(\frac{x - \mu}{\sigma}\right)^2}, \tag{5.1}$$

where

$A \equiv$ scaling factor of function

$\sigma \equiv$ standard deviation of function

$\mu \equiv$ mean of the function.

The three-parameter Lorentz function is defined as:

$$L(x) = I\left[\frac{\gamma^2}{(x - x_0)^2 + \gamma^2}\right], \tag{5.2}$$

where

$I \equiv$ height of peak

$\gamma \equiv$ scale parameter for width of peak

$x_0 \equiv$ location of centre of peak.

Table 5.2 shows the states observed in the current experiment, alongside those observed in previous studies. Literature levels are taken from a range of studies, with the study reporting the smallest excitation energy uncertainty for a state being presented in the table.

In this experiment, all peaks measured could be matched to at least one state in ^{26}Mg described in a previous study, indicating no new states were observed in the current experiment. While the (d, p) reaction is most sensitive to states with large neutron spectroscopic factors, and cannot populate very high-spin states, this lack of discovery of new states suggests that our current knowledge

of the energies of the states just above the alpha threshold in ^{26}Mg is now fairly comprehensive. This indicates that our understanding of which states drive the ^{22}Ne$(\alpha, \gamma)^{26}$Mg and ^{22}Ne$(\alpha, n)^{25}$Mg reactions that determine the neutron budget in the weak s-process is approaching being well established.

Late on in the writing of this thesis, a paper was published describing the measurement of the ^{25}Mg$(d, p)^{26}$Mg reaction using a deuteron beam of energy 56 MeV [182]. However, this work had a different emphasis to that described in this thesis, and investigated whether the (d, p) reaction is an appropriate surrogate reaction to neutron capture reactions on ^{25}Mg, with a poorer experimental resolution than that in the current work.

E_x (current) [MeV]	E_x (lit) [MeV]	Ref.	Reaction mechanism(s)
10.600(2)	10.6001(4) *	[81]	$(\alpha, p\gamma)$, (n, γ), (p, p')
10.648(2)	10.6473(8)	[177]	$(\gamma, \bar{\gamma})$
	10.650(1) [1]	[175]	(p, p')
	10.6507(4) [2]	[176]	heavy-ion fusion/γ decay
10.682(2)	10.6819(3) *	[183]	(n, γ)
	10.6963(4)	[176]	heavy-ion fusion/γ decay
	10.704(2)	[176]	heavy-ion fusion/γ decay
	10.706(1)	[175]	(p, p')
10.717(2)	10.719(2) *	[175]	(p, p'), (d, d')
	10.730(2)	[175]	(p, p'), (d, d')
10.743(2)	10.742(3)	[176]	heavy-ion fusion/γ decay
	10.74598(12)	[183]	(n, γ)
10.766(2)	10.767(2)	[81]	(p, p'), $(\alpha, p\gamma)$
	10.771(1)	[175]	(p, p'), (d, d')
10.802(2)	10.8059(4)	[183]	(n, γ)
	10.818(1)	[175]	(p, p'), (d, d')
10.823(2)	10.826(1)	[175]	(p, p'), (d, d')
10.880(2)	10.882(1)	[175]	(p, p'), (d, d')
10.896(2)	10.893(1)	[175]	(p, p'), (d, d')
10.915(2)	10.915(1)	[175]	(p, p'), (d, d')
10.928(2)	10.928(1) *	[175]	(p, p'), (d, d')
10.947(2)	10.943(2)	[175]	(d, d')
	10.9491(8)	[177]	$(\gamma, \bar{\gamma})$
10.975(2)	10.978(3) *	[181]	(p, p')
10.997(1)	10.998(1) *	[175]	(p, p'), (d, d')
11.016(1)	11.012(3)	[175]	(p, p'), (d, d')
	11.017(1)	[175]	(p, p'), (d, d')
	11.039(3)	[176]	heavy-ion fusion/γ decay
11.047(1)	11.047(1) *	[175]	(p, p'), (d, d')
11.072(1)	11.074(1)	[175]	(p, p'), (d, d')
11.082(1)	11.084(1)	[175]	(p, p'), (d, d')
	11.102(1)	[175]	(p, p'), (d, d')
11.112(1)	11.11223(4) *	[180]	(n, γ), (n, tot)
	11.119(1)	[175]	(p, p'), (d, d')

Table 5.2 *Excitation energies of states of ^{26}Mg observed in the present work using the (d, p) reaction, compared to those seen in previous studies, with references and reaction mechanisms given. States used in the energy calibration are marked with asterisks.*

---

[1] 1^+ state described in Ref. [81].

[2] 7^- state described in Ref. [176] (population forbidden in the current work).
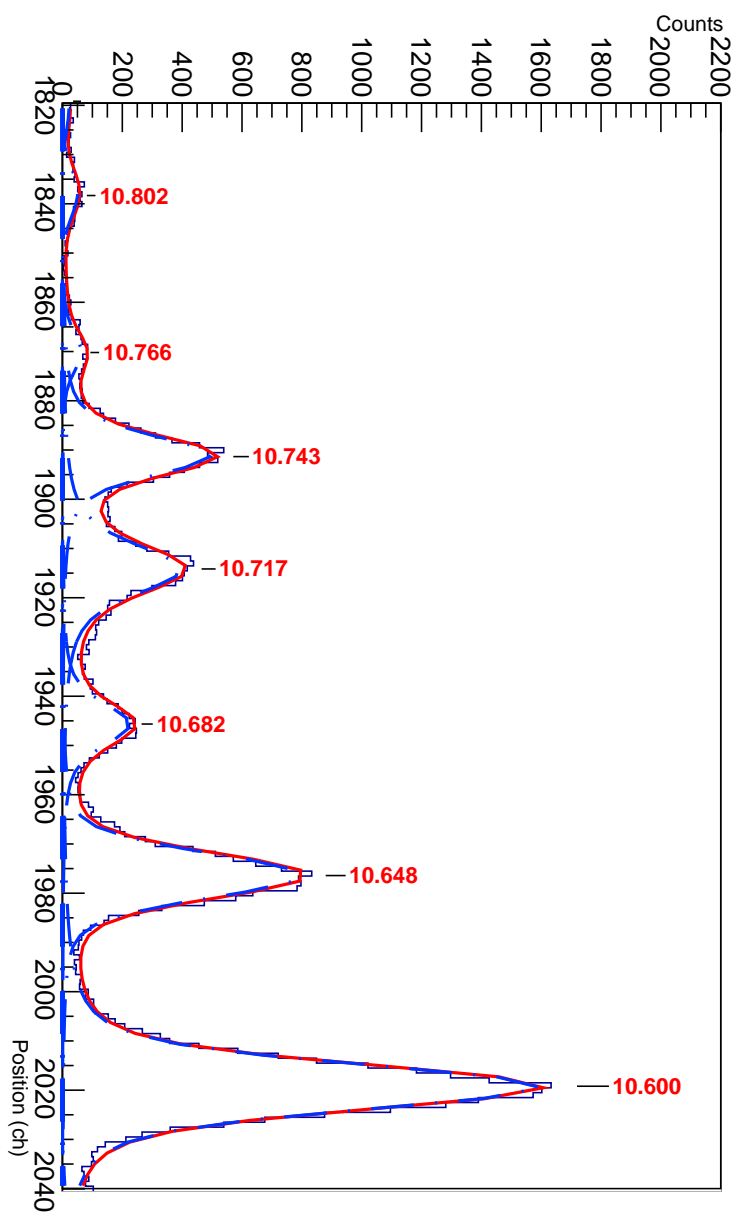
Figure 5.3 *Spectrum of the $^{25}Mg(d,p)^{26}Mg$ reaction at θ_{lab}=10°. Peaks are fitted with Voigt functions, with individual fits shown in dashed blue and the sum of fits in solid red. Excitation energies in MeV calculated in this work (see Table 5.2) are noted in red.*
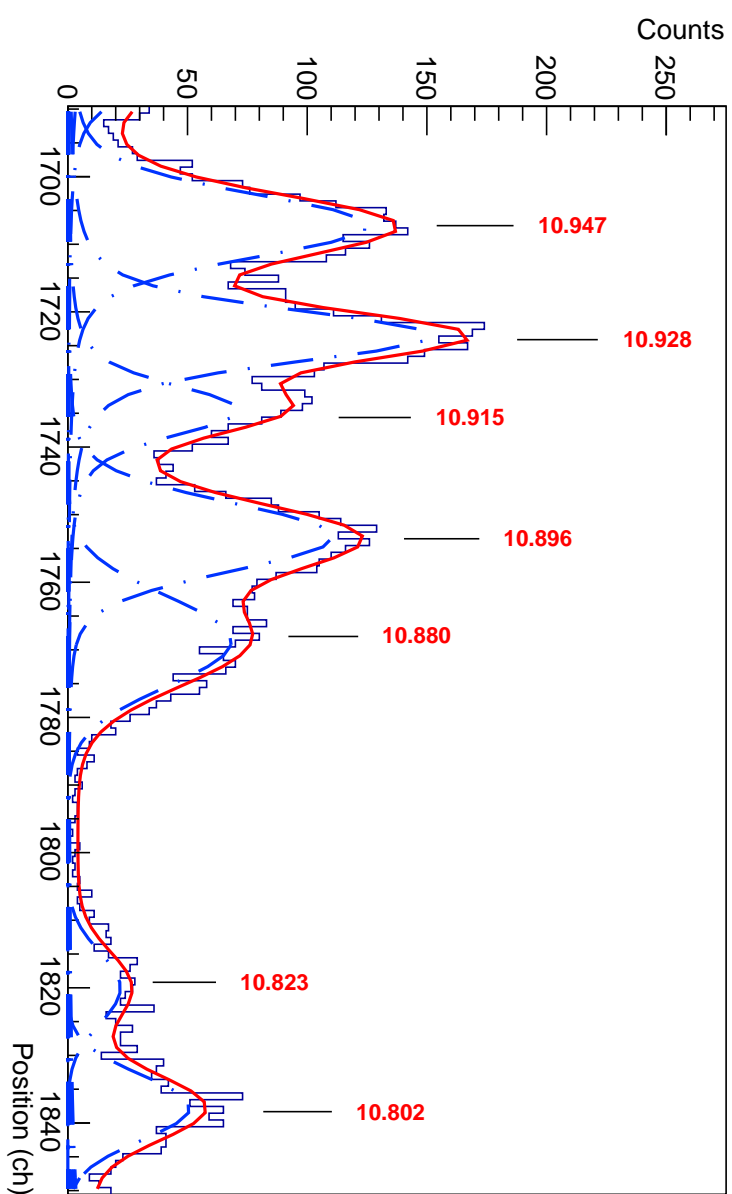
Figure 5.4 *Same as Figure 5.3 above, at higher excited states.*
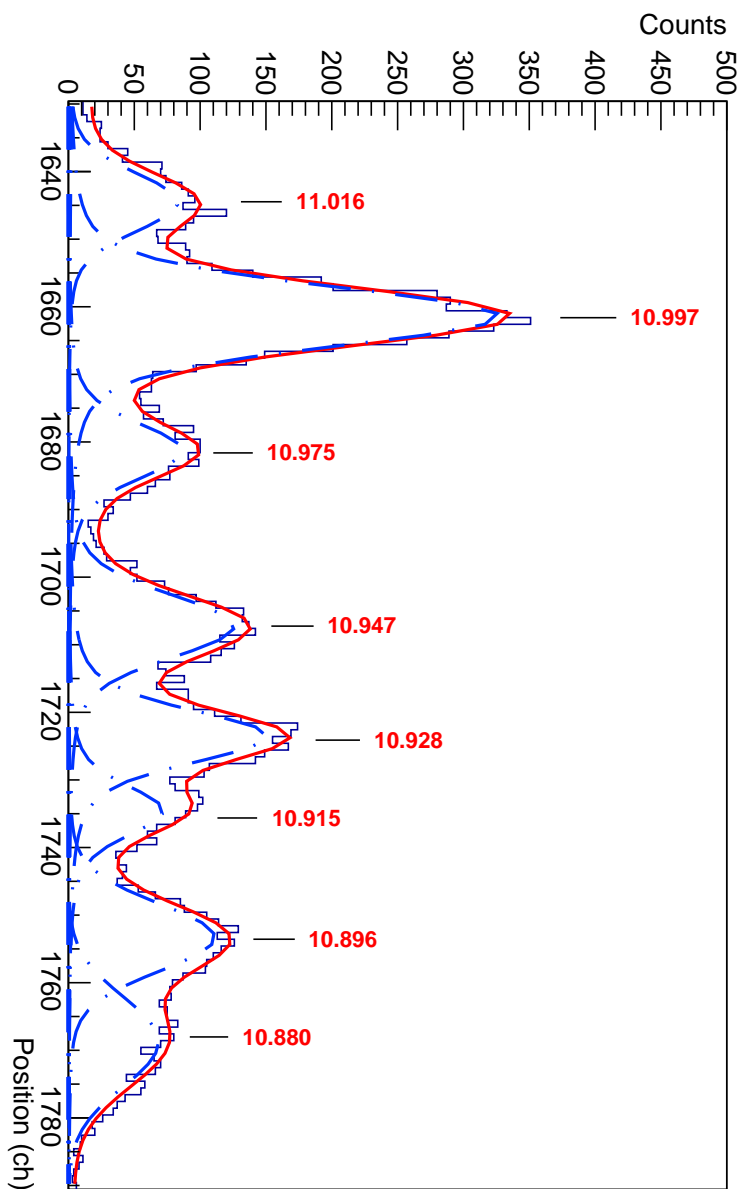
Figure 5.5 *Same as Figure 5.3 above, at higher excited states.*
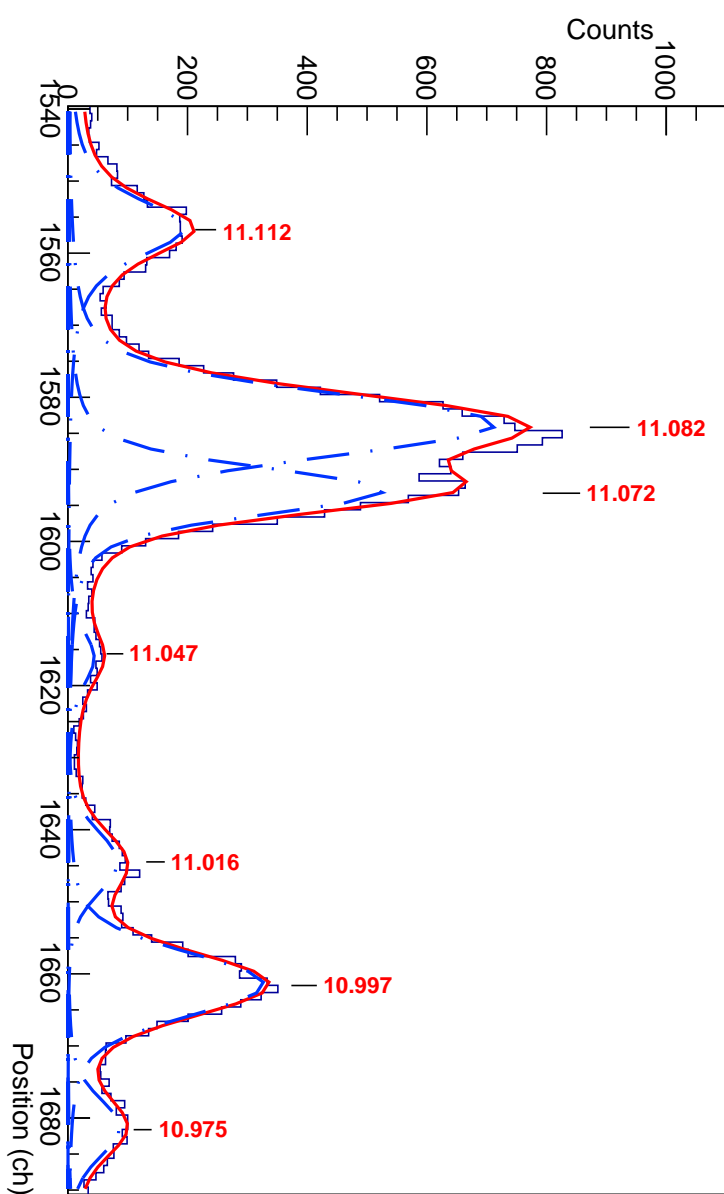
Figure 5.6 *Same as Figure 5.3 above, at higher excited states.*

5.3 Angular distributions of states of ^{26}Mg above the alpha threshold populated using the ^{25}Mg(d, p)^{26}Mg reaction

This section presents some of the angular distributions of excited states measured in the current work, fitted using weakly bound DWBA calculations performed with FRESCO (previously discussed in §2.3).

The angular distributions of states presented in this section are those relevant to known resonances in ^{26}Mg that drive the ^{22}Ne$(\alpha, \gamma)^{26}$Mg and ^{22}Ne$(\alpha, n)^{25}$Mg reactions in the weak s-process. Those relevant to the ^{22}Ne $+ \alpha$ reactions have been measured in the recent alpha-transfer experiments of Jayastissa *et al.* [116] or Ota *et al.* [174], but reliable values of the alpha partial widths extracted rely on well-established spin/parities of states.

States around 10.8 MeV

Two peaks were observed at excitation energies of 10.802(2) and 10.823(2) MeV in the current work. The peak at 10.802(2) MeV is fitted very well at the most forward angles by an $\ell=1$ component, as shown in Figure 5.7.

At larger lab angles of emission, the smaller impact parameter in the reaction will make multi-step processes more likely. Thus, the single-step mechanism of the DWBA calculations is not expected to fit larger angles perfectly, but will replicate the most forward angles well. This contrasts with the first experiment discussed in this thesis, where some of the more forward angles required the addition of a compound component to describe their angular distributions. In addition, these multi-step mechanisms mean that measurements of differential cross sections at more backward angles will not provide further clarification on which ℓ-transfers can populate that excited state, and thus the spin/parities that state could possibly have.
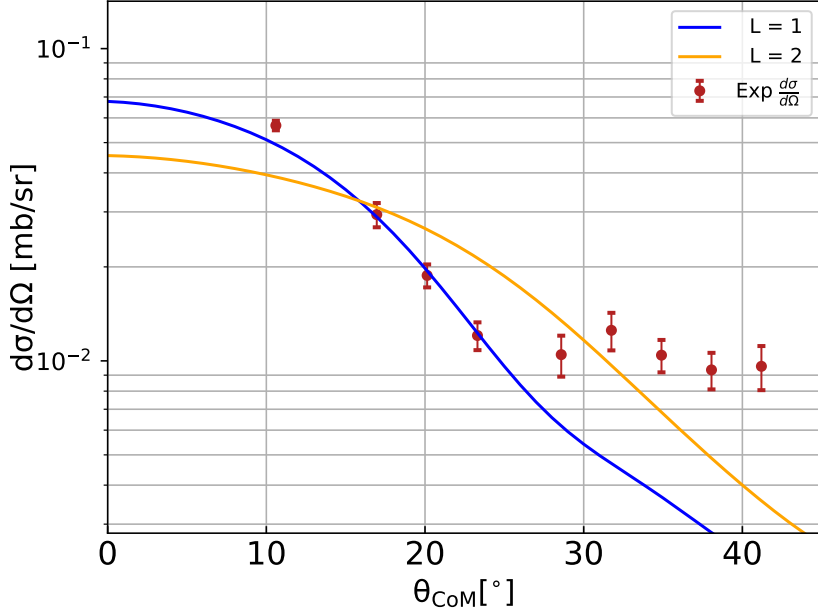
Figure 5.7 *Differential cross section angular distribution of peak observed at 10.802 MeV.*

A state was observed by the photoexcitation experiment of Longland *et al.* [177] at an energy of 10.8057(7) MeV, and assigned a spin/parity of 1^-, an assignment which was also given by the (α, α') scattering of Talwar *et al.* [173] to a state in this region. The $\ell=1$ angular distribution shown in Figure 5.7 is consistent with these 1^- assignments.

The angular distribution of the state at 10.802(2) MeV can be contrasted with that of the peak observed at 10.648(2) MeV in the current work. This state was seen by Longland *et al.* [177] at 10.6473(8) MeV and assigned $J^\pi{=}1^+$ (the unnatural parity of this state means it cannot contribute to the ^{22}Ne $+ \alpha$ reactions). As can be seen in Figure 5.8, an $\ell=2$ angular distribution fits the differential cross section distribution best, which is in agreement with the spin/parity assigned by Longland *et al.* [177].
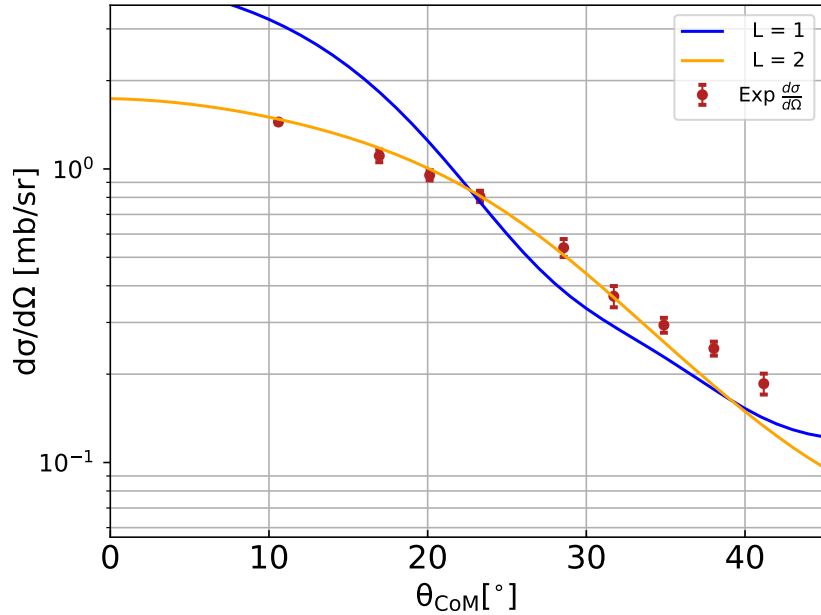
Figure 5.8 *Differential cross section angular distribution of peak observed at 10.648 MeV.*

The distinct structure seen in the angular distribution of the peak observed at 10.823(2) MeV in the current experiment, as can be seen in Figure 5.9, can only be explained by an $\ell=0$ transfer to reach the final excited state.
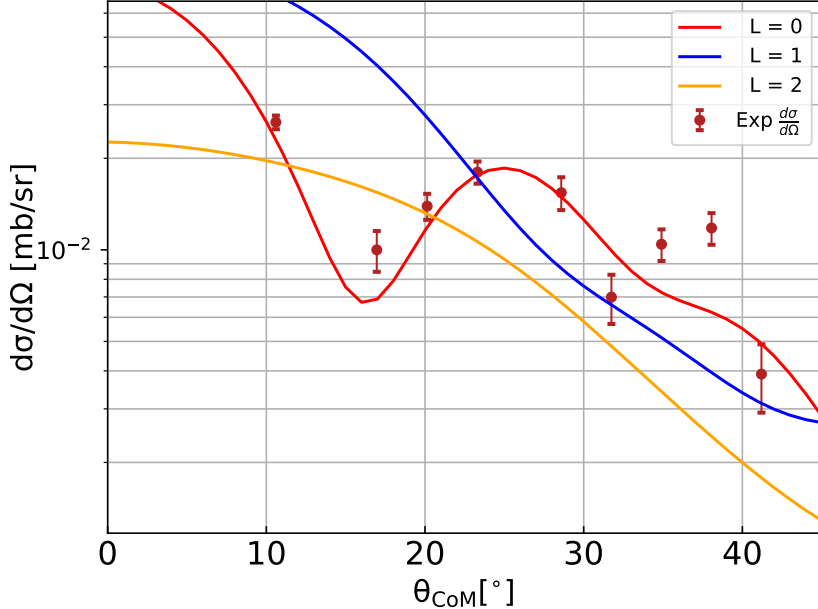
Figure 5.9 *Differential cross section angular distribution of peak observed at 10.823 MeV.*

This constrains the spin/parity of the state to either 2^+ or 3^+ and, as this state has been seen in alpha transfer experiments [116, 174], it can only have natural parity, giving a spin/parity assignment of 2^+. While this assignment comes from only a small number of data points, it is in agreement with the electron scattering experiment of Lees *et al.* [147] and the γ-decay experiment of Lotay *et al.* [176]. DWBA fits to electron scattering data by Lees *et al.* gave an assignment of 2^+ to a state measured at 10.838(24) MeV. The experiment by Lotay *et al.* constrained the spin/parity of what was assumed to be the same state (with an excitation energy of 10.823(3) MeV) to $J=(2\text{-}6)$.

The high resolution proton and deuteron scattering experiment from Adsley *et al.* indicates that there are three excited states of ^{26}Mg in this region, at excitation energies of 10.806(1), 10.818(1) and 10.826(1) MeV [175]. An alpha-particle inelastic scattering experiment from Adsley *et al.* [178] indicated a 0^+ state exists at 10.824(10) MeV, while a high energy (p, p') experiment from Ref. [184] observed a 1^+ state at around 10.82 MeV. No evidence of population of a 0^+ or 1^+ state around 10.8 MeV was found in the current work, which would have had a clear $\ell=2$ transfer in the angular distribution. This is consistent with only two states observed with a separation of $\sim$20 keV, which remained across all angles measured, thus matching well to the states at 10.806 and 10.826 MeV.

The excited state at 10.826 MeV corresponds to a resonance in the ^{22}Ne$(\alpha, \gamma)^{26}$Mg

reaction rate, which contributes to the reaction rate at lower temperatures, below $\sim$0.2 GK. Combining the spin/parity assignment of 2^+ (and thus eliminating the possibility of a 0^+ or 1^- assignment) with the results of the alpha-transfer study of Jayatissa *et al.* [116] gives an extracted alpha partial width of $\Gamma_\alpha = 2.1 \pm 0.3(stat.) \pm 0.4(sys.) \times 10^{-22}$ eV, as shown in Table 5.4.

The higher-energy measurement of the ^{25}Mg$(d,p)^{26}$Mg reaction by Chen *et al.* [182] failed to resolve the individual states in this region.

State at 11.082 MeV

The angular distribution of the peak observed at 11.082(1) MeV in the current experiment is fitted best by an ℓ=2 transfer, as shown in Figure 5.10, only allowed by a positive-parity state.
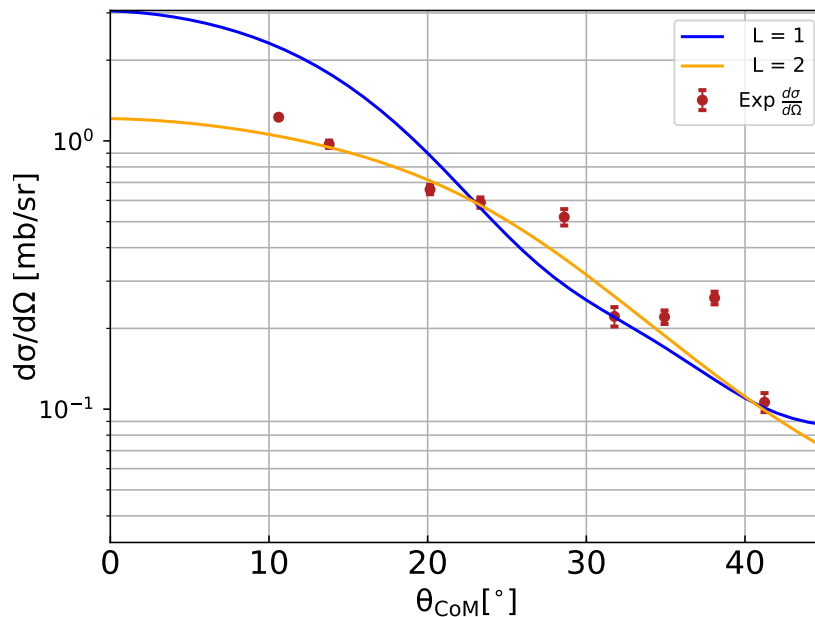
Figure 5.10 *Differential cross section angular distribution of peak observed at 11.082 MeV.*

The proton inelastic scattering experiment of Adsley *et al.* [178] observed an excited state at an energy of 11.084(1) MeV. This state had been seen previously in the alpha-scattering experiment of Talwar *et al.* [173], with an assignment of either 2^+ or 3^- from comparison to DWBA angular distributions. The γ decay

study of Lotay *et al.* [176] observed an angular distribution that could not be reconciled with the 3^- assignment, and thus deemed it to be a 2^+ state.

In the ^{25}Mg$(d, p)^{26}$Mg study of Chen *et al.* [182], a peak at an energy of 11.069(10) MeV (indicating several states are contributing to the peak in that work), fitted by an $\ell=2$ transfer, suggesting a strong, positive-parity state is present in this region.

The angular distribution observed in the current work provides confirmation that this excited state has a positive parity, consistent with a 2^+ (and not 3^-) spin/parity assignment, and thus reduces the uncertainty in the alpha partial width of the resonance that dominates the ^{22}Ne$(\alpha, \gamma)^{26}$Mg reaction rate, giving it a value of $\Gamma_\alpha = 5.7 \pm 0.7(\text{stat.})^{+1.4}_{-1.2}(\text{sys.}) \times 10^{-11}$ eV, when combined with the results of Jayatissa *et al.* [116], as shown in Table 5.4.

Peak at 11.112 MeV

In the current experiment, a peak is observed with an excitation energy of 11.112(1) MeV. This matches a state seen at 11.113(1) MeV observed through the (p, p') and (d, d') scattering experiments of Adsley *et al.* [178] and a state measured at 11.112 MeV by the neutron capture reactions of Massimi *et al.* [179, 180]. These neutron capture reactions were analysed with an R-matrix code to assign a spin/parity of 2^+ to this state.

In the current work, the angular distribution is fitted well by the $\ell=2$ transfer, consistent with a 2^+ state, as shown in Figure 5.11.
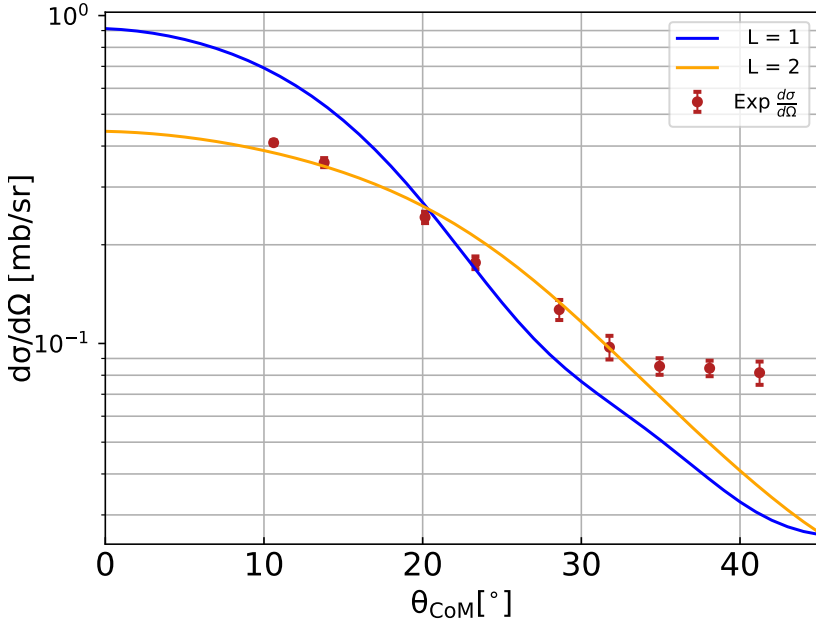
Figure 5.11 *Differential cross section angular distribution of peak observed at 11.112 MeV.*

This is consistent with the spin/parity of 2^+ used to place an upper limit on the extracted alpha partial width in the alpha transfer experiment of Ota *et al.* [174], indicating the reliability of the limit of $\Gamma_\alpha < 2.2 \times 10^{-10}$ eV for the resonance that dominates the ^{22}Ne$(\alpha, n)^{25}$Mg at low temperatures ($\sim$0.2 GK) [174].

In the (d, p) study of Chen *et al.* [182], a peak observed at 11.112(10) MeV was fitted with an ℓ=3 transfer, but contains contributions from several nearby states.

Peak at 10.947 MeV

A peak was observed in the spectrum of the current experiment at 10.947(2) MeV, consistent with production from a single state. This excitation energy matches the state at 10.9491(8) MeV seen in the photoexcitation study of Longland *et al.* [177], who assigned it a spin/parity of 1^-. The angular distribution measured in the current work is not fitted well by a pure ℓ=1 or pure ℓ=2 transfer, as can be seen in the left hand side of Figure 5.12, with no improvement provided by the addition of an ℓ=0 transfer to the ℓ=2 component. A combination of the ℓ=1 and ℓ=3 transfers fits the angular distribution best, as can be seen in Figure 5.12, consistent with the population of a 1^- state.
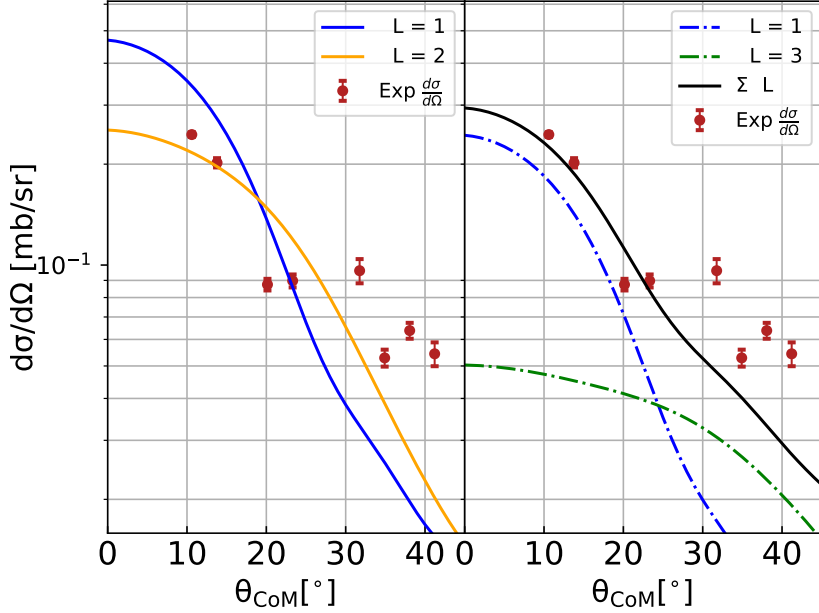
Figure 5.12 *Differential cross section angular distribution of peak observed at 10.947 MeV.*

The inelastic scattering experiment of Adsley *et al.* [175] observed another state at 10.943(2) MeV through the (d, d') reaction (a contaminant peak obscured the state in the (p, p') spectrum). This same state was observed at an energy of 10.943(4) MeV and assigned a range of possible spin/parities (5^-, 6^+, 7^-) by the γ-decay study of Lotay *et al.* [176]. As none of these spin/parities proposed by Lotay *et al.* can be populated by an $\ell=1$ transfer, the component of the angular distribution that dominates the more forward angles in the current work must have come exclusively from the lower-spin state, meaning the distribution observed in the current work is consistent with the spin/parity assignment of 1^- to the 10.949 MeV state.

The alpha-transfer experiment of Jayatissa *et al.* [116] populated a state with an excitation energy of 10.95(2) MeV. The sub-Coulomb beam energy used preferentially populates low-spin states, meaning the high-spin state at 10.943 MeV is very unlikely to be contributing to the alpha-transfer yield. Using the recommended spin/parity of 1^- for the state at 10.949 MeV, an alpha partial width of $\Gamma_\alpha = 3.0 \pm 0.3(\text{stat.})^{+0.75}_{-0.6}(\text{sys.}) \times 10^{-14}$ eV was extracted, as shown in Table 5.4. This reduces the uncertainty in this state's contribution to the $^{22}\text{Ne}(\alpha, \gamma)^{26}\text{Mg}$ reaction rate, which is expected to be significant at lower temperatures.

E_x (lit) [MeV]	E_x (current) [MeV]	ℓ-transfer (current)	Recommended J^π
10.8059	10.802	1	1^-
10.826	10.823	0	2^+
10.9491	10.947	1+3	1^-
11.084	11.082	2	2^+
11.112227	11.112	2	2^+

Table 5.3 *Excited states discussed in the previous section, with the permitted ℓ-transfers extracted from their angular distributions and recommended spin/parities, based on constraints from literature and the current work.*

A summary of the key ℓ-transfers constrained from the measured angular distributions and their corresponding recommended spin/parities are shown in Table 5.3. The possible alpha partial widths extracted from Ref. [116] are shown in Table 5.4, with recommended spin/parities and widths from the constraints found in this work presented. The method of extraction of alpha widths from alpha transfer reactions is described in Appendix C.

E_x [MeV] [116]	Recommended E_x [MeV]	E_r [keV]	J^π	Γ_α [eV] [116]	Recommended J^π	Recommended Γ_α [eV]
11.08(2)	11.084(1) [a]	469(1)	0^+	$1.3\pm0.1\pm0.3\times10^{-9}$		
			1^-	$2.5\pm0.3^{+0.7}_{-0.5}\times10^{-10}$		
			2^+	$5.7\pm0.7^{+1.4}_{-1.2}\times10^{-11}$	2^+	$5.7\pm0.7^{+1.4}_{-1.2}\times10^{-11}$
10.95(2)	10.9491(8)[b]	334.4(8)	0^+	$1.5\pm0.2^{+0.4}_{-0.3}\times10^{-13}$		
			1^-	$3.0\pm0.3^{+0.75}_{-0.6}\times10^{-14}$	1^-	$3.0\pm0.3^{+0.75}_{-0.6}\times10^{-14}$
			2^+	$6.4\pm0.6^{+1.0}_{-0.6}\times10^{-15}$		
10.83(2)	10.826(1)[a]	211(1)	0^+	$5.3\pm0.7^{+1.1}_{-1.0}\times10^{-21}$		
			1^-	$1.0\pm0.1^{+0.3}_{-0.2}\times10^{-21}$		
			2^+	$2.1\pm0.3\pm0.4\times10^{-22}$	2^+	$2.1\pm0.3\pm0.4\times10^{-22}$

[a] Adsley *et al.* (2018) [175].
[b] Longland *et al.* (2009) [177].

Table 5.4 *Table summarising possible alpha partial widths extracted from the yield of the alpha transfer experiment of Jayatissa et al. [116]. Recommended alpha partial widths constrained using the recommended spin/parities of the current study are given. The first and second uncertainties presented with the alpha partial widths are the statistical and systematic uncertainties from Jayatissa et al. [116]. Alpha threshold of 10.61474(3) MeV taken from Ref. [141].*

5.4 ^{22}Ne + α reaction rates for neutron production in the weak s-process

5.4.1 ^{22}Ne(α, γ)^{26}Mg and ^{22}Ne(α, n)^{25}Mg Reaction Rate Calculations

Reactions that proceed through relatively high excitation energies will tend to be dominated by resonant direct capture reactions [85]. As the ^{22}Ne(α, γ)^{26}Mg and ^{22}Ne(α, n)^{25}Mg reactions proceed through states above S_α=10614.8 keV and S_n=11093.1 keV respectively [81], the non-resonant capture component of the reaction rate will be considered negligible in the calculation of the reaction rates. The contribution for each resonance was calculated using the formalisation set out in §2.2, with the parameters used given in Table 5.5.

For low energy resonances just above the alpha threshold, as are involved in the temperatures relevant to neutron production for the s-process, the alpha partial width (Γ_α) is much smaller than that of the γ and neutron widths (Γ_γ, Γ_n). Thus, the resonance strengths for the (α, γ) and (α, n) reactions, $\omega\gamma_{(\alpha,\gamma)}$ and $\omega\gamma_{(\alpha,n)}$, can be well approximated as:

$$\omega\gamma_{(\alpha,\gamma)} \approx (2J+1)\frac{\Gamma_\alpha}{1+\frac{\Gamma_n}{\Gamma_\gamma}},$$

$$\omega\gamma_{(\alpha,n)} \approx (2J+1)\frac{\Gamma_\alpha}{1+\frac{\Gamma_\gamma}{\Gamma_n}}. \tag{5.3}$$

Table 5.5 shows the properties of the nuclear states used in the reaction rate calculations of the ^{22}Ne(α, γ)^{26}Mg and ^{22}Ne(α, n)^{25}Mg reaction rates and the studies they were taken from, including alpha partial widths constrained by the angular distributions of states shown in the previous section. For resonances associated with excited states above 11.32 MeV, resonance strengths were taken from Ref. [185] for the (α, γ) reaction and from Ref. [186] for the (α, n) reaction.

Table 5.5 *Energy level properties used to calculate $^{22}Ne(\alpha,\gamma)^{26}Mg$ and $^{22}Ne(\alpha,n)^{25}Mg$ reaction rates. Properties have been labelled with their sources, with unlabelled properties constrained by the current work (see section 5.3). Alpha threshold of 10.61474(3) MeV taken from Ref. [141].*

E_x [MeV]	E_r [MeV]	J^π	$\frac{\Gamma_n}{\Gamma_\gamma}$	Γ_α [eV]	$\omega\gamma_{(\alpha,\gamma)}$ [eV]	$\omega\gamma_{(\alpha,n)}$ [eV]
10.826 [a]	0.211	2^+	0	2.1×10^{-22} [b]	1.1×10^{-21}	—
10.9491 [c]	0.3344	1^-	0	3.0×10^{-14} [b]	9.0×10^{-13}	—
11.084 [a]	0.469	2^+	0	5.7×10^{-11} [b]	2.9×10^{-10}	—
11.11223 [d]	0.49749	2^+	1530 [d]	$<2.2\times10^{-10}$ [e]	$<7.2\times10^{-13}$	$<1.1\times10^{-9}$
11.16307 [d]	0.54833	2^+ [d]	1900 [d]	$<1.3\times10^{-11}$ [e]	$<4.8\times10^{-14}$	$<9.1\times10^{-11}$
11.16924 [d]	0.55450	3^- [d]	588 [d]	$<1.3\times10^{-11}$ [e]	$<1.5\times10^{-13}$	$<9.1\times10^{-11}$
11.17104 [d]	0.55630	2^+ [d]	0.2 [d]	$<1.3\times10^{-11}$ [e]	$<5.4\times10^{-11}$	$<1.1\times10^{-11}$
11.3195 [f]	0.7048	(0^+) [b]			4.6×10^{-5} [f]	1.2×10^{-4} [g]

[a] ^{26}Mg$(p,p')^{26}$Mg and ^{26}Mg$(d,d')^{26}$Mg - Adsley *et al.* (2018) [175].
[b] ^{22}Ne$(^6$Li$,d)^{26}$Mg - Jayatissa *et al.* (2020) [116].
[c] ^{26}Mg$(\gamma,\bar{\gamma})^{26}$Mg - Longland *et al.* (2009) [177].
[d] ^{25}Mg $+ n$ - Massimi *et al.* (2017) [180].
[e] ^{22}Ne$(^6$Li$,d)^{26}$Mg - Ota *et al.* (2020) [174].
[f] ^{22}Ne$(\alpha,\gamma)^{26}$Mg (direct measurement) - Hunt *et al.* (2019) [170].
[g] ^{22}Ne$(\alpha,n)^{25}$Mg (direct measurement) - Jaeger *et al.* (2001) [186].

The calculated rates for the ^{22}Ne$(\alpha,\gamma)^{26}$Mg and ^{22}Ne$(\alpha,n)^{25}$Mg reactions are plotted in Figure 5.13, with the ratio of their rates shown in Figure 5.14. The normalised contributions of each individual resonance to the total reaction rate are shown in Figures 5.15 and 5.16 respectively.
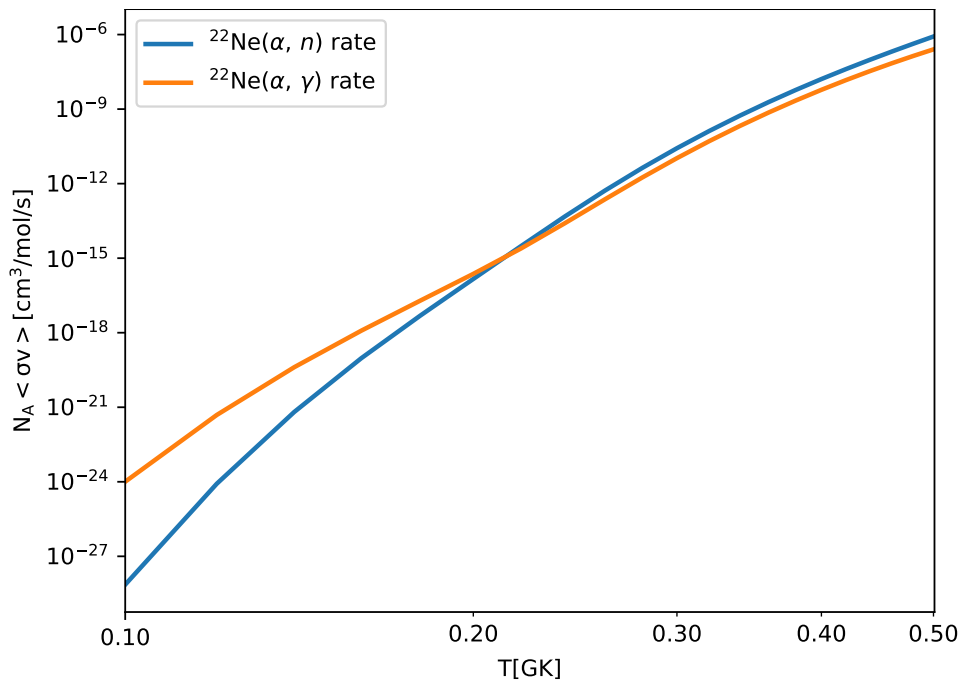
Figure 5.13 *Calculated $^{22}Ne(\alpha,\gamma)^{26}Mg$ and $^{22}Ne(\alpha,n)^{25}Mg$ reaction rates, using parameters from Table 5.5.*
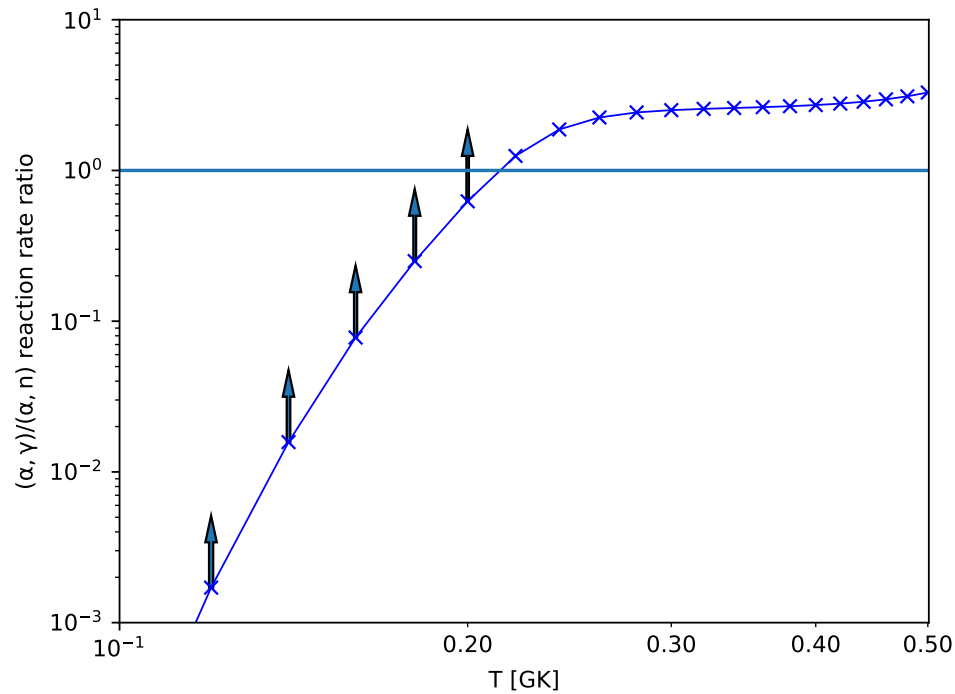
Figure 5.14 *Ratio of $^{22}Ne(\alpha,\gamma)^{26}Mg$ and $^{22}Ne(\alpha,n)^{25}Mg$ reaction rates, calculated using parameters from Table 5.5. The upwards pointing arrows show the temperatures at which the reaction rate ratio can be considered to be a lower limit.*
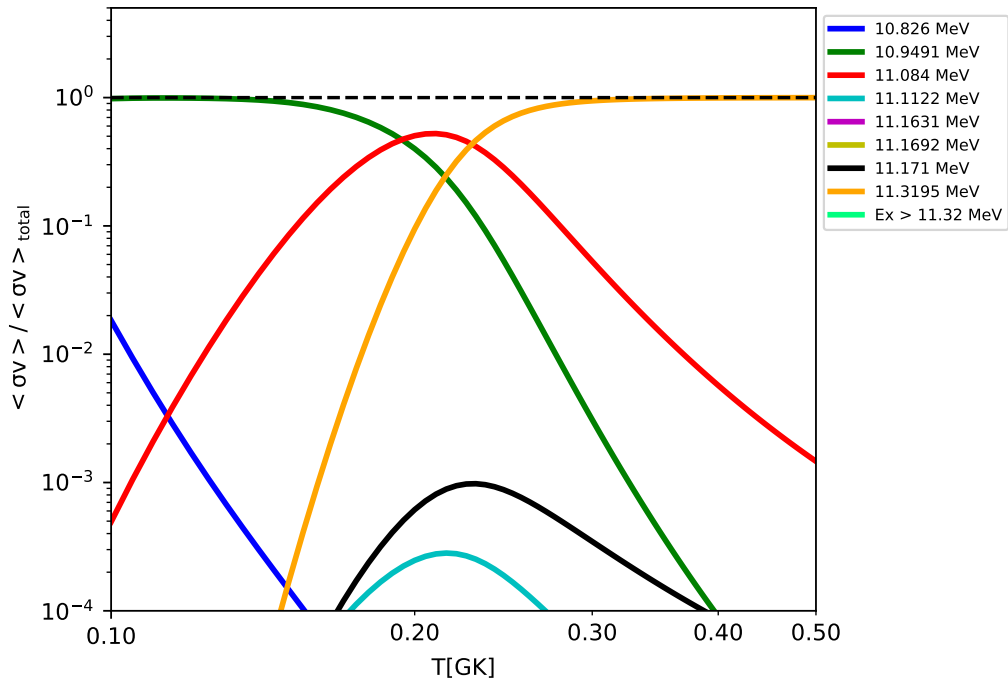
Figure 5.15 *Individual resonances of the $^{22}Ne(\alpha,\gamma)^{26}Mg$ reaction, normalised to the total reaction rate, using parameters from Table 5.5.*
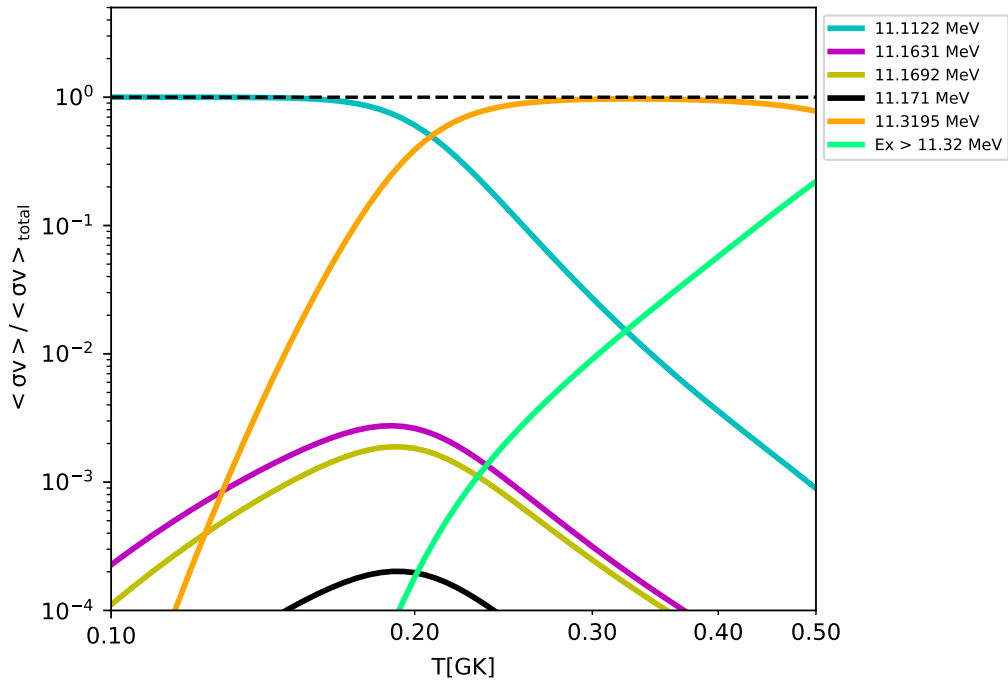
Figure 5.16 *Individual resonances of the $^{22}Ne(\alpha,n)^{25}Mg$ reaction, normalised to the total reaction rate, using parameters from Table 5.5.*

As can be seen in Figure 5.15, the ^{22}Ne$(\alpha, \gamma)^{26}$Mg reaction rate is dominated at low temperatures by the resonance associated with E_x=10.9491 MeV, at temperatures around 0.2 GK by the resonance associated with E_x=11.084 MeV, and by the resonance associated with E_x=11.3195 MeV at higher temperatures. The resonance associated with 10.826 MeV contributes a small amount to the reaction rate at low temperatures, and resonances above 11.32 MeV contribute up to $\sim$10% at higher temperatures.

For the ^{22}Ne$(\alpha, n)^{25}$Mg reaction, as shown in Figure 5.16, the resonances associated with the excitation energies of 11.112 and 11.3195 MeV almost completely dominate the reaction rate below and above 0.2 GK respectively, with resonances above 11.32 MeV contributing over 10% of the reaction rate at temperatures above $\sim$0.5 GK.

5.4.2 Comparisons of ^{22}Ne$(\alpha, \gamma)^{26}$Mg and ^{22}Ne$(\alpha, n)^{25}$Mg reaction rates to previous work

Figures 5.17 and 5.18 present the ^{22}Ne$(\alpha, \gamma)^{26}$Mg and ^{22}Ne$(\alpha, n)^{25}$Mg reaction rates calculated in the current work as ratios of the rates calculated in the Monte Carlo study of Longland *et al.* (2012) [187]. These Figures also compare reaction rates calculated using the alpha partial widths given in Table 1 of Jayatissa *et al.* [116] and the ratios of neutron and gamma partial widths given in Table 3 of Ota *et al.* [174] to Longland *et al.* (2012) [187]. Due to the complexity of the uncertainties in the parameters that contribute to the reaction rates, a truly comprehensive representation of the uncertainties associated with the reaction rates would require a dedicated Monte Carlo analysis of the available information, beyond the scope of the work in this thesis. What is presented here, however, can be considered recommended rates for the two reactions.
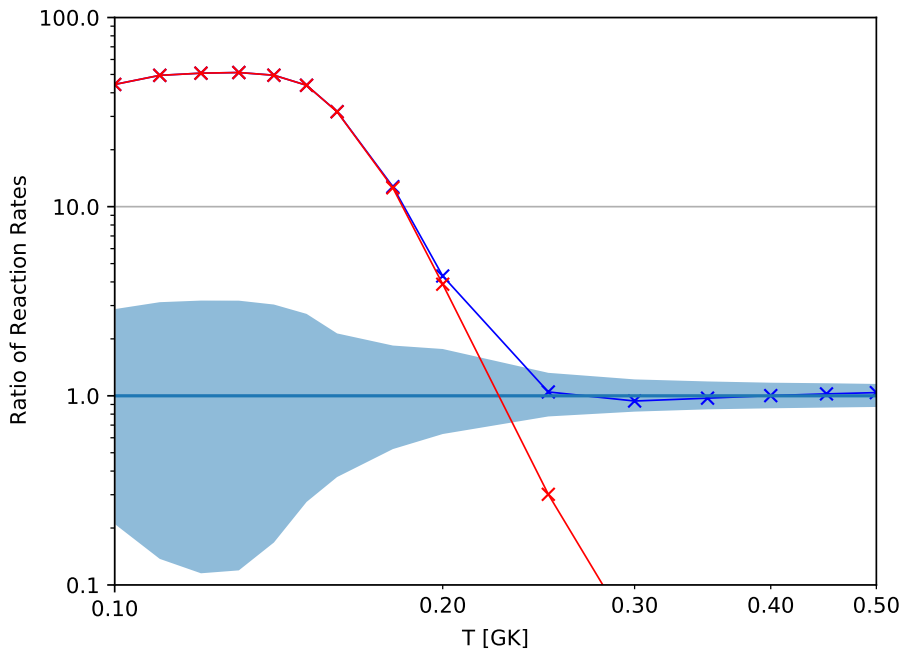
Figure 5.17 *The $^{22}Ne(\alpha,\gamma)^{26}Mg$ reaction rate calculated in the current work (blue) and using the parameters extracted in Jayatissa et al. [116] (red), presented as a ratio to the median reaction rate of Longland et al. [187]. The "low rate" and "high rate" from Longland et al. are indicated by the shaded areas.*
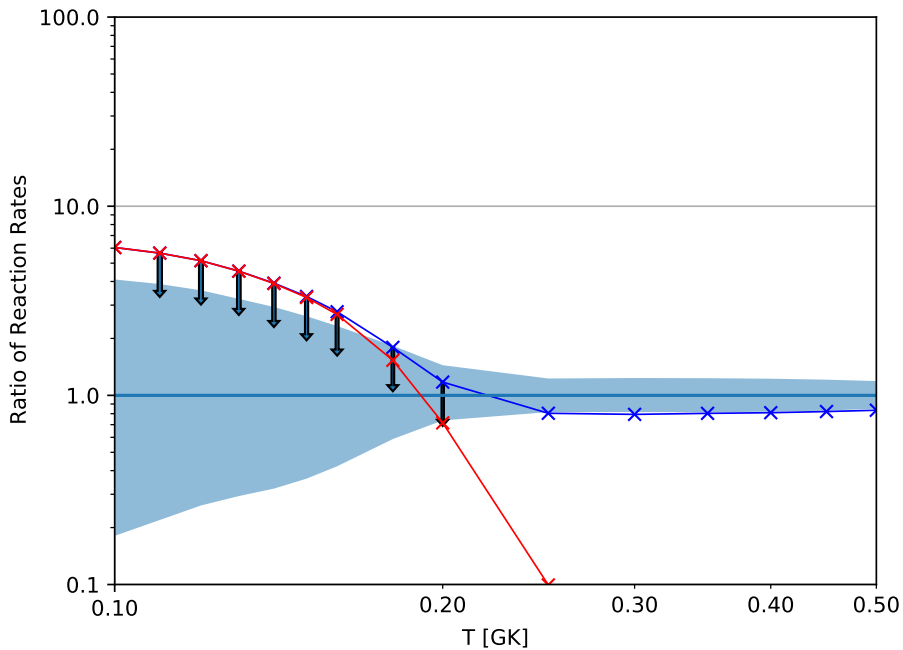
Figure 5.18 *The $^{22}Ne(\alpha,n)^{25}Mg$ reaction rate calculated in the current work (blue) and using the parameters extracted in Jayatissa et al. [116] (red), presented as a ratio to the median reaction rate of Longland et al. [187]. The "low rate" and "high rate" from Longland et al. are indicated by the shaded areas. Arrows indicate the temperatures at which the reaction rate ratio should be considered an upper limit.*

110

As can be seen in Figure 5.17, the rate of the ^{22}Ne$(\alpha, \gamma)^{26}$Mg reaction is now considered to be much greater at temperatures below $\sim$0.25 GK. This is due to the contributions from the resonances associated with the states at 10.949 and 11.084 MeV, which dominate the reaction rate at these temperatures (as can be seen in Figure 5.15) and have only recently had their alpha partial widths measured. Longland *et al.* [187] relied on calculating a theoretical upper limit to estimate the size of the partial width of the 10.949 MeV state, while the reaction rate calculations presented in the current work used the (larger) alpha width measured recently in the alpha transfer study described in Ref. [116]. In addition, the state at 11.084 MeV had not been identified at the time of publication of Longland *et al.* (2012), and therefore the contributions from the resonance associated with this state were only included in later reaction rate calculations. Above 0.25 GK, the current reaction rate and that of Longland *et al.* (2012) are similar, as the rate is dominated by the resonance associated with the state at 11.3195 MeV, which has had concordant measurements of its strength in direct studies [170, 185]. The lower reaction rate from Jayatissa *et al.* [116] at higher temperatures can be explained by the extraction of an alpha partial width for the state at 11.3195 MeV that is lower than that extracted in direct studies [170, 185].

Figure 5.18 shows the current ^{22}Ne$(\alpha, n)^{25}$Mg reaction rate normalised to that of Longland *et al.* [187]. At temperatures below 0.2 GK, the reaction rate is dominated by a resonance associated with an excited state at 11.112 MeV, as shown in Figure 5.16, which has only had the upper limit of its alpha partial width measured. Therefore, the reaction rate calculated at these temperatures in the current work should be considered an upper limit, with the true reaction rate possibly below that recommended by Longland *et al.*. At temperatures above 0.2 GK, the resonance associated with the state at 11.3195 MeV dominates the reaction rate (with other resonances that have been directly measured becoming more significant around 0.5 GK). No direct measurement of this resonance has been published since the work of Jaeger *et al.* [186] that was used in Longland *et al.*, and so the understanding of the contribution of this resonance to the reaction rate remains unchanged. For the resonances associated with the states at 11.163 and 11.171 MeV, Longland *et al.* relied on the calculation of upper limits of the alpha partial widths, assuming the lowest possible spin out of the ranges known at the time. This resulted in partial width upper limits of the order $\Gamma_\alpha < 10^{-9}$ eV. However, spin/parity knowledge from the neutron capture studies of Massimi *et al.* [180] and the alpha transfer study of Ota *et al.* [174] have allowed stricter

constraints on the alpha partial widths of these states to be imposed, now of the order $\Gamma_\alpha < 10^{-11}$ eV. These smaller widths have resulted in much weaker (α, n) resonance strengths for these resonances. As can be seen in Figure 5.16, this results in a negligible reaction rate contribution from these resonances, leading to a reduction in the rate of the ^{22}Ne$(\alpha, n)^{25}$Mg reaction above 0.2 GK relative to that recommended by Longland *et al.* Once again, the lower reaction rate calculated from the work of Jayatissa *et al.* [116] at higher temperatures can be explained by the alpha partial width for the state at 11.3195 MeV extracted being lower than that from direct reactions.

During the latter phases of the preparation of this thesis, Adsley *et al.* (2021) [188] published a review of the current state of studies intending to constrain the rates of the ^{22}Ne $+ \alpha$ reactions. In this study, a Monte Carlo calculation of the reaction rates and upper and lower limits were performed. However, some differences in the methods of parameter choice for the states of astrophysical importance, specifically the alpha partial widths, are of note. For the resonances associated with the state at 11.084 and 11.171 MeV, alpha partial widths are taken from the alpha transfer studies of Refs. [116] and [174]. However, for states at 10.949, 11.112, 11.163 and 11.169 MeV, calculations of Wigner limits are used, despite all these states being observed or having experimental upper limits placed on their alpha widths in the same alpha-transfer studies. This exclusion of the alpha widths from the 10.949 and 11.112 MeV states results in Adsley *et al.* [188] calculating an ^{22}Ne$(\alpha, \gamma)^{26}$Mg rate less than that of the current study below 0.2 GK, and an ^{22}Ne$(\alpha, n)^{25}$Mg rate that could be higher than that calculated in the current study at temperatures below 0.2 GK.

Chapter 6

Summary and Discussion

The two experiments discussed in this work achieved their original goals by successfully constraining astrophysically important nuclear reaction rates. The first experiment constrained the $^{25}\text{Al}(p,\gamma)^{26}\text{Si}$ reaction rate at nova temperatures (with the results published in a peer-reviewed paper [1]) and the second experiment constrained the $^{22}\text{Ne}(\alpha,n)$ and $^{22}\text{Ne}(\alpha,\gamma)$ reaction rates for neutron production in the weak s-process.

In the first experiment described in this thesis, the $^{25}\text{Mg}(d,p)$ reaction was measured using the Enge split-pole spectrograph at TUNL to study the states in ^{26}Mg that are mirror states of the resonances in the $^{25}\text{Al}(p,\gamma)^{26}\text{Si}$ reaction in nova burning conditions, a key reaction for determining the yield of ^{26}Al in novae. Only the 3^+ resonance has been experimentally constrained in ^{26}Si previously, and previous transfer studies of the mirror nucleus ^{26}Mg have failed to cleanly resolve the mirror 0^+ and 1^+ states [139, 140], or have produced anomalously large spectroscopic factors for the 1^+ state [143]. This work allowed the first clean and reliable extraction of an absolute value and upper limit for the spectroscopic factors of the 0^+ and 1^+ states in ^{26}Mg respectively (along with a measurement of the spectroscopic factor of the 3^+ state).

By comparing these spectroscopic factors to shell-model calculations, proton partial widths for the mirror states in ^{26}Si were estimated. The extracted partial width for the 3^+ state of $\sim$2.6 eV agrees with a $^{25}\text{Al}(d,n)^{26}\text{Si*}(p)$ study that measured the width directly in ^{26}Si [157], while the 0^+ partial width is consistent with the small value predicted by shell-model calculations [86]. The strict upper limit that has been placed on the proton partial width of the 1^+ state is in agreement with shell-model calculations, but is roughly 40 times smaller than

the partial width implied by a previous (^{4}He, ^{3}He) study, suggesting that there were multi-step contributions in the yield of the 1^+ state in that study [143] and what was extracted was not a pure spectroscopic factor.

Reaction rate calculations using these three resonances have re-affirmed the 3^+ state to dominate at higher temperatures, while the first reliable experimental constraints this work has placed on the 0^+ state show that it contributes up to $\sim$10% of the reaction rate across all temperatures. The limit on the 1^+ proton partial width confirms that, while it dominates the rate at lower temperatures, it never competes significantly with the β-decay of ^{25}Al, re-affirming that the resonance has very little effect on the amount of ^{26}Al produced in novae.

The 0^+ and 1^+ states both have proton partial widths smaller than their γ partial widths, meaning the constraints from this work have significantly reduced the uncertainty in their resonance strengths. As the most significant resonance for the ^{25}Al$(p,\gamma)^{26}$Si reaction, future efforts to constrain the rate should focus on more accurate values of the partial widths of the 3^+ state. As the method for extracting Γ_γ for the state relies on knowledge of Γ_p, a reduction in the uncertainty of Γ_p improves knowledge of both parameters. A recent re-measurement of the ^{25}Al$(d,n)^{26}$Si*(p) reaction at FSU, presented in Ref. [189], with a much clearer spectrum than in the previous (d,n) work, suggests that more accurate information on this state could be available in the near future.

A negative parity state in ^{26}Si around 5.5–6.2 MeV could contribute to the ^{25}Al$(p,\gamma)^{26}$Si reaction rate at nova temperatures through an ℓ=1 resonance. Previous indirect evidence from γ-decay [142] and (d,p) studies [139, 140] indicate the existence of a 1^- state around 5.7 MeV in ^{26}Mg. In the current work, all individual states could not be resolved, but the angular distribution of the peak measured at 5.7 MeV is not in conflict with the existence of a negative parity state at this energy. The identification of a mirror state to this in ^{26}Si and the measurement of its properties would greatly clarify its role in the ^{25}Al(p,γ) reaction rate.

As described in the second experiment of this thesis, the Enge split-pole spectrometer measured the population of excited states of ^{26}Mg above the alpha threshold (S_α=10.615 MeV) using the ^{25}Mg(d,p) reaction, to constrain properties of those states relevant to the ^{22}Ne(α,n) and ^{22}Ne(α,γ) reactions. These two reactions proceed through resonances of natural parity states in ^{26}Mg above the alpha threshold and their rates determine the neutron budget in the weak s-process. Direct measurements of resonances that control these rates have only

been possible for excitation energies at 11.3195 MeV and above, with indirect studies constraining the lower resonances. Recent alpha transfer studies [116, 174] have constrained these resonance strengths by extracting alpha partial widths for the corresponding states. However, these values are strongly dependent on knowledge of the spin/parities of these states. In the current work, the angular distributions of states above the alpha threshold were compared to weakly-bound DWBA calculations for different ℓ-transfers, with the best-fitting transfers constraining the spin/parities of these states. The astrophysically significant states at 10.826, 10.9491, 11.084 and 11.11223 MeV were re-affirmed to have spin/parities 2^+, 1^-, 2^+ and 2^+ respectively. These assignments were combined with the results of alpha-transfer experiments to constrain alpha partial widths of the resonances, which determine the resonance strengths in the ^{22}Ne $+ \alpha$ reactions.

Using these constrained width values, reaction rate calculations indicated the states in ^{26}Mg at 10.9491, 11.084 and 11.3195 MeV dominate the ^{22}Ne$(\alpha,\gamma)^{26}$Mg rate across temperatures relevant for neutron production in the weak s-process, while excited states at 11.112 and 11.3195 MeV control the ^{22}Ne$(\alpha,n)^{25}$Mg reaction rate.

As mentioned, the strength of the resonance associated with the state at 11.3195 MeV has been directly measured, constraining both reaction rates above $\sim$0.2 GK. However, the resonances associated with the states at 10.949 and 11.112 MeV dominate the ^{22}Ne$(\alpha,\gamma)^{26}$Mg and ^{22}Ne$(\alpha,n)^{25}$Mg reaction rates respectively below $\sim$0.2 GK. As neither of these resonance strengths have been measured directly, and the temperature range they cover is likely where the (α,n) rate will overtake the (α,γ) rate, constraining these strengths further is vital to determining the weak s-process neutron budget. Only an upper limit has been placed on the alpha partial width of the 11.112 MeV state. As its spin/parity is now certain, a high-sensitivity alpha transfer study could be able to measure an absolute value for its alpha partial width. Direct measurements of both resonances would significantly constrain the reaction rates. The direct measurement of the resonance strength of the 10.949 MeV state in the (α,γ) reaction is planned at the Laboratory for Underground Nuclear Astrophysics (LUNA), with a previous campaign placing an upper limit on the resonance strength consistent with previous indirect measurements [190]. Measurements of the properties of these two states will significantly further constrain the rates of the ^{22}Ne $+ \alpha$ reactions. This will provide greater certainty on the neutron budget available for the weak s-process, giving a clear understanding of the

nucleosynthesis of elements between A=60 and A=90 through this process.

Appendix A

Composition of Experimental Target

CERTIFICATE OF ANALYSIS
#7-00-M

Name of Preparation: ^{25}Mg

Country of Destination: United States

Consignee: Argonne National Laboratory

CHARACTERISTICS OF ISOTOPE-ENRICHED PRODUCT

1. **Weight of enriched isotope:**

   Compound weight: 200.0mg   **Element weight:** 200.0mg

   Form: Mg (Metal)

2. **Isotopic composition:**

Isotope	24	25	26				
Enrichment (%)	0.47	99.2 ± 0.1	0.33				

3. **Chemical Impurities:**

Element	Symbol	Impurity Measurement (ppm)	Element	Symbol	Impurity Measurement (ppm)
Silver	Ag	<1	Gallium	Ga	<1
Aluminium	Al	10	Gadolinium	Gd	<1
Arsenic	As	<1	Germanium	Ge	<1
Gold	Au	<1	Hafnium	Hf	<1
Boron	B	10	Mercury	Hg	<1
Barium	Ba	<1	Holmium	Ho	<1
Beryllium	Be	<1	Iodine	I	<5
Bismuth	Bi	<1	Indium	In	<1
Bromine	Br	<50	Iridium	Ir	<1
Calcium	Ca	<100	Potassium	K	<50
Cadmium	Cd	<1	Lanthanum	La	<1
Cerium	Ce	<1	Lithium	Li	<1
Cobalt	Co	<1	Lutetium	Lu	<1
Chromium	Cr	<5	Manganese	Mn	4
Cesium	Cs	1	Molybdenum	Mo	<1
Copper	Cu	3	Sodium	Na	47
Dysprosium	Dy	<1	Niobium	Nb	<1
Erbium	Er	<1	Neodymium	Nd	<1
Europium	Eu	<1	Nickel	Ni	<1
Iron	Fe	800	Osmium	Os	<1

Figure A.1 *Target composition certification for the material used to make the targets in the current experiments, performed by Trace Sciences International and cosigned by Argonne National Laboratory.*

118

Appendix B

Kinematics Calculations

B.1 Conversion of angles and differential cross sections from laboratory to centre-of-mass frame

As the outputs of DWBA calculations are in the centre-of-mass frame, the angles and cross sections must be converted to the same frame to be compared.

For a reaction $A(a,b)B$, the ratio between the velocity of the centre-of-mass frame v_c and the velocity of the ejected particle in the CoM frame $v_b{}'$ is calculated as follows [85]:

$$\gamma \equiv \frac{v_c}{v_b'} = \sqrt{\frac{m_a m_b E_{beam}}{m_B(m_b + m_B)Q + m_B(m_B + m_b - m_a)E_{beam}}}, \qquad \text{(B.1)}$$

where

$E_{beam} \equiv$ beam energy

$Q \equiv Q$ value of the reaction

$m_a \equiv$ mass of incoming particle

$m_b \equiv$ mass of ejected particle

$m_A \equiv$ mass of target

$m_b \equiv$ mass of residual nucleus.

The centre-of-mass (θ') and lab angles (θ) for a reaction have the following relationship, which was solved for θ' to calculate centre-of-mass angles:

$$\tan(\theta) = \frac{\sqrt{1 - \left(\frac{v_c^2}{c^2}\right)} \sin(\theta')}{\cos(\theta') + \gamma}. \tag{B.2}$$

Differential cross sections for a nuclear reaction of A(a, b)B were converted from the lab frame to the centre-of-mass frame as follows [85]:

$$\left(\frac{d\sigma}{d\Omega}\right)'_{\theta'} = \frac{1 + \gamma \cos(\theta')}{1 + \gamma^2 + 2\gamma \cos(\theta')^{3/2}} \left(\frac{d\sigma}{d\Omega}\right)_{\theta}. \tag{B.3}$$

B.2 Conversion of residual nucleus excitation energy to ejected particle magnetic rigidity

For a known excitation energy, the magnetic rigidity of the ejected particle can be calculated using the procedure described below.

Subscripts $beam$, T, p, rec and CoM refer to the incident beam, target nucleus, outgoing proton, recoil nucleus and centre-of-mass frame respectively. Subscripts i and f refer to properties before and after the reaction. Lab frame variables are unprimed, while centre-of-mass (CoM) variables are primed.

The energy in the centre-of-mass frame of the beam is given by:

$$T'_{beam} = T_{beam} \left(\frac{m_T}{m_T + m_{beam}} \right). \tag{B.4}$$

Thus, the total kinetic energy in the centre-of-mass frame after the reaction, T_{total} is given by:

$$T'_{total} = Q + T'_{beam} - E_{x,rec}. \tag{B.5}$$

This means the ejected particle has centre-of-mass energy, Lorentz factor and velocity are given by:

$$T'_p = \frac{T'_{total}}{1 + \frac{m_p}{m_{rec}}},$$

$$\gamma'_p = \frac{T'_p}{m_p + 1},$$

$$v'_p[c] = \sqrt{1 - \frac{1}{\gamma'^2_p}}. \tag{B.6}$$

To calculate the centre-of-mass frame velocity, the velocity of the beam must first be calculated:

$$\gamma_{beam} = 1 + \frac{T_{beam}}{m_{beam}},$$

$$v_{beam} = \sqrt{1 - \frac{1}{\gamma^2_{beam}}}. \tag{B.7}$$

Thus, the velocity of the centre-of-mass frame (relative to the lab frame) before

and after the reaction is given by:

$$v_i = \frac{m_{beam}}{m_{beam} + m_{targ}} v_{beam},$$

$$v_f = \frac{m_{beam} + m_{targ}}{m_p + m_{rec}} v_i. \tag{B.8}$$

This allows the CoM angle of the ejected particle to be calculated, which can be combined with the results of equation B.6 to give the two components of its CoM velocity:

$$\tan(\theta) = \frac{\sqrt{1 - \left(\frac{v^2}{c^2}\right)} \sin(\theta')}{\cos(\theta') + \frac{v_f}{v_p'}},$$

$$v_{px}' = v_p' \cos\theta',$$

$$v_{py}' = v_p' \sin\theta'. \tag{B.9}$$

Using Lorentzian transformations, these velocities can be converted in to the lab frame, giving properties of the ejectile in the lab frame:

$$v_{px} = \frac{v_{px}' + v_f}{1 + v_{px}' v_f},$$

$$v_{py} = \frac{\sqrt{1 - \frac{v^2}{c^2}} v_{py}'}{1 + \frac{v}{c^2} v_{px}'},$$

$$v_p = \sqrt{v_{px}^2 + v_{py}^2},$$

$$\gamma_p = \frac{1}{\sqrt{1 - \frac{v_p^2}{c^2}}},$$

$$p_p[\text{MeV/c}] = m_p[\text{MeV}]\sqrt{\gamma_p^2 - 1}. \tag{B.10}$$

Conversion of the momentum to a magnetic rigidity is then possible:

$$\frac{p}{q}[kgms^{-1}C^{-1}] = B\rho[Tm],$$

$$\frac{p}{q}[MeV/c/e] = \frac{5.344 \times 10^{-16}}{1.609 \times 10^{-19}} \frac{p}{q}[kgms^{-1}C^{-1}],$$

$$\frac{p}{q}[MeV/c/e] = 299.7925 B\rho[Tm]. \tag{B.11}$$

B.3 Calculation of mean and statistical uncertainties of excitation energies

The weighted mean excitation energy $\overline{E_x}$ of a peak across several runs and its associated statistical uncertainty $\sigma_{\bar{E}_x}$ can be calculated using the following method:

$$\overline{E_x} = \frac{1}{\sum_i^n \frac{1}{\Delta E_{xi}^2}} \sum_i^n \frac{E_{xi}}{\Delta E_{xi}^2},$$

$$\sigma_{\bar{E}_x}^2 = \frac{1}{\sum_i^n \frac{1}{\Delta E_{xi}^2}} \frac{1}{n-1} \sum_i^n \frac{(E_{xi} - \overline{E_x})^2}{\Delta E_{xi}^2}. \tag{B.12}$$

where

$E_{xi} \equiv$ excitation energy from single run

$\overline{E_x} \equiv$ mean excitation energy

$\sigma_{\bar{E}_x}^2 \equiv$ standard deviation of mean excitation energy

$n \equiv$ number of runs peak observed at

$i \equiv$ index for run peak observed at.

Appendix C

Alpha partial widths from alpha transfer experiments

Direct measurements of the resonances of the ^{22}Ne$(\alpha, \gamma)^{26}$Mg and ^{22}Ne$(\alpha, n)^{25}$Mg reactions are very challenging, especially for the lower energy resonances, due to their low cross sections. Just above the alpha threshold, the alpha partial width is much smaller than the other partial widths (due to the Coulomb barrier the alpha particle experiences), meaning the resonance strength is largely dependent on the alpha partial width. Alpha transfer experiments will only populate the natural parity (0^+, 1^-, 2^+...) states of ^{26}Mg, i.e., the states the ^{22}Ne$(\alpha, \gamma)^{26}$Mg and ^{22}Ne$(\alpha, n)^{25}$Mg reactions proceed through, and the yield from each of these states allows an estimation of the alpha partial width of that state. In contrast to the (d, p) reactions described in this thesis, the spin/parity of a state in the ^{22}Ne alpha transfer experiments only has one ℓ-transfer that can populate that state.

In the sub-Coulomb transfer work of Jayatissa *et al.* [116], the cross sections of natural parity states populated by alpha transfer were calculated and analysed using distorted wave Born approximation (DWBA) weakly bound state approximation calculations. By comparing experimentally measured cross sections to theoretical cross sections, a spectroscopic factor was extracted for each state, allowing the calculation of asymptotic normalisation coefficients (ANCs), C^2, for each state. ANC values were then used to calculate the reduced widths

(γ^2) using the following relationship:

$$C^2 = \frac{2\mu R}{\hbar^2 W^2_{-\eta,\ell+1/2}(2kR)} \frac{\gamma^2}{1 + \gamma^2 \frac{dS}{dE}},$$ (C.1)

where

$\mu \equiv$ reduced mass of the system,

$R \equiv$ channel radius,

$W \equiv$ Whittaker function,

$S \equiv S_\ell(kR) \equiv$ shift function.

The alpha partial widths were then calculated using the reduced widths:

$$\Gamma_\alpha = \frac{2\gamma^2 P}{1 + \gamma^2 \frac{dS}{dE}},$$ (C.2)

where

$P \equiv P_\ell(kR) \equiv$ penetrability function.

More information on using ANCs to extract partial widths can be found in Refs. [191] and [192].

In Jayatissa *et al.* [116], the alpha partial widths were calculated at several artificial binding energies, using the DWBA weakly bound approximation. These calculated widths were then linearly extrapolated to the true (negative) binding energy of the state to arrive at final values for the partial widths. This method was also performed successfully in Ref. [117].

As the choice of spin/parities impact the theoretical calculations of alpha transfer experiments, the alpha partial widths extracted are dependent on knowledge of the spin/parities for the states observed in alpha transfer experiments.

Bibliography

[1] C. B. Hamill *et al.*, Eur. Phys. J. A **56**, 36 (2020).

[2] E. Rutherford, London, Edinburgh, Dublin Philos. Mag. J. Sci. **12**, 134 (1906).

[3] H. Geiger and E. Marsden, Proc. R. Soc. Lond. A **82**, 495 (1909).

[4] E. Rutherford, London, Edinburgh, Dublin Philos. Mag. J. Sci. **21**, 669 (1911).

[5] William Thomson, Macmillan's Mag. 388 (1862).

[6] A. Eddington, Nature **106**, 14 (1920).

[7] G. Squires, J. Chem. Soc. 3893 (1998).

[8] H. A. Bethe, Phys. Rev. **55**, 434 (1939).

[9] C. von Weizsacker, Phys. Zeitschrift **38**, 176 (1937).

[10] M. Asplund, N. Grevesse, A. J. Sauval, and P. Scott, Annu. Rev. Astron. Astrophys. **47**, 481 (2009).

[11] F. Hoyle, Astrophys. J. Suppl. **1**, 121 (1954).

[12] M. Asplund, N. Grevesse, and A. Jacques Sauval, Nucl. Phys. A **777**, 1 (2006).

[13] M. E. Burbidge, G. R. Burbidge, W. A. Fowler, and F. Hoyle, Rev. Mod. Phys. **29**, 548 (1957).

[14] A. G. W. Cameron, *Stellar evolution, nuclear astrophysics, and nucleogenesis*, 2nd ed. (Atomic Energy of Canada Ltd., Chalk River, Ontario, 1957).

[15] A. G. W. Cameron, Publ. Astron. Soc. Pacific **69**, 201 (1957).

[16] A. G. W. Cameron, in *Stellar evolution, nuclear astrophysics, and nucleogenesis*, 2nd ed., edited by D. M. Kahl (Dover Publications, Inc., Mineola, New York, 2013).

[17] H. Schatz, J. Phys. G Nucl. Part. Phys. **43**, 064001 (2016).

[18] G. Fontaine, P. Brassard, and P. Bergeron, Publ. Astron. Soc. Pacific **113**, 409 (2001).

[19] S. O. Kepler *et al.*, Mon. Not. R. Astron. Soc. **375**, 1315 (2007).

[20] H. L. Shipman, Astrophys. J. **228**, 240 (1979).

[21] J. Jose, *Stellar Explosions: Hydrodynamics and Nucleosynthesis*, 1st ed. (CRC Press/Taylor and Francis, Boca Raton, 2016).

[22] S. Starrfield, C. Iliadis, and W. R. Hix, in *Class. Novae*, 2nd ed., edited by M. F. Bode and A. Evans (Cambridge University Press, Cambridge, 2008), Chap. 4, pp. 77–101.

[23] J. Jose and S. N. Shore, in *Class. Novae*, 2nd ed., edited by M. F. Bode and A. Evans (Cambridge University Press, Cambridge, 2008), Chap. 6, pp. 121–140.

[24] S. Starrfield, C. Iliadis, and W. R. Hix, The thermonuclear runaway and the classical nova outburst, 2016.

[25] A. W. Shafter, Astrophys. J. **834**, 196 (2017).

[26] S. Starrfield *et al.*, AIP Conf. Proc. **891**, 364 (2007).

[27] C. Iliadis *et al.*, Astrophys. J. **855**, 76 (2018).

[28] C. Iliadis *et al.*, Astrophys. J. Suppl. Ser. **142**, 105 (2002).

[29] J. José *et al.*, Astrophys. J. **612**, 414 (2004).

[30] J. José and M. Hernanz, J. Phys. G Nucl. Part. Phys. **34**, R431 (2007).

[31] K. Setoodehnia *et al.*, Phys. Rev. C **98**, 055804 (2018).

[32] K. Setoodehnia *et al.*, Phys. Rev. C **99**, 055812 (2019).

[33] T. Lee, D. A. Papanastassiou, and G. J. Wasserburg, Geophys. Res. Lett. **3**, 41 (1976).

[34] P. A. Denissenkov *et al.*, Mon. Not. R. Astron. Soc. **442**, 2058 (2014).

[35] A. Kankainen *et al.*, Phys. Lett. Sect. B Nucl. Elem. Part. High-Energy Phys. **813**, 136033 (2021).

[36] M. Auer *et al.*, Earth Planet. Sci. Lett. **287**, 453 (2009).

[37] S. E. Woosley and T. A. Weaver, Astrophys. J. **238**, 1017 (1980).

[38] Pulu, Al-26 Decay Scheme, 2019.

[39] P. Merrill, Astrophys. J. **116**, 21 (1952).

[40] A. Bellerive, Int. J. Mod. Phys. A **19**, 1167 (2004).

[41] W. Mahoney, J. Ling, W. A. Wheaton, and J. A.S., Astrophys. J. **286**, 578 (1984).

[42] J. R. Simanton, R. A. Rightmire, A. L. Long, and T. P. Kohman, Phys. Rev. **96**, 1711 (1954).

[43] D. M. Smith, New Astron. Rev. **48**, 87 (2004).

[44] R. Diehl *et al.*, Nature **439**, 45 (2006).

[45] W. Wang *et al.*, Astron. Astrophys. **496**, 713 (2009).

[46] P. Martin, J. Knödlseder, R. Diehl, and G. Meynet, Astron. Astrophys. **506**, 703 (2009).

[47] L. Bouchet, E. Jourdain, and J. P. Roques, Astrophys. J. **801**, 142 (2015).

[48] K. Kretschmer *et al.*, Astron. Astrophys. Rev. **559**, 1 (2013).

[49] M. Lugaro, U. Ott, Kereszturi, and Á. Kereszturi, Prog. Part. Nucl. Phys. **102**, 1 (2018).

[50] B. Côté *et al.*, Astrophys. J. **878**, 156 (2019).

[51] C. Baldovin, M. Pignatari, and R. Gallino, Mem. della Soc. Astron. Ital. **77**, 927 (2006).

[52] M. Limongi and A. Chieffi, Astrophys. J. **647**, 483 (2006).

[53] N. Prantzos, Astron. Astrophys. **420**, 1033 (2004).

[54] G. J. Wasserburg, A. I. Karakas, and M. Lugaro, Astrophys. J. **836**, 126 (2017).

[55] S. W. Jones *et al.*, Mon. Not. R. Astron. Soc. **485**, 4287 (2019).

[56] C. Tur, A. Heger, and S. M. Austin, Astrophys. J. **718**, 357 (2010).

[57] J. José and C. Iliadis, Rep. Prog. Phys **74**, 96901 (2011).

[58] E. Vangionia-Flam, J. Audouze, and J.-P. Chieze, Astron. Astrophys. **82**, 234 (1980).

[59] M. Arnould, H. Norgaard, F.-K. Thielemann, and W. Hillebrandt, Astrophys. J. **237**, 931 (1980).

[60] S. Starrfield *et al.*, Phys. Rep. **227**, 223 (1993).

[61] A. Parikh and J. José, Phys. Rev. C **88**, 048801 (2013).

[62] F. Strieder *et al.*, Phys. Lett. Sect. B Nucl. Elem. Part. High-Energy Phys. **707**, 60 (2012).

[63] W. J. Huang *et al.*, Chinese Phys. C **41**, 030002 (2017).

[64] M. L. Pumo, in *Astrophysics*, edited by Ibrahim Kucuk (IntechOpen, London, 2012), Chap. 3.

[65] J. J. Cowan *et al.*, Rev. Mod. Phys. **93**, 15002 (2021).

[66] H. C. Urey and B. Donn, Astrophys. J. **124**, 307 (1956).

[67] D. D. Clayton and W. A. Fowler, Ann. Phys. (N. Y). **16**, 51 (1961).

[68] P. A. Seeger and W. A. Fowler, Astrophys. J. Suppl. **11**, 121 (1964).

[69] D. Watson *et al.*, Nature **574**, 497 (2019).

[70] J. C. Lattanzio and P. R. Wood, *Asymptot. Giant Branch Stars* (Springer, New York, 2004), Chap. 2, pp. 23–104.

[71] R. Reifarth, C. Lederer, and F. Käppeler, J. Phys. G Nucl. Part. Phys. **41**, 053101 (2014).

[72] U. Battino *et al.*, Universe **7**, 25 (2021).

[73] S. Cristallo *et al.*, Astrophys. J. **859**, 105 (2018).

[74] D. D. Clayton and M. E. Rassbach, Astrophys. J. **148**, 69 (1967).

[75] C. Travaglio, R. Gallino, M. Busso, and R. Gratton, Astrophys. J. **549**, 346 (2001).

[76] R. Gallino *et al.*, Astrophys. J. **497**, 388 (1998).

[77] F. Käppeler, R. Gallino, S. Bisterzo, and W. Aoki, Rev. Mod. Phys. **83**, 157 (2011).

[78] M. Pignatari *et al.*, Astrophys. J. **710**, 1557 (2010).

[79] A. C. Philips, *The Physics of Stars*, 2nd ed. (Wiley, New York, 1999).

[80] D. Bemmerer *et al.*, Nucl. Phys. A **779**, 297 (2006).

[81] M. S. Basunia *et al.*, Nucl. Data Sheets **134**, 1 (2016).

[82] C. M. Raiteri, M. Busso, R. Gallino, and G. Picchio, Astrophys. J. **371**, 665 (1991).

[83] B. Bucher *et al.*, Phys. Rev. Lett. **114**, 251102 (2015).

[84] M. Wang *et al.*, Chinese Phys. C **36**, 1603 (2012).

[85] C. Iliadis, *Nuclear Physics of Stars*, 1st ed. (Wiley, Weinheim, 2007).

[86] W. A. Richter, B. A. Brown, A. Signoracci, and M. Wiescher, Phys. Rev. C **83**, 065803 (2011).

[87] A. Matic *et al.*, Phys. Rev. C **82**, 025807 (2010).

[88] J. P. Schiffer, Nucl. Phys. **46**, 246 (1963).

[89] C. Iliadis, Nucl. Phys. A **618**, 166 (1997).

[90] N. K. Timofeyuk and R. C. Johnson, Prog. Part. Nucl. Phys. **111**, 103738 (2020).

[91] N. K. Timofeyuk, R. C. Johnson, and A. M. Mukhamedzhanov, Phys. Rev. Lett. **91**, 23 (2003).

[92] N. K. Timofeyuk and P. Descouvemont, Phys. Rev. C **72**, 064324 (2005).

[93] D. E. Hoff *et al.*, Nature **580**, 52 (2020).

[94] J. A. Nolen and J. P. Schiffer, Phys. Lett. **29B**, 396 (1969).

[95] P. E. Hodgson, in *Nuclear Reactions and Nuclear Structure*, edited by W. Marshall and D. Wilkinson (Oxford University Press, London, 1971), p. 302.

[96] M. Callens, Ph.D. thesis, K.U. Leuven, 2013.

[97] A. Gallman *et al.*, Nucl. Phys. **88**, 654 (1966).

[98] F. Meurders and G. De Korte, Nucl. Phys. A **249**, 205 (1975).

[99] T. A. Schmick, K. W. Kemper, P. K. Bindal, and R. D. Koshel, Phys. Rev. C **10**, 556 (1974).

[100] F. Hammache, N. Oulebsir, P. Roussel, and M. G. Pellegriti, J. Phys. Conf. Ser. **665**, 012007 (2016).

[101] N. Oulebsir *et al.*, Phys. Rev. C **85**, 035804 (2012).

[102] N. B. Nguyen, F. M. Nunes, and R. C. Johnson, Phys. Rev. C **82**, 014611 (2010).

[103] I. Thompson, Comput. Phys. Reports **7**, 167 (1988).

[104] I. J. Thompson and F. M. Nunes, *Nuclear Reactions for Astrophysics: Principles, Calculation and Applications of Low-Energy Reactions*, 1st ed. (Cambridge University Press, Cambridge, 2009), p. 480.

[105] H. An and C. Cai, Phys. Rev. C **73**, 054605 (2006).

[106] X. Li and C. Cai, Nucl. Phys. A **801**, 43 (2008).

[107] N. Austern *et al.*, Phys. Rep. **154**, 125 (1987).

[108] M. Avrigeanu and V. Avrigeanu, J. Phys. Conf. Ser. **205**, 012014 (2010).

[109] M. Kamimura *et al.*, Prog. Theor. Phys. Suppl. **89**, 136 (1986).

[110] Y. Han, Y. Shi, and Q. Shen, Phys. Rev. C **74**, 044615 (2006).

[111] A. J. Koning and J. P. Delaroche, Nucl. Phys. A **713**, 231 (2003).

[112] E. S. Soukhovitski, S. Chiba, and J. Y. Lee, AIP Conf. Proc. **769**, 1100 (2005).

[113] J. Bang and J. Zimanyi, Nucl. Phys. A **139**, 534 (1969).

[114] C. M. Vincent and H. . T. Fortune, Phys. Rev. C **2**, 1 (1970).

[115] V. E. Bunakov, Nucl. Phys. A **140**, 241 (1970).

[116] H. Jayatissa *et al.*, Phys. Lett. Sect. B Nucl. Elem. Part. High-Energy Phys. **802**, 135267 (2020).

[117] M. L. Avila *et al.*, Phys. Rev. C **90**, 042801 (2014).

[118] D. Kahl *et al.*, Phys. Lett. Sect. B Nucl. Elem. Part. High-Energy Phys. **797**, 134803 (2019).

[119] W. Hasuer and H. Feshbach, Phys. Rev. **87**, 366 (1952).

[120] P. E. Hodgson, Reports Prog. Phys. **50**, 1171 (1987).

[121] T. Rauscher, F. K. Thielemann, and K. L. Kratz, Phys. Rev. C **56**, 1613 (1997).

[122] M. Wang *et al.*, Chinese Phys. C **41**, 10 (2017).

[123] S. Karampagia, R. A. Senkov, and V. Zelevinsky, At. Data Nucl. Data Tables **120**, 1 (2018).

[124] B. V. Carlson, J. E. Escher, and M. S. Hussein, J. Phys. G Nucl. Part. Phys. **41**, 094003 (2014).

[125] A. J. Koning, S. Hilaire, and M. C. Duijvestijn, Int. Conf. Nucl. Data Sci. Technol. 211 (2008).

[126] S. Hilaire, C. Lagrange, and A. J. Koning, Ann. Phys. **306**, 209 (2003).

[127] N. S. University, NC State University Experimental Nuclear Physics, 2021.

[128] C. R. Westerfeldt *et al.*, Nucl. Instruments Methods Phys. Res. **219**, 284 (1984).

[129] J. F. Wilkerson, T. B. Clegg, and E. J. Ludwig, Nucl. Instruments Methods Phys. Res. **207**, 331 (1983).

[130] H. A. Enge, Phys. Today **20**, 65 (1967).

[131] N. Instruments and H. A. Enge, **162**, 161 (1979).

[132] C. Marshall *et al.*, IEEE Trans. Instrum. Meas. **68**, 533 (2019).

[133] G. F. Knoll, *Radiation Detection and Measurement*, 3rd ed. (John Wiley and Sons, New York, 2000).

[134] Dougsim, Proportional counter avalanches, 2012.

[135] Saint-Gobain, Saint-Gobain Crystals BC-400, BC-404 Plastic SCintillators, 2021.

[136] H. Photonics, Technical report, Hamamatsu Photonics K.K., Tokyo (unpublished).

[137] K. B. Swartz, D. W. Visser, and J. M. Baris, Nucl. Instruments Methods Phys. Res. Sect. A Accel. Spectrometers, Detect. Assoc. Equip. **463**, 354 (2001).

[138] G. C. Smith, J. Fischer, and V. Radeka, IEEE Trans. Nucl. Sci. **35**, 409 (1988).

[139] M. Burlein, K. S. Dhuga, and H. T. Fortune, Phys. Rev. C **29**, 2013 (1984).

[140] H. F. Arciszewski *et al.*, Nucl. Physics, Sect. A **A430**, 234 (1984).

[141] F. Wang *et al.*, Phys. Lett. Sect. B Nucl. Elem. Part. High-Energy Phys. **770**, 83 (2017).

[142] S. S. Bhattacharjee *et al.*, Phys. Rev. C **89**, 024324 (2014).

[143] M. Yasue *et al.*, Phys. Rev. C **42**, 1279 (1990).

[144] C. Iliadis *et al.*, Phys. Rev. C **53**, 475 (1996).

[145] A. Nagel *et al.*, J. Phys. G Nucl. Phys. **1**, 324 (1975).

[146] F. Glatz *et al.*, At. Nucl. **324**, 187 (1986).

[147] E. W. Lees *et al.*, J. Phys. A Math. Nucl. Gen. **7**, 936 (1974).

[148] G. F. Grinyer *et al.*, Phys. Rev. C **71**, 044309 (2005).

[149] D. Seweryniak *et al.*, Phys. Rev. C **75**, 062801 (2007).

[150] N. De Séréville *et al.*, Proc. Sci. **NIC XI**, 212 (2010).

[151] T. Komatsubara *et al.*, Eur. Phys. J. A **50**, 136 (2014).

[152] D. T. Doherty *et al.*, Phys. Rev. C **92**, 035808 (2015).

[153] D. W. Bardayan *et al.*, Phys. Rev. C **74**, 045804 (2006).

[154] K. A. Chipps *et al.*, Phys. Rev. C **82**, 045803 (2010).

[155] J. C. Thomas *et al.*, Eur. Phys. J. A **21**, 419 (2004).

[156] M. B. Bennett *et al.*, Phys. Rev. Lett. **111**, 232503 (2013).

[157] P. N. Peplowski *et al.*, Phys. Rev. C **79**, 032801 (2009).

[158] P. F. Liang *et al.*, Phys. Rev. C **101**, 024305 (2020).

[159] Y. Parpottas *et al.*, Phys. Rev. C **70**, 065805 (2004).

[160] F. Ajzenberg-Selove and K. L. Dunning, Phys. Rev. **119**, 1681 (1960).

[161] W. R. McMurray, P. Van Der Merwe, and I. J. Van Heerden, Nucl. Physics, Sect. A **92**, 401 (1967).

[162] D. C. De Martini and T. R. Donoghue, Phys. Rev. C **8**, 621 (1973).

[163] J. A. Caggiano *et al.*, Phys. Rev. C - Nucl. Phys. **65**, 055801 (2002).

[164] N. K. Timofeyuk, P. Descouvemont, and R. C. Johnson, Eur. Phys. J. A **27**, 269 (2006).

[165] J. J. Parker, Ph.D. thesis, Florida State University, 2017.

[166] H. Yamaguchi, Pentrability/Wigner Limit Calculator.

[167] C. E. Rolfs and W. S. Rodney, *Cauldrons in the Cosmos* (The University of Chicago Press, Chicago and London, 1988).

[168] J. Long *et al.*, Phys. Rev. C **96**, 015502 (2017).

[169] C. Iliadis *et al.*, Nucl. Phys. A **841**, 31 (2010).

[170] S. Hunt *et al.*, Phys. Rev. C **99**, 045804 (2019).

[171] U. Giesen *et al.*, Nucl. Physics, Sect. A **561**, 95 (1993).

[172] C. Ugalde *et al.*, Phys. Rev. C **76**, 025802 (2007).

[173] R. Talwar *et al.*, Phys. Rev. C **93**, 055803 (2016).

[174] S. Ota *et al.*, Phys. Lett. Sect. B Nucl. Elem. Part. High-Energy Phys. **802**, 135256 (2020).

[175] P. Adsley *et al.*, Phys. Rev. C **97**, 045807 (2018).

[176] G. Lotay *et al.*, Eur. Phys. J. A **55**, 109 (2019).

[177] R. Longland *et al.*, Phys. Rev. C **80**, 055803 (2009).

[178] P. Adsley *et al.*, Phys. Rev. C **96**, 055802 (2017).

[179] C. Massimi *et al.*, Phys. Rev. C **85**, 044615 (2012).

[180] C. Massimi *et al.*, Phys. Lett. B **768**, 1 (2017).

[181] C. E. Moss, Nucl. Phys. **269**, 429 (1976).

[182] Y. Chen *et al.*, Phys. Rev. C **103**, 035809 (2021).

[183] T. A. Walkiewicz *et al.*, Phys. Rev. C **45**, 1597 (1992).

[184] G. M. Crawley *et al.*, Phys. Rev. C **39**, 311 (1989).

[185] K. Wolke *et al.*, Zeitschrift für Phys. A **334**, 491 (1989).

[186] M. Jaeger *et al.*, Phys. Rev. Lett. **87**, 202501 (2001).

[187] R. Longland, C. Iliadis, and A. I. Karakas, Phys. Rev. C **85**, 065809 (2012).

[188] P. Adsley *et al.*, Phys. Rev. C **103**, 015805 (2021).

[189] J. Baker, Ph.D. thesis, Florida State University, 2015.

[190] E. Masha and LUNA Collaboration, EPJ Web Conf. **227**, 1 (2020).

[191] A. M. Mukhamedzhanov and R. E. Tribble, Phys. Rev. C **59**, 3418 (1999).

[192] A. M. Mukhamedzhanov, Phys. Rev. C **86**, 044615 (2012).